

STATUS OF THESIS

Title of thesis

Application of Electromagnetic Waves and Zinc Oxide &
Aluminum Oxide as Dielectric Nanoparticles in
Enhanced Oil Recovery

I NOOR RASYADA BINTI AHMAD LATIFF

hereby allow my thesis to be placed at the Information Resource Center (IRC) of Universiti Teknologi PETRONAS (UTP) with the following conditions:

1. The thesis becomes the property of UTP
2. The IRC of UTP may make copies of the thesis for academic purposes only.
3. This thesis is classified as

Confidential

Non-confidential

If this thesis is confidential, please state the reason:

The contents of the thesis will remain confidential for _____ years.

Remarks on disclosure:

Endorsed by

Signature of Author

Signature of Supervisor

Permanent address: _____
25, Laluan Desa Pengkalan 13,
Taman Desa Pengkalan
31500 Lahat, Perak

Name of Supervisor
Dr. Hasnah Mohd Zaid

Date : _____

Date : _____

UNIVERSITI TEKNOLOGI PETRONAS

APPLICATION OF ELECTROMAGNETIC WAVES AND ZINC OXIDE &
ALUMINUM OXIDE AS DIELECTRIC NANOPARTICLES IN
ENHANCED OIL RECOVERY

by

NOOR RASYADA AHMAD LATIFF

The undersigned certify that they have read, and recommend to the Postgraduate Studies Programme for acceptance this thesis for the fulfillment of the requirements for the degree stated.

Signature: _____

Main Supervisor: Dr. Hasnah Mohd Zaid

Signature: _____

Co-Supervisor: Prof. Dr. Noorhana Yahya

Signature: _____

Head of Department: Dr. Rosdiazli Ibrahim

Date: _____

**APPLICATION OF ELECTROMAGNETIC WAVES AND ZINC OXIDE &
ALUMINUM OXIDE AS DIELECTRIC NANOPARTICLES IN
ENHANCED OIL RECOVERY**

by

NOOR RASYADA AHMAD LATIFF

A Thesis

Submitted to the Postgraduate Studies Program

as a Requirement for the Degree of

**MASTER OF SCIENCE
ELECTRICAL AND ELECTRONICS ENGINEERING
UNIVERSITI TEKNOLOGI PETRONAS
BANDAR SERI ISKANDAR,
PERAK**

FEBRUARY 2013

DECLARATION OF THESIS

Title of thesis Application Of Electromagnetic Waves And Zinc Oxide & Aluminum Oxide As Dielectric Nanoparticles In Enhanced Oil Recovery

I _____ NOOR RASYADA AHMAD LATIFF

hereby declare that the thesis is based on my original work except for quotations and citations which have been duly acknowledged. I also declare that it has not been previously or concurrently submitted for any other degree at UTP or other institutions.

Witnessed by

Signature of Author

Signature of Supervisor

Permanent address: _____
25, Laluan Desa Pengkalan 13,
Taman Desa Pengkalan
31500 Lahat, Perak

Name of Supervisor
Dr. Hasnah Mohd Zaid

Date : _____

Date : _____

ACKNOWLEDGEMENTS

Alhamdulillah, all praises to ALLAH Subhanahu Wa Ta’ala for the blessing and strength that He has given to me to search for the knowledge throughout completing this research project.

Along this challenging yet memorable journey, I believe I had gain a lot of experience and knowledge not only in physics stuffs such as nanotechnology, electromagnetism and enhanced oil recovery, but might as well learn about life, about people of diverse nationality and background and letting go of fear, especially towards walking out of the comfort zone and trying out new things in life. Thus, I would like to express my gratitude towards my mother who has always been supporting me all this while, even though she had no idea of what I was working on; her hope and belief in me give me strength to face the world. Thank you Mak, for your love and understanding.

Being surrounded by great people in the university makes nothing impossible to be done in research. Sincerest gratitude and appreciation goes to my research supervisor, Dr. Hasnah Mohd Zaid for her continuous assistance, support, and invaluable guidance throughout this research. I would also like to extend my gratitude to my former superior and co-supervisor, Professor Dr. Noorhana Yahya; for the employment opportunity, as well as the trust and belief you put in me to continue for MSc study. It was a mind blowing experience to work with both great physicists; with their great and novel ideas.

I also wish to thank Professor Dr. Birol Demiral as my field supervisor for his assistance and insightful discussions, as well as the employment opportunity in Enhanced Oil Recovery Centre, UTP. Me, being clueless about enhanced oil recovery in the early days; you slowly developed the knowledge and understanding in me,

especially in petroleum engineering domain through weekly seminars and discussions.
Thanks to you Prof!

I also would like to acknowledge the staffs and technicians of Central Analytical Lab, Electrical & Electronics Engineering Department, Fundamental & Applied Sciences Department, Mechanical Engineering Department and Chemical Engineering Department of Universiti Teknologi PETRONAS for their kindness and supportive encouragement throughout completion of this project.

Million thanks to all my fellow friends especially to Poppy, Baya, Khairil, Hajar and Jefferie whom always have been very supportive and helpful throughout this journey. Thanks for lending me your shoulders to cry on, guys! Finally, I would like to express my deepest gratitude to my late father Allahyarham Haji Ahmad Latiff Mahidin, Mohd Razif Zenudin, my brothers and my sister for their patience, open-mindedness, and endless support. Only Allah SWT can return your kindness and patience for all this time.

Many thanks to all others not mentioned here individually.

ABSTRACT

Recovering oil from reservoirs with high temperature and high pressure is impractical by using the existing methods. Therefore, injection of dielectric nanofluid activated by low frequency electromagnetic (EM) wave has been proposed to improve recovery efficiency of an oil reservoir. When subjected to an alternating electric field, change in the viscosity of the nanofluid gives better sweep efficiency during the core displacement tests. Dielectric nanoparticles namely ZnO and Al₂O₃ were synthesized using sol-gel method. Microstructural characterization confirmed that both nanoparticles have high purity and crystallinity; with average particle size of 38 nm and 45 nm for Al₂O₃ and ZnO, respectively. Displacement tests were conducted using packed silica beads to evaluate recovery efficiency of the nanofluid in comparison to the conventional surfactant, sodium dodecyl sulfate (SDS). Dielectric properties of the nanofluids e.g. relative permittivity, dielectric loss and loss tangent were characterized in a frequency range of 10² to 10⁶ Hz. At frequency 10² Hz, Al₂O₃ nanofluid has 45.3% higher dielectric losses than ZnO, which inferred the existence of higher surface charges bounded for occurrence of greater interfacial polarization. Furthermore, the electro rheological properties of the nanofluids were also studied by varying the presence of electromagnetic wave during the displacement tests. In the absence of EM irradiation, Al₂O₃ nanofluid recovered highest residual oil volume with 31.7% increment after 2 pore volumes injected in comparison with SDS. When subjected to EM irradiation, 81.7% more residual oil recovered by Al₂O₃ nanofluid in comparison to the case when no irradiation is present. Among these two nanofluids, Al₂O₃ gives 44.11% higher efficiency to recover the residual oil as compared to ZnO. It has demonstrated that change in the viscosity of dielectric nanofluids when irradiated with EM wave will improve sweep efficiency and hence, gives higher oil recovery.

ABSTRAK

Kaedah yang sedia ada tidak praktikal untuk memperoleh minyak dari reservoir yang bersuhu dan bertekanan tinggi. Oleh itu, suntikan bendalir nano dielektrik yang diaktifkan oleh gelombang elektromagnetik (EM) frekuensi rendah telah diusulkan untuk meningkatkan kecekapan perolehan minyak tersisa. Di dalam medan elektrik ulang alik, perubahan kelikatan bendalir nano memberikan kecekapan penyapuan yang lebih baik dalam ujian sesaran teras. Partikel nano iaitu ZnO dan Al₂O₃ telah disintesis melalui kaedah sol-gel. Pencirian mikrostruktur menunjukkan bahawa partikel-partikel nano memiliki ketulenan dan kehabluran tinggi, dengan anggaran ukuran partikel masing-masing dari 38 nm dan 45 nm untuk Al₂O₃ dan ZnO. Ujian sesaran dibuat menggunakan manik-manik silika terpadat untuk menilai kecekapan bendalir nano berbanding surfaktan konvensional, natrium sulfat dodesil (SDS). Sifat dielektrik bendalir nano seperti ketelusan relatif, kehilangan dielektrik dan tangen kehilangan dicirikan dalam julat frekuensi 10²-10⁶ Hz. Pada frekuensi 10² Hz, bendalir nano Al₂O₃ memiliki kerugian dielektrik 45.3% lebih tinggi dari ZnO, yang membuktikan kewujudan lebih banyak cas permukaan terbatas untuk lebih banyak peluang berlakunya pengutuban antara muka. Selain itu, sifat reologi elektrik bendalir nano juga dikaji dengan menjadikan kehadiran gelombang elektromagnetik sebagai pembolehubah di dalam ujian sesaran. Tanpa penyinaran gelombang EM, bendalir nano Al₂O₃ memberikan kenaikan 31.7% perolehan minyak tersisa setelah 2 isipadu liang disuntikkan, berbanding SDS. Dengan penyinaran EM, 81.7% lebih banyak minyak tersisa diperoleh dengan bendalir nano Al₂O₃ berbanding perolehan tanpa penyinaran. Di antara kedua-dua bendalir nano, Al₂O₃ mempunyai kecekapan 44.11% lebih tinggi untuk memulihkan minyak tersisa berbanding ZnO. Hal ini menunjukkan bahawa perubahan dalam kelikatan bendalir nano dielektrik ketika disinarkan dengan gelombang EM akan meningkatkan kecekapan penyapuan dan justeru, memberikan perolehan minyak tersisa yang lebih tinggi.

In compliance with the terms of the Copyright Act 1987 and the IP Policy of the university, the copyright of this thesis has been reassigned by the author to the legal entity of the university,

Institute of Technology PETRONAS Sdn Bhd.

Due acknowledgement shall always be made of the use of any material contained in, or derived from, this thesis.

© Noor Rasyada Ahmad Latiff, 2013

Institute of Technology PETRONAS Sdn Bhd

All rights reserved.

TABLE OF CONTENT

ABSTRACT	vii
ABSTRAK	viii
LIST OF FIGURES	xiii
LIST OF TABLES	xvi
LIST OF ABBREVIATIONS	xvii
LIST OF SYMBOLS/UNITS	xviii
CHAPTER 1 INTRODUCTION	1
1.1 Background of the Research.....	1
1.1.1 Stages in oil recovery	2
1.1.2 Challenges in the oil recovery	4
1.1.3 Selection of Feasible EOR Methods	5
1.2 Problem statement	6
1.2.1 Solution to the problems	7
1.3 Objective of the research	8
1.4 Scope of works	9
1.5 Overview of the thesis	9
CHAPTER 2 REVIEW OF LITERATURE AND THEORY	11
2.1 Trapping of oil in reservoir rocks	11
2.2 Mechanisms of EOR methods	13
2.2.1 Reduction in oil-water interfacial tension	13
2.2.2 Alteration of surface wettability	15
2.2.3 Improvement of the sweep and displacement efficiency	16
2.3 Nanotechnology in EOR.....	17
2.3.1 Solid particles as surfactant.....	22
2.3.2 Solid particles as rheology modifying agent	25
2.3.2.1 Physics of the electrorheological effect	27
2.4 Selection of materials	30
2.4.1 Metallic oxide nanoparticles	31
2.4.1.1 Aluminum oxide nanoparticles	32

2.4.1.2 Zinc oxide nanoparticles	33
2.5 Dielectric theory	34
2.5.1 Dielectric response with the applied frequency	37
2.6 Electromagnetic wave propagation theory	38
CHAPTER 3 METHODOLOGY	42
3.1 Synthesis of Dielectric Nanoparticles.....	44
3.2 Characterization of nanoparticles	46
3.2.1 Field Emission Scanning Electron Microscopy (FESEM).....	46
3.2.2 Energy Dispersive X-Ray (EDX).....	47
3.2.3 X-ray powder diffraction (XRD).....	48
3.2.4 Transmission Electron Microscope (TEM)	49
3.3 Nanofluid Preparation and Characterization	50
3.3.1 Preparation of Nanofluids	51
3.3.2 Dielectric properties measurement.....	51
3.3.3 Oil-aqueous phase interfacial tension (IFT) measurement.....	52
3.3.4 Viscosity Measurement	54
3.4 Electromagnetic Wave Transmission System	55
3.4.1 Scaled Model Calculation	55
3.4.2 Core Flooding Experimental Setup	57
3.5 Petrophysical Characterization	58
3.5.1 Fluids characterization	58
3.5.2 Reservoir rocks characterization	60
3.5.2.1 Permeability	60
3.5.2.2 Porosity	63
3.5.2.3 Fluid Saturation.....	64
3.6 Core Flooding Tests.....	66
CHAPTER 4 RESULTS AND DISCUSSIONS.....	69
4.1 Nanoparticles Characterization.....	69
4.1.1 Characterization of zinc oxide nanoparticles	69
4.1.1.1 Field Emission Scanning Electron Microscopy (FESEM)	70
4.1.1.2 X-Ray Diffraction (XRD)	72
4.1.1.3 Energy Dispersive X-Ray (EDX)	75

4.1.1.4 Transmission Electron Microscope (TEM)	75
4.1.2 Characterization of aluminium oxide nanoparticles.....	78
4.1.2.1 Field Emission Scanning Electron Microscopy (FESEM)	78
4.1.2.2 X-Ray Diffraction (XRD)	80
4.1.2.3 Energy Dispersive X-Ray (EDX)	82
4.1.2.4 Transmission Electron Microscope (TEM)	85
4.2 Nanofluid Characterization.....	87
4.2.1 Dielectric properties	87
4.2.1.1 Permittivity	87
4.2.1.2 Loss Factor.....	89
4.2.1.3 Loss tangent	90
4.2.2 Interfacial tension (IFT) measurement	91
4.2.3 Viscosity measurement	93
4.3 Petrophysical properties characterization	94
4.3.1 Reservoir fluid properties.....	94
4.3.2 Reservoir rock properties	95
4.4 Core Displacement Tests	96
4.4.1 Effect of nanoparticles addition into the base fluid.....	97
4.4.2 Effect of EM irradiation on the recovery efficiency	99
4.4.3 Pressure drop as an indication of viscosity change	104
CHAPTER 5 CONCLUSIONS	110
5.1 Conclusion	110
5.2 Recommendation	111
5.3 Main Contribution	111
5.4 List of Publications	112
APPENDIX A XRD DATA	125
APPENDIX B INTERFACIAL TENSION (IFT) MEASUREMENT.....	138
APPENDIX C CRUDE OIL INFORMATION	150
APPENDIX D OIL RECOVERY EVALUATION & CALCULATION	152

LIST OF FIGURES

Figure 1.1: World oil production by source in the Reference Scenario of World Energy Outlook 2008 [3]	2
Figure 1.2: Estimation of the recoverable and residual oil after primary and secondary recovery stages [10]	3
Figure 1.3: Influence of the reservoir depth on the applicability of EOR methods.....	5
Figure 1.4: Various EOR methods.....	7
Figure 2.1: The role of surface charge in oil displacement process.....	15
Figure 2.2: Role of polymer to reduce water fingering and improve sweep and displacement efficiency [34].....	17
Figure 2.3: Surfactant adsorption at the interface.....	23
Figure 2.4: Influence of contact angle on the adsorption of particles to the interface.	23
Figure 2.5: Variation of the energy required to remove a single spherical particle exhibiting a contact angle of 90° from a planar oil-water interface	25
Figure 2.6: Schematic illustration of the (a) ER particles and (b) the non-ER particles behaviors before and after applying external electric field [38]	26
Figure 2.7: Physical phenomena of the polarization processes [52].....	27
Figure 2.8: Increase in surface charge density enhances the interfacial polarization..	28
Figure 2.9: The structure of electro rheological systems	30
Figure 2.10: Phase formation of Al ₂ O ₃ [59].....	33
Figure 2.11: Parallel plate capacitor [65].....	35
Figure 2.12: Dielectric response of solids over a wide range of frequencies [68].....	38
Figure 3.1: Flow chart of the methodology	43
Figure 3.2: Synthesis of zinc oxide by sol gel method	45
Figure 3.3: Supra 55VP Zeiss Variable Pressure Field Emission Scanning Electron Microscope (VP-FESEM).....	47
Figure 3.4: Fundamental principle of elemental detection	48
Figure 3.5: Libra 200FE Zeiss Transmission Electron Microscope	50
Figure 3.6: Agilent 4294A Impedance Analyzer with 16451B Liquid Dielectric Fixture	52

Figure 3.7: SVT 20N DataPhysics Spinning Drop Tensiometer	53
Figure 3.8: The interface of SVTS 20 software for IFT calculation.....	54
Figure 3.9: Brookfield CAP 2000+ Viscometer	54
Figure 3.10: Schematic diagram of the transmitter-oil reservoir system.....	56
Figure 3.11: Schematic diagram of core flooding setup	58
Figure 3.12: Kinematic viscosity measurement device (a) Tamson Viscometer Unit TVB445 and (b) Capillary tube 1B.....	59
Figure 3.13: Linear flow model	61
Figure 3.14: Measurement column serves as unconsolidated cores for petro physical characterization and core flooding experiment.....	63
Figure 3.15: Stages of core flooding carried out for each EOR fluid	68
Figure 4.1: Variables considered in annealing process of ZnO nanoparticles.....	70
Figure 4.2:FESEM images for ZnO nanoparticles annealed at temperature (a).....	71
Figure 4.3: XRD pattern for ZnO nanoparticles annealed at temperature (a) 500°C, (b) 400°C, (c) 300°C, (d) 250°C and (e) 200°C	74
Figure 4.4: TEM micrographs of ZnO 300 dispersed in isopropanol (a) under magnification of 200,000 times and (b) diffraction line to determine the <i>d</i> -spacing ..	78
Figure 4.5: Variables considered in annealing process of Al ₂ O ₃ nanoparticles	78
Figure 4.6: FESEM images of Al ₂ O ₃ nanoparticles annealed at temperature (a) 900°C, (b) 1000°C and (c) 1100°C	79
Figure 4.7: Phase transformation of Al ₂ O ₃ xerogel after annealed at increasing temperature [71].....	80
Figure 4.8: XRD Pattern for (a) standard Al ₂ O ₃ nanoparticles and annealed at temperature (b) 1100°C, (c) 1000°C and (d) 900°C	81
Figure 4.9: TEM micrographs of Al ₂ O ₃ 1100 dispersed in isopropanol (a) under magnification of 200,000kX and (b) diffraction line to determine the <i>d</i> -spacing	86
Figure 4.10: Relative permittivity spectra of ZnO and Al ₂ O ₃ nanofluids measured in frequency sweep of 100 Hz to 4 MHz	88
Figure 4.11: Loss factor spectra of ZnO and Al ₂ O ₃ nanofluids measured in frequency sweep of 100 Hz to 4 MHz	89
Figure 4.12: Loss tangent spectra of ZnO and Al ₂ O ₃ nanofluids measured in frequency sweep of 100 Hz to 4 MHz	90

Figure 4.13: Dynamic IFT measurement of the injection fluids.....	93
Figure 4.14: Plot of kinematic viscosity versus temperature of the Arabian Heavy crude oil from 25°C to 80°C	95
Figure 4.15: Comparison of the incremental recovery versus pore volume injected of the base fluid and ZnO nanofluid.....	97
Figure 4.16: Comparison of the incremental recovery versus pore volume injected of the base fluid and Al ₂ O ₃ nanofluid.....	98
Figure 4.17: Comparison of the incremental recovery versus pore volume injected in the absence of EM waves for all injection fluids	99
Figure 4.18: Comparison of the incremental recovery versus pore volume of ZnO nanofluid injected in the presence of EM waves	100
Figure 4.19: Comparison of the incremental recovery versus pore volume of Al ₂ O ₃ nanofluid injected in the presence of electromagnetic wave	101
Figure 4.20: Comparison of the incremental recovery versus pore volume of both types of nanofluids injected in the presence/absence of EM waves	102
Figure 4.21: Effluent collected at the outlet during EOR fluid injections, from 0.1 until 2.0 pore volumes.....	103
Figure 4.22: Incremental oil recovery and pressure difference for 2 PV injection of Al ₂ O ₃ nanofluid	108
Figure 4.23: Incremental oil recovery and pressure difference for 2 PV injection of Al ₂ O ₃ nanofluid in the presence of EM irradiation	108
Figure 4.24: Incremental oil recovery and pressure difference for 2 PV injection of ZnO nanofluid	109
Figure 4.25: Incremental oil recovery and pressure difference for 2 PV injection of ZnO nanofluid in the presence of EM irradiation	109

LIST OF TABLES

Table 2.1: Six forces relevant in EOR	12
Table 2.2: Recent applications of nanotechnology in enhanced oil recovery.....	20
Table 3.1: Stoichiometric calculation of ZnO.....	46
Table 3.2: Stoichiometric calculation of Al ₂ O ₃	46
Table 3.3: Parameters calculated for designing the scaled experimental setup	57
Table 3.4: Details of the crude oil for viscosity measurement	59
Table 3.5: Glass beads mixtures of different combination, mixed at equal ratio	62
Table 4.1: Comparative values of crystal planes, d-spacing, lattice parameter, structure and crystallite size of ZnO nanoparticles annealed at various temperatures	73
Table 4.2: Elemental distribution analysis of ZnO nanoparticles annealed at various temperatures	76
Table 4.3: Comparative Values of Crystal Planes, d-spacing, Lattice Parameter, Structure, Crystallite Size of Al ₂ O ₃ Nanoparticles Annealed at Various Temperatures	82
Table 4.4: Comparison of Weight and Atomic Ratio from EDX Analysis of Al ₂ O ₃ Nanoparticles	84
Table 4.5: Dynamic interfacial tension value between crude oil and injection fluids.	92
Table 4.6: Kinematic viscosity of the injection fluid.....	93
Table 4.7: Viscosity of the Arabian Heavy crude oil with temperature variation	95
Table 4.8: Permeability and porosity of the glass bead packs	96
Table 4.9: Petrophysical Characterization and Recovery Evaluation.....	106
Table 4.10: Relationship between incremental oil recovery with the pressure drop .	107

LIST OF ABBREVIATIONS

EOR	: Enhanced Oil Recovery
HTHP	: High Temperature and High Pressure
ZnO	: Zinc oxide
Al ₂ O ₃	: Aluminum oxide
SDS	: Sodium Dodecyl Sulfate
OOIP	: Original Oil in Place
ROIP	: Residual Oil in Place
EM	: Electromagnetic
FESEM	: Field Emission Scanning Electron Microscope
TEM	: Transmission Electron Microscope
XRD	: X-Ray Diffractometer
EDX	: Energy Dispersive X-Ray
IFT	: Interfacial Tension
ER	: Electro rheological
DC	: Direct Current
HNO ₃	: Nitric acid
PV	: Pore Volume

LIST OF SYMBOLS/UNITS

cP	: centipoise
psi	: pound per square inch
Hz	: Hertz
ft	: feet
rpm	: rotation per minute
ml	: mililiter
g	: grams
°C	: degree Celcius
wt%	: weight percentage
ppm	: parts per million
m	: mater
min	: minute
s	: second
Å	: Angstrom ($= 1 \times 10^{-10}$ m)
mN/m	: miliNewton/meter (tension)
mD	: miliDarcy

CHAPTER 1

INTRODUCTION

This first chapter briefly discusses research motivation, introduction to the research idea, objectives, research scope and approaches to accomplish the objectives.

1.1 Background of the Research

Fossil fuels energy still remains an ultimate source of energy based on the energy density that it can offer, which is still unbeatable by any type of renewable energy, e.g. solar, hydro-turbine and biomass [1]. Dependence of the world survival on the oil and gas resources is clearly understood that even with a small change in the price of oil will create crisis i.e. increase of the price of consumer goods, increasing living costs and utility bills [2]. To make these situations worse, in the 2008 World Economic Outlook (WEO) oil production from the existing fields are decreasing and shows a declining trend in the discovery of the new conventional oil reserves, as shown in Figure 1.1 [3]. Conventional oil reserve is defined as an oil reserve that is economically recoverable by the existing technologies e.g. water-alternating-gas (WAG) injection, surfactant flooding and miscible carbon dioxide displacement. Problems are created when this so called ‘easy oil’ is depleted and the only option left is to look for unconventional oil reserves [4]. Usually, unconventional reserves are defined based on the geographical location of the reservoir and characteristics of the oil to be recovered [5]. If a reservoir buried more than 500 m below the seafloor is about to be considered, extreme variation in the reservoir pressure and temperature could bring harm to most of the existing method, especially methods involving insertion of foreign devices and chemicals, for instance. If oil characteristic is the main parameter to be considered, heavy oil requires more effort and better technology rendered by its highly viscous nature [6]. In an environment of more than 100°C, most

of the chemicals e.g. polymers and surfactants are not able to withstand the temperature and subsequently experience degradation which in turn reduced the efficiency of the method [7].

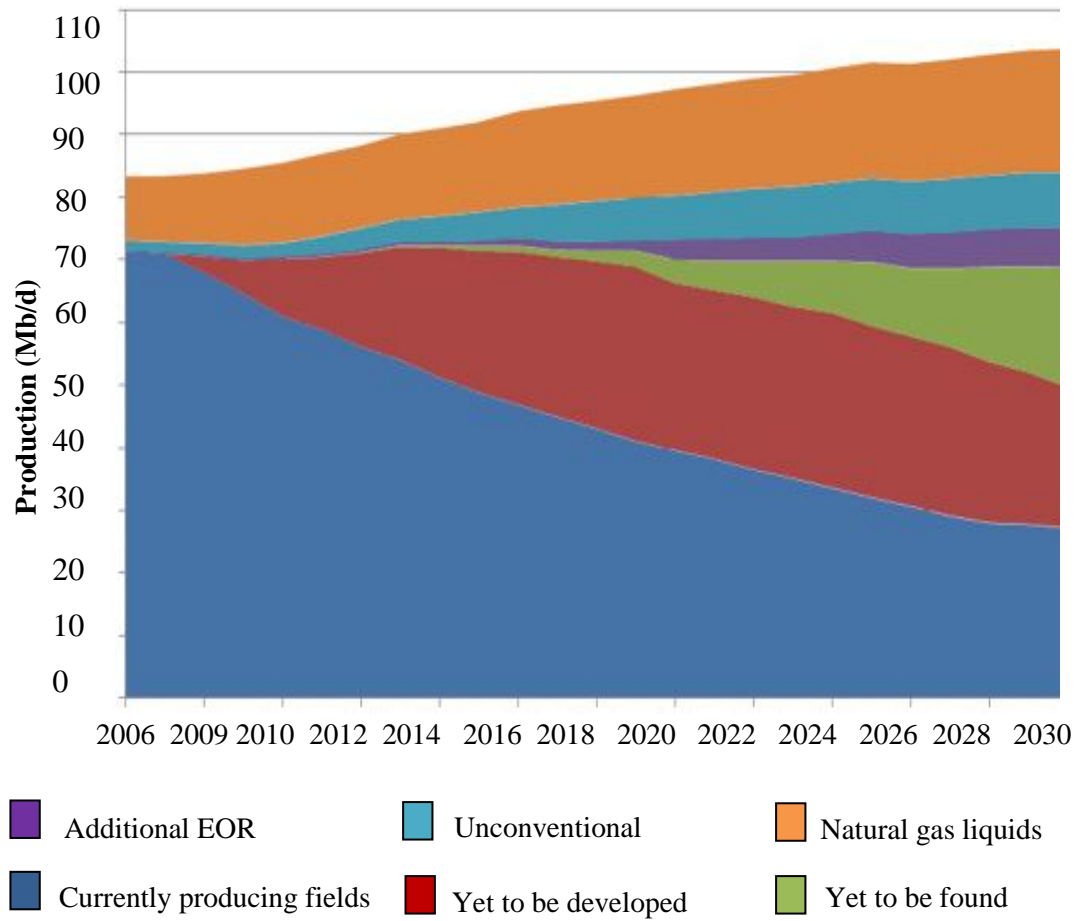


Figure 1.1: World oil production by source in the Reference Scenario of World Energy Outlook 2008 [3]

1.1.1 Stages in oil recovery

Life cycle of an oil reservoir consists of three major stages; primary, secondary and tertiary oil recovery stages as visualized in Figure 1.2. Primary recovery is the first oil that comes out once a well has been drilled. The natural pressures that exist due to the depth of the oil will force it to flow through the rock or sand formation toward the lower pressure wellbore, where it is lifted to the surface. Since it uses

natural forces to shift the oil, primary recovery is the least expensive method of extraction but typically recovers only 10 -15% of the original oil in place (OOIP) [8].

Secondary recovery methods come into application after the reservoir has lost its natural pressure to move the remaining oil. Water flooding has been applied as the most common technique which injects large volumes of water under pressure into the hydrocarbon-bearing zone to sweep some of the oil it encounters along with it as the water flows through the formation toward the producing wellbore [9]. An additional 10-20% of OOIP can be recovered by employing this technique, but has to be stopped when it reaches to a point where water flooding is no longer cost effective.

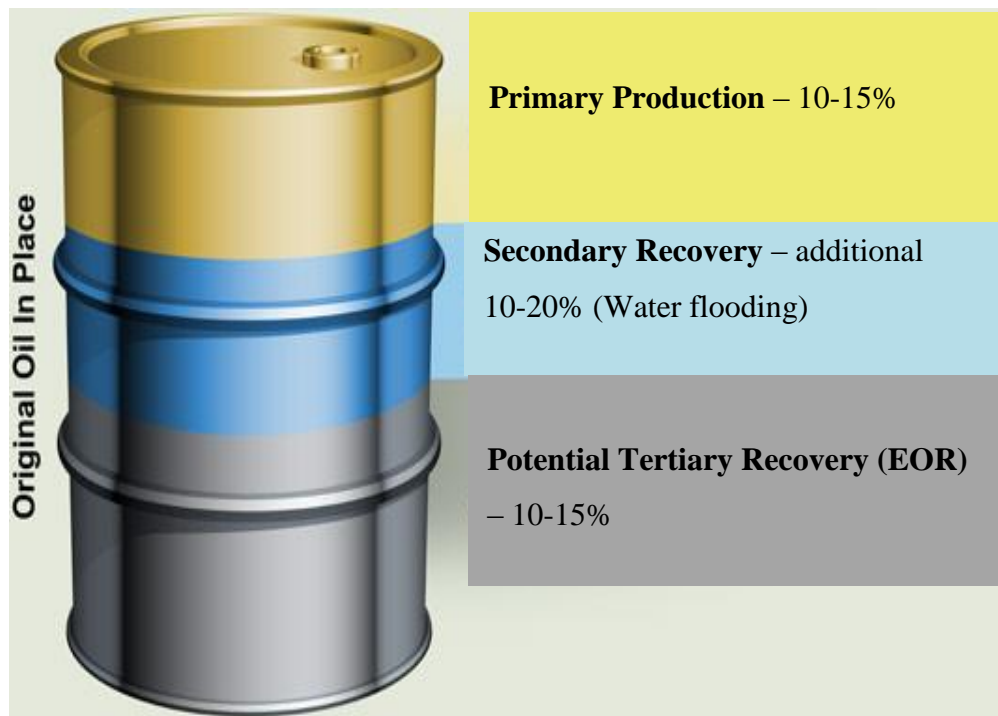


Figure 1.2: Estimation of the recoverable and residual oil after primary and secondary recovery stages [10]

Enhanced oil recovery (EOR) refers to the recovery of oil that is left behind in a reservoir after primary and secondary recovery methods, either due to exhaustion or no longer economical through application of thermal, chemical or miscible gas processes. At this point, tertiary recovery stage will be performed as a means to

extract the remaining oil that is still trapped in the reservoir by application of external agent, whichever applicable and appropriate with the reservoir condition. At present, on average only about 30 - 35% OOIP has successfully recovered after application of various methods mentioned above. Maximizing the production of an oil reservoir has become even more difficult and also costly, so approximately 65 - 70% is currently left behind [11].

1.1.2 Challenges in the oil recovery

There are two terms to describe the type of oil reservoir; conventional and unconventional. They are distinguished from each other based on their geographical location or the economics and also the physical character of the hydrocarbons [5]. Most of the existing oil reservoirs nowadays are maturing fields and categorized as the conventional oil reservoirs or ‘easy oil’. Conventional oil is simply defined as oil reservoir that is easily recoverable at low cost and without the need of applying advanced technology. However, this type of reservoir is depleted and most of the newly discovered reservoirs could be categorized as unconventional oil, e.g. heavy oil, tar sands, reservoir located deepwater region and high temperature and high pressure reservoirs [5]. Because of the continuous research and probably due to the extreme change of oil prices, unconventional oil reserves that were evaluated uneconomic to recover earlier are now considered as viable to produce oil.

As the depth of the reservoir increases, high pressure and high temperature (HTHP) environment is also present. Figure 1.3 shows the influence of the reservoir depth on the applicability of various EOR methods. Some methods work efficiently at increasing depth e.g. hydrocarbon miscible and fireflood, by manipulating the highly pressurized environment. However, this is limited to reservoirs with low water saturation and high oil saturation i.e. more than 600 barrels of oil initially present in the reservoir and has oil reservoir thickness of at least 1.5 meter .Chemical flooding methods are not feasible since most of the chemicals e.g. polymer and alkaline suffers degradation due to the extreme temperature created by the pressure at more than 2100 meter (7000 ft) depth. Since conventional methods are no longer applicable to

the extreme reservoir conditions e.g. reservoir with high temperature and high pressure, a new method with highly advanced technology has to be designed.

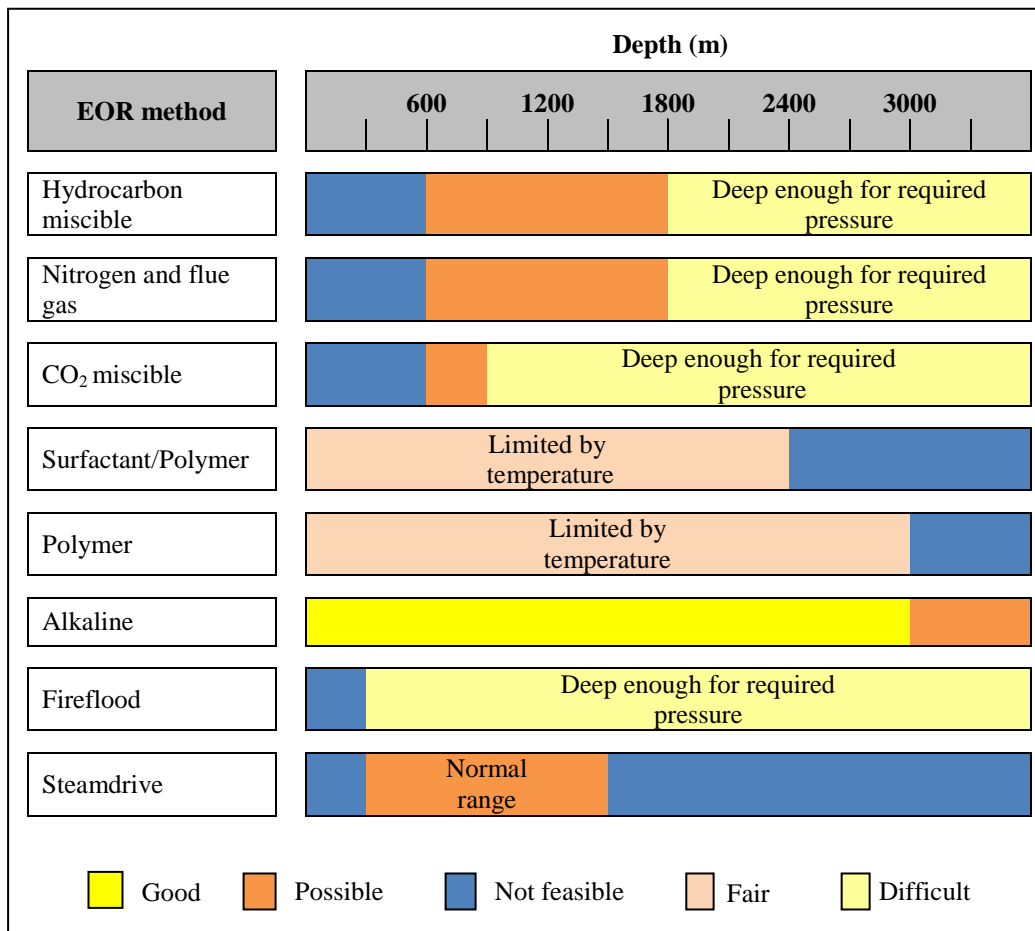


Figure 1.3: Influence of the reservoir depth on the applicability of EOR methods

1.1.3 Selection of Feasible EOR Methods

In order to recover oil from high pressure and temperature reservoirs, consideration has to be taken on methods which have applicability to operate at these extreme conditions. As depicted in Figure 1.4, various potential EOR methods can be considered in the screening stage to fit in the reservoir conditions. One of the criteria might be a non-invasive approach, which implies that insertion of any physical or external stimulating devices into the reservoir should be avoided. For instance, electrical heating method requires electrodes to be inserted into the reservoir to

undergo resistive Joule heating of the reservoir materials, as the current passed through highly resistive region. If this method is going to be considered in extreme temperature region, resistance in the electronics circuit will be very high and may bring failure to the circuit. Thermal expansion may damage downhole equipment and cause cement failure. Microwave heating also has similar problem, but with greater severity since it requires a huge installation density of the antenna to provide higher volume of effectiveness or coverage area, attributed to the low penetration depth of high frequency electromagnetic wave [12,13].

Other criteria that should be considered are the sustainability of the agent in the extreme pressure and temperature environment. In this case, agent is the injectant or external fluid to be injected into the reservoir to stimulate oil recovery. In chemical flooding, chemical e.g. surfactant and polymer was used to reduce interfacial tension between oil and water interface and also to increase the sweep efficiency of the displacing fluid, respectively. However, these chemicals are not able to withstand high temperature. At elevated temperatures in aqueous solution, partially hydrolyzed polyacrylamides (HPAM) experience hydrolysis of amide side groups over 8 years at 100°C and about 2 years at 120°C [14, 15]. Other methods, as shown in Figure 1.4 will be discussed further in the next chapter.

1.2 Problem statement

As mentioned earlier in this chapter, there are two major criterions that have to be taken into consideration to design a new EOR method that is suitable for HTHP environment. Invasive approach e.g. insertion of electrode or any stimulating devices in extreme temperature and pressure environment will cause failure to the electronic circuits and the device itself. Injection of external stimulating agents or fluids into the reservoir under this extreme condition is not feasible when their stability could not be sustained and degraded with increasing temperature and pressure.

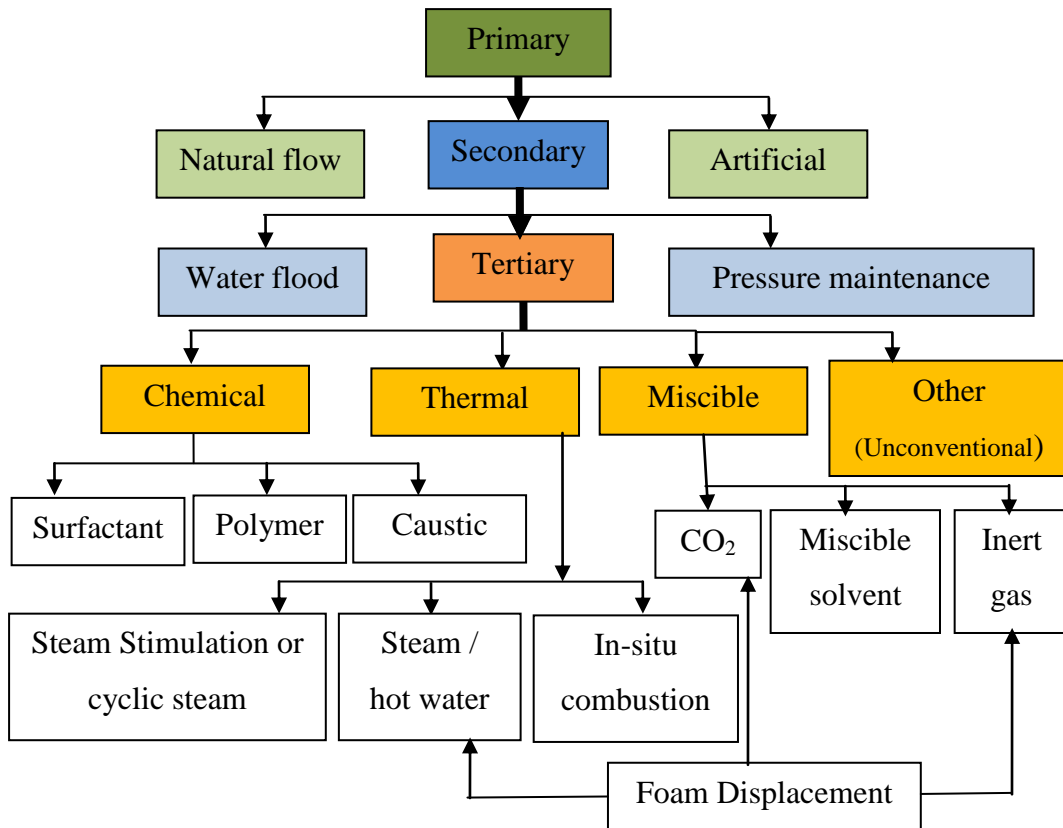


Figure 1.4: Various EOR methods

1.2.1 Solution to the problems

These problems could be treated by employing a method that can withstand HTHP environment. Non-invasive approach to stimulate oil in the reservoir could be applied with the application of low frequency electromagnetic (EM) wave. This is due to the fact that at low frequency, penetration depth of the wave will be higher and therefore, transmitter is not necessarily located in the wellbore. This research proposed that low frequency EM wave may be located on the seafloor and transmitter EM energy remotely.

To stimulate oil production from the target oil reservoir, dielectric nanoparticles suspension will be injected into the porous medium and activated by the low frequency EM wave. Usage of nanotechnology in this research may have potential to enhance this proposed method, due to interaction at molecular level. Dielectric will be polarized in electric field and create highly dense charges on the surfaces, creating

surface active interfaces. Interaction of charges at the interfaces will disturb the compatibility between oil/water/rock interfaces and therefore oil can be released more easily. Therefore, two types of dielectric materials namely zinc oxide, ZnO and aluminum oxide, Al₂O₃ have been proposed for this study. Both of them are widely employed in the industry for various applications e.g. optoelectronic devices, electromagnetic wave shield, radio-frequency (RF) communication materials and insulators for heating system [16, 17]. Interesting and unique properties of these nanomaterials could be tailored to meet specific requirement and application, by preparing them using enormous methods e.g. sol gel, hydrothermal, co-precipitation and combustion, to name a few [16, 17, 18]. Among all methods, sol gel has been identified as the synthesis method to be used in this study based on the high repeatability and ability to control morphology, structure and uniform size distribution of the end products; by varying the precursor composition, solvent type, annealing temperature, etc [19].

1.3 Objective of the research

The main objective of this study is to validate the feasibility of electromagnetically stimulated dielectric nanoparticles in recovering oil from an oil reservoir. Therefore, specific objectives have been outlined to meet the target:

1. To determine the optimum annealing temperature for the formation of single phase, highly crystalline nanoparticles by synthesizing Al₂O₃ and ZnO nanoparticles using sol gel method with variation in annealing temperature and characterize the as-synthesized nanoparticles.
2. To identify the frequency at which material shows highest dielectric constant and loss factor for maximum interfacial polarization by measuring dielectric properties of the nanoparticles suspensions at low frequency region.

3. To obtain the difference in the percentage of residual oil being recovered by nanoparticles suspensions in the presence and absence of EM wave irradiation by conducting core flooding experiments.

1.4 Scope of works

The scope of this research works will include synthesis and characterizations of two different types of metal oxides nanomaterial; ZnO and Al₂O₃ for EOR purpose. These nanomaterials were synthesized by using sol-gel method. Micro structural properties of ZnO and Al₂O₃ were analyzed using XRD, FESEM, EDX and TEM.

Both nanomaterials were then dispersed into base fluid to form colloidal suspension and characterized for their dielectric properties. Following to this step is designing the experimental setup for the measurement of oil recovery with and without irradiation of EM wave. Prior to the evaluation of oil recovery, the porous medium was prepared and characterized for its petro physical properties e.g. porosity, permeability and pore volume. Properties of the oil used in this experiment were also characterized e.g. dynamic viscosity and density.

Feasibility of this proposed method were tested in a water bath, consist of a column of porous medium connected with inlet and outlet tubing which were channeled to the respective pumps and effluent collector. Experiments were conducted at temperature 60°C and ambient pressure, by varying the presence of EM field during the core displacement tests.

1.5 Overview of the thesis

This thesis consists of five main chapters. Chapter 1 provides an overview about enhanced oil recovery stages. Chapter 2 outlines the reviews of several works that have been carried out previously, as well as the theoretical literature to support this research work. Methodology used in carrying out the research is covered in Chapter 3. Chapter 4 presents the results and discussion of the work. Last but not least, this work

will be summarized and concluded, as well as outlining future research recommendations in Chapter 5.

CHAPTER 2

REVIEW OF LITERATURE AND THEORY

In this chapter, theoretical aspect of the electromagnetic waves propagation and their interaction with matter will be discussed as well as the fundamental knowledge on the EOR processes and recovery mechanisms, especially at surface and molecular level. Relevant works by other researchers will also be discussed to understand the current scenario of the methods applied in the industry.

2.1 Trapping of oil in reservoir rocks

Usually after water flooding, large amount of oil is expected to be trapped in the reservoir rock pores in the form of discontinuous oil ganglia due to the capillary forces. Oil recovery is dependent on the assembly of dispersed, disconnected residual oil into macroscopic and mobile oil banks. Traditional oil recovery understanding is focusing on three major forces that acted on the oil ganglion, namely capillary, viscous and gravitational forces. If nanotechnology is concerned, it has to be focused on the nanoscale forces: Coulombic interaction and disjoining forces. Table 2.1 elaborates six types of forces relevant in EOR by outlining their nature and mechanisms. EOR is dependent on processes at the nano-scale in addition to micro and macro scales. At the nano-scale, the pore shape, mineralogy, roughness, water distribution and surface film behavior dominate oil recovery [20].

Although oil recovery needs to overcome capillary forces, it is the boundary conditions (pore geometry and wettability) and instability of the associated interfaces that govern the oil displacement at the micro scale. Trapping of oil in water-wet systems occurs due to the localized viscous or buoyancy forces which are unable to overcome the large capillary forces at small pore throats that exist when the interfacial tension is high.

Table 2.1: Six forces relevant in EOR

Force	Nature of Force
Coulombic	The intermolecular forces. These comprise van der Waals (VDW) forces: induced dipole (London), dipole-dipole and hydrogen bond. If polar molecules and ions are present then ion-dipole and ionic bonding forces exist
Disjoining	Forces associated with thin films due to the departure from bulk properties arising from the influence of the surfaces. Includes steric and electrical double layer forces as well as VDW forces
Marangoni	Forces that arise due to a gradient in a property such as concentration or interfacial tension
Capillary	Forces resulting from the curvature of fluid interfaces which yields pressure differences between different fluid phases
Viscous	Forces associated with the viscosity contrast of fluids and responsible for the displacement efficiency of one fluid by another
Gravity	Forces responsible for water-oil separation on the macroscopic scale due to density differences and hence, buoyancy effects

2.2 Mechanisms of EOR methods

Tertiary oil recovery or often regarded as EOR can be divided into three major groups, namely thermal, miscible and chemical methods. Steam flooding, in-situ combustion, and EM heating are some of the EOR processes that fall into thermal method. Thermal energy is transferred into the reservoir to heat up the oil formation and therefore reducing oil viscosity for easier displacement. Meanwhile in miscible flooding method, various types of solvents were used to fully mix up with the residual oil to overcome capillary forces and hence, increase oil mobility. Liquefied petroleum gas (LPG), nitrogen, carbon dioxide and alcohol are some of the solvents that have been used in the industry. In chemical flooding, polymers, surfactants and alkalis were mixed up with water before injection. Target range of crude oil to be recovered using this method is in between the range of heavy oil that is recoverable by thermal flooding and light oil that is recoverable by miscible flooding. Chemical flooding methods work either by reducing interfacial tension between oil and water, increasing sweep efficiency or changing wettability of the rock surfaces. Detail explanation on the recovery mechanism will be discussed in the following subsection.

2.2.1 Reduction in oil-water interfacial tension

Residual oil present in the water flooded zones is believed to be in the discontinuous oil ganglia form which is trapped in the reservoir rock pores. Viscous forces and the capillary forces are the two major forces acting on the oil ganglia, the ratio of which is represented by the capillary number [21]. At the end of water flooding stage, the capillary number N_{cap} is around 10^{-8} to 10^{-7} and has to be increased by an order of at least two to three magnitudes to enable additional oil recovery. Capillary number, N_{cap} can be increased by increasing the viscosity of the displacing fluid or by lowering interfacial tension as shown in Equation 2.1,

$$N_{cap} = \frac{v\mu}{\gamma} \quad (2.1)$$

where v is the Darcy velocity in m/s, μ is the viscosity of injected phase in Pa·s and γ is the interfacial tension (IFT) of the oil phase-aqueous phase in N/m [22].

One way to achieve lower IFT is injecting chemical e.g. alkali and surfactant into oil reservoir and alter the stability at the oil-water interfaces. In alkaline flooding by injection of NaOH or NaHCO₃ solution, Dong et al (2010) has demonstrated the reaction of alkalis with the acidic components in crude oil to produce interfacial species in-situ which results in lower IFT value [23]. In another work, Hirasaki et al (2008) has pointed out the possibility to achieve very low residual oil saturation (<0.05) by reducing oil-water IFT from a typical value of 20-30 mN/m to the values ranging from 10⁻² to 10⁻³ mN/m in surfactant flooding. Surfactant is dissolved in either water or oil to form micro emulsion; a middle phase form in between oil and aqueous phase due to the solubilisation effect which in turn forms a mobilized oil bank [24]. Abhijit et al (2011) has successfully increased recovery to approximately 20% OOIP by injecting 0.5 pore volumes aqueous solution of 0.3 wt% SDS [25]. However, Dong et al (2010) has demonstrated that ultra-low IFT value obtained by combining alkaline with surfactant shown better recovery efficiency than those obtained from alkaline or surfactant flooding alone. When 0.1 wt% NaOH is added into 100 ppm of surfactant solution, IFT value has reduced from 28 to 0.036 mN/m, to give additional 2.5% OOIP recovered in the core flooding test as compared to NaOH-only flood [23].

High surface charge density at the oil-water interface minimizes the re-attachment of the crude oil droplets to the negatively charged sand particles and hence more droplets would come out of the porous media. Therefore, Chang et al (1978) suggested that minimum interfacial tension and interfacial viscosity would increase the deformability of drops to come through narrow necks of pores and also promote the coalescence of droplets thus resulting in higher oil recovery efficiency [26]. Based on the experimental works done by Bansal et al (1978), it was found that the occurrence of maximum electrophoretic mobility due to high surface charge density at the crude oil-alkali interface corresponds to the minimum in the interfacial tension. When concentration of NaOH solution does not exceed 0.5 wt%, ionization of the carboxylic group (RCOO⁻) which naturally present in the crude oil will occur and caused sudden increase in the charge density at the interface, which in turn will increase electrophoretic mobility [27].

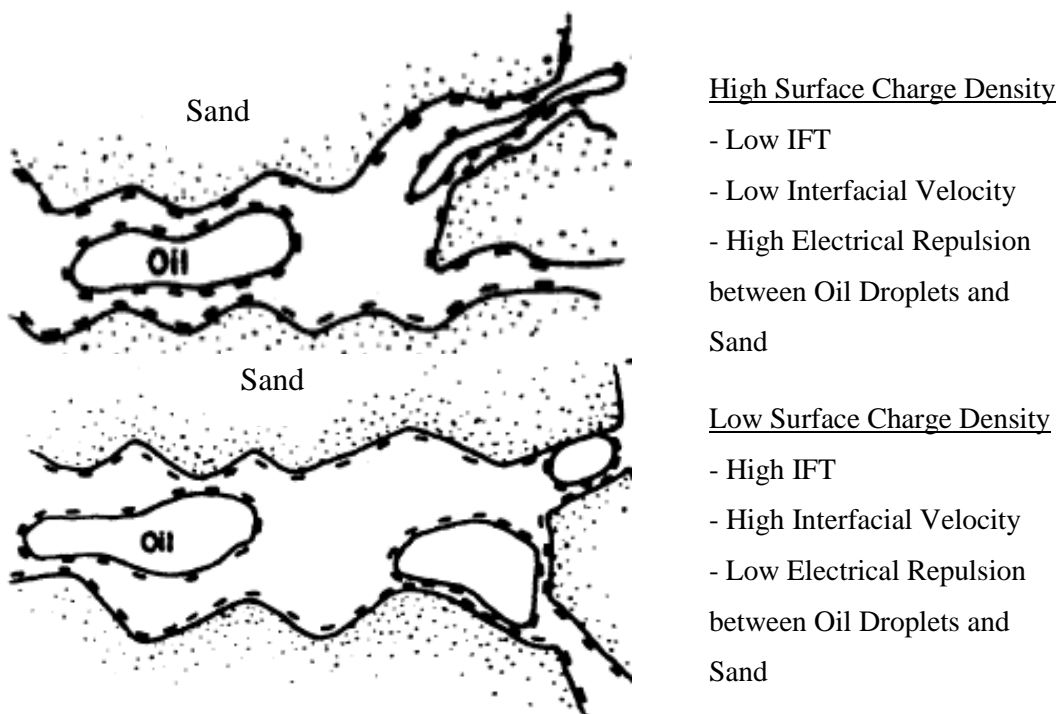


Figure 2.1: The role of surface charge in oil displacement process

2.2.2 Alteration of surface wettability

Wettability is known as the relative tendency of fluid to wet a solid surface in the presence of another fluid that coexists in a system. Alteration of surface wettability is believed to cause additional oil production from unconventional and depleted oil reservoirs. In a research conducted by Roosta et al (2009), wettability alteration works in two ways; either by changing the wetting state from oil-wet to water-wet and increase oil production by preventing the re-imbibitions of oil into the pores, or by changing a strongly oil-wet rock to have neutral wettability, giving rise to higher oil production in non-fractured reservoirs [28].

It is generally accepted that application of surfactant into the oil reservoir may change the wettability of the reservoir rock by the formation of ion-pair which in turn facilitates the adsorption of surfactant molecules onto the crude oil adsorbed on the rock surfaces [23]. Apparently, applying chemicals is not the only way to achieve wettability alteration of the reservoir rocks. Few studies [29, 30] on thermal EOR

methods stated the feasibility of thermal energy to induce change in the wetting state of the rocks. Al-Hadhrami and Blunt (2000) have reported that thermal energy may induce desorption of surface active components of the crude oil known as asphaltenes from the rock surface, rendering it to be more water-wet and hence, displace the oil [29].

2.2.3 Improvement of the sweep and displacement efficiency

Sweep efficiency is a measure of how effective is an EOR process that depends on the volume of the reservoir contacted by the injected fluid. It depends on various factors e.g. reservoir thickness, permeability, mobility ratio, density difference between the displacing and the displaced fluid, and flow rate [31]. Adverse mobility ratio between crude oil and water causes injected water to finger through reservoir, to leave behind a huge amount of reserves and hence give low recovery. Mobility ratio, M as defined in Equation 2.2 is the mobility of the displacing fluid (water) to the mobility of the displaced fluid (oil),

$$M = \frac{k_{rw}}{k_{ro}} \frac{\mu_o}{\mu_w} \quad (2.2)$$

where k_{rw} is defined as relative permeability to water, k_{ro} is relative permeability to oil, μ_o and μ_w are the viscosity of oil and water in cP, respectively. $M < 1$ is the favourable value during fluid injection. Addition of polymer increases the viscosity of the displacing water and reduces permeability of the porous media, allowing for an increase in the vertical and areal sweep efficiencies for higher oil recovery [32]. By increasing the viscosity of the aqueous phase, reduction of the mobility ratio is achieved for better mobility control. Application of partially-hydrolyzed polyacrylamides aqueous solution of 0.4 wt% in a laboratory core flood studies by Wang and Dong (2007) changed the viscosity of brine (initially 1 cP) to 40 cP and hence recovered 14.3 %OOIP in the tertiary recovery stage [33]. Another main accepted mechanism of mobile residual oil after water flooding is that there must be a rather large viscous force perpendicular to the oil-water interface to push the residual oil [25].

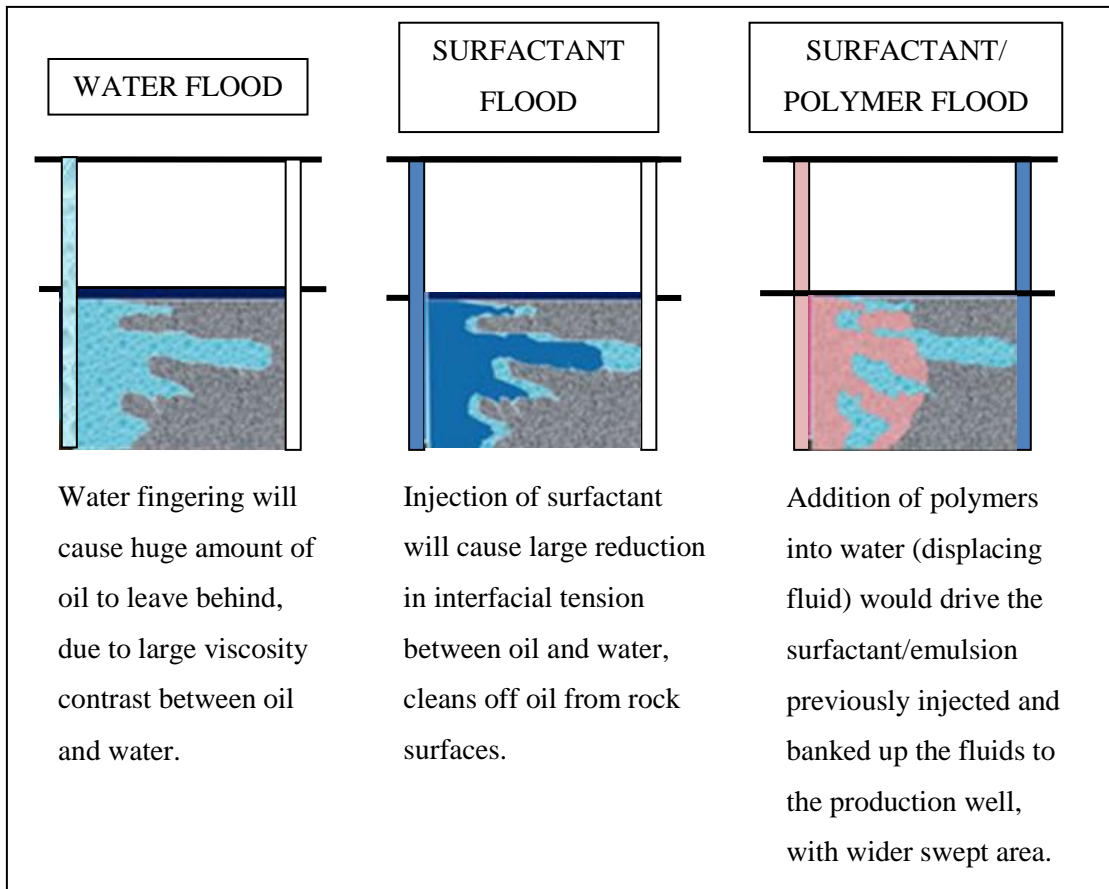


Figure 2.2: Role of polymer to reduce water fingering and improve sweep and displacement efficiency [34]

2.3 Nanotechnology in EOR

Drilling, drill-in, completion and stimulation fluids used in drilling and production operations are a complex system that consists of a fluid phase, a solid phase and a chemical phase [35]. Other than water and oil phases, the solids, chemicals and polymers that are used in the fluid design play an important role in the functional behavior of the fluids. The application of nanotechnology in oil and gas industry, especially in EOR is not a new thing. The ability of nanotechnology to manufacture tailor made nanomaterials with specific characteristic properties is expected to play a leading role in overcoming the technical and environmental challenges faced during drilling and production. Their superior behavior of nanomaterials are greatly

dependent on the grain boundary, surface area per unit mass/volume, purity, perfection, size and shape which are created during the synthesis and production stages [35]. High surface area-to-volume ratio caused only small concentration of nanoparticles necessary to create a new stimulation fluid, with superior behavior [36].

A detail explanation by Binks (2002) highlighted the possibility of solid particles to act similarly like low molar mass surfactants and surface-active polymers in preparation of emulsions and foam stabilization. Definite difference in their behavior is to be anticipated that individual particles do not assemble to form aggregated structures in the same way that surfactant molecules form micelles, thus no solubilization effect is present [37].

Another way to employ particles in EOR processes is by utilizing the electro rheological properties of solid particles suspensions, such that its rheology will be altered under the influence of electric field [38]. Recently, Ahmad Latiff et al (2011) have demonstrated more than 30% increase in the incremental recovery with ZnO and Al₂O₃ nanofluids. When subjected to 59.96 MHz EM wave, both nanofluids showed increment in their apparent viscosity which in turn enhanced sweep efficiency for greater oil recovery [39]. Dispersion of magnetic iron alloy nanoparticles in synthetic oil.

Wettability alteration of reservoir rock surfaces, emulsion and foam stabilization, interfacial tension reduction and etc are some of the ways to use nanoparticles in enhanced oil recovery. A recent work by Ali Karimi et al (2012) has proved that zirconium oxide, ZrO₂ nanoparticles suspension can change an oil-wet carbonate system to become water-wet by changing the surface free energy as the nanoparticles being adsorbed onto the solid surfaces. Quick imbibitions of the nanofluids into the core plugs recovered about 50% OOIP in just half a day [40]. In another study using 5 nm silica nanoparticles dispersed in aqueous solution, foam generated by co-injecting the nanofluid of 0.05 wt% concentration with CO₂ shows two to eighteen times more resistance to the flow as compared to the foam generated without nanoparticles [41]. Soleimanov et al. (2011) has successfully demonstrated 70-79% of reduction in oil-water interfacial tension with less than 0.01 wt% non-ferrous metal nanoparticles concentration dispersed in aqueous sulphuric acid solution. The tremendous IFT reduction was facilitated by the adsorption of nanoparticles onto the sand surfaces which tends to stabilize the physical and chemical adsorption process at the interfaces [42]. Reviews

on the relevant research works are summarized in Table 2.2 for clearer comparison. Theoretical explanation on the effect of nanoparticles presence on fluid-fluid interfaces will be covered in the next subsection.

Table 2.2: Recent applications of nanotechnology in enhanced oil recovery

Author(s)/ Year	Nanoparticles type	Dispersant/ Carrier	Average Particles Size	Mechanism	Results	Reference
Binks (2002)	Not mentioned	Not mentioned	6 to 184 nm	Stabilizing emulsion	Highly adsorbed due to high interfacial energy	[37]
Binks (2002)	Not mentioned	Not mentioned	<6 nm	Reducing IFT	Particles behave as surfactant	[37]
Zitha (2002)	Magnetic Fe alloy particles	Synthetic oil	~0.5-5.0 μm	Improve sweep efficiency/ increase viscosity	Rheological parameters change to gel type behavior in applied magnetic field	[43]
Onyekonwu et. al (2010)	Polysilicon Nanoparticles	Water/ethanol	10-60 nm	Wettability change, IFT Reduction	38.8% more oil recovered in EOR stage	[44]

Suleimanov et al (2011)	non-ferrous metal (0.001 wt%)	0.05 wt% sulphanole-alkyl aryl sulfonates	90-110 nm	70-90% more reduction in surface tension	1.5 fold incremental oil production compared to surfactant	[42]
Zaid, Ahmad Latiff, Yahya, Demiral (2011)	ZnO, Al ₂ O ₃	0.3 wt% sodium dodecyl sulfate	40-45 nm	Improved sweep efficiency by increase in viscosity	Al ₂ O ₃ gives the highest recovery of ~50% ROIP with EM irradiation	[39]
Karimi et al. (2012)	ZrO ₂	Non-ionic surfactants (Tween 80, glycerin, Span 20, 80, 85, etc)	24 nm	Wettability change	Recovered 50% OOIP in 12 hours due to imbibition	[40]

2.3.1 Solid particles as surfactant

As the surfactant is added to the equal volume of oil phase and aqueous phase, the molecules will accumulate at the interface and make partition between these two phases, where the hydrophilic head resides in water and the hydrophobic tail tends to reside in non-polar phase i.e. oil in this case. Hydrophilic surfactant will preferentially reside in the aqueous phase, where the monolayer tends to curve around oil, giving rise to oil-in-water emulsion. In contrast, larger portion of lipophilic surfactant monolayer is solvated by oil and curve around water, therefore water becomes the dispersed phase in water-in-oil emulsion [37, 45]. At a threshold value called critical micelles concentration (CMC), further addition of surfactant molecules will cause aggregation of the surfactant molecules to occur, which is known as micelles, as presented in Figure 2.2.

Unlike surfactants, particles do not have specific area of which is hydrophobic and hydrophilic. In the case of spherical particles which adsorbed to the interfaces, contact angle, θ which the particle makes with the interface is the most important parameter to be considered [37]. Hydrophilic particles e.g. metal oxides will normally have contact angle of $< 90^\circ$, therefore most of the particle surface remains in the water (polar phase) rather than in oil (non-polar phase). Hydrophobic particles such as treated silica tend to reside in oil compared to water since the contact angle is greater than 90° . In comparison with the surfactant molecules, the monolayer formed in between of oil and water phase tend to curve such that most of the particle surface remains on the external side; forming oil-in-water emulsions when θ is less than 90° or water-in-oil emulsions when θ is greater than 90° , as depicted in Figure 2.3.

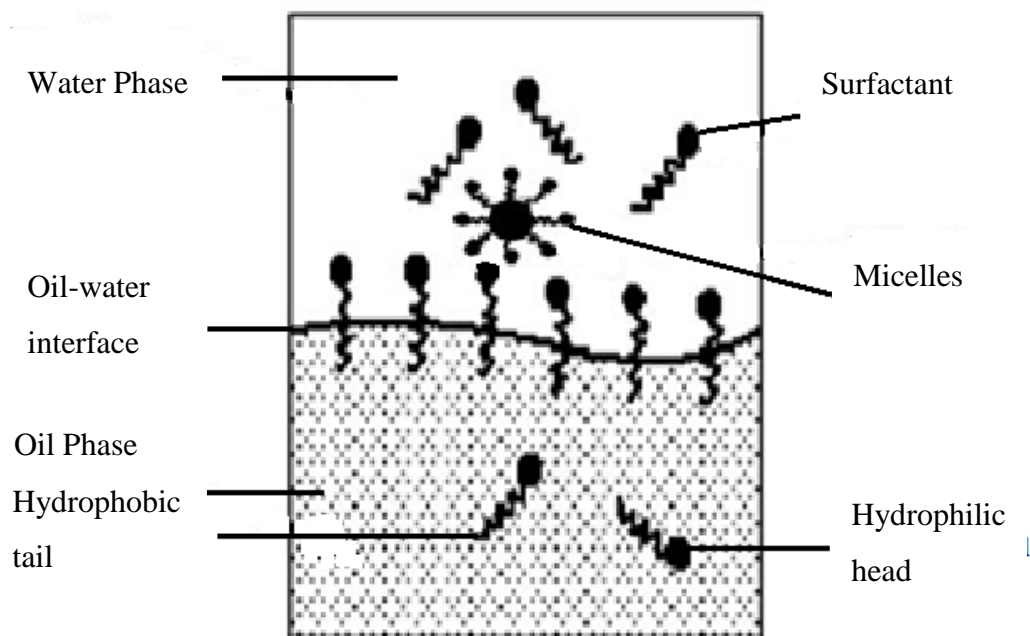


Figure 2.3: Surfactant adsorption at the interface

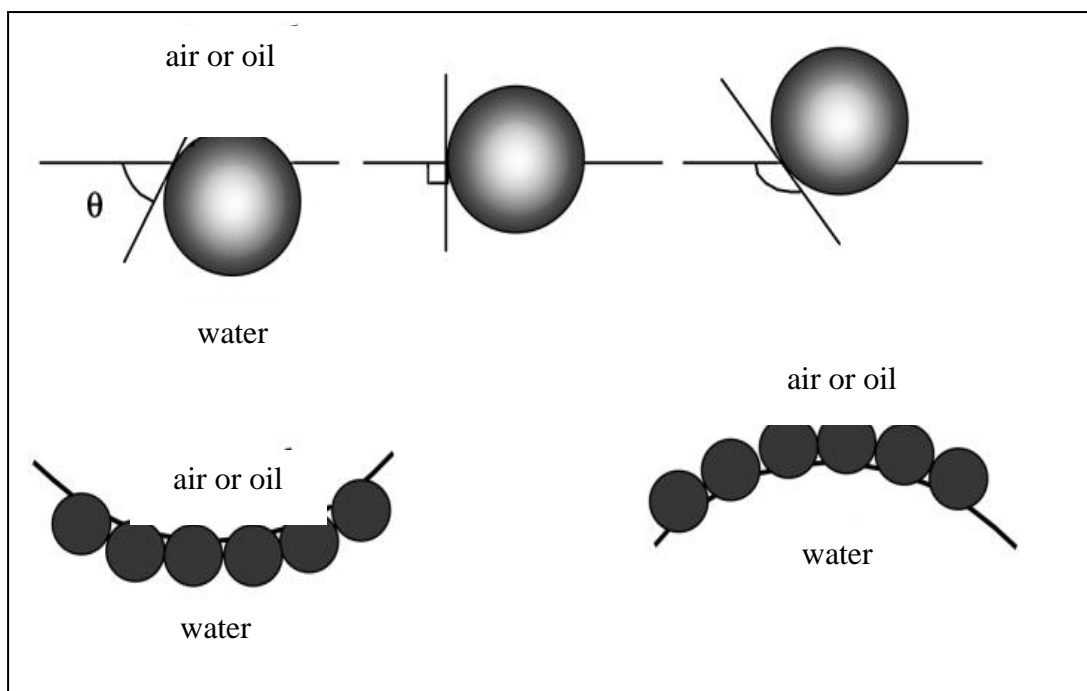


Figure 2.4: Influence of contact angle on the adsorption of particles to the interface

When a spherical hydrophobic or hydrophilic particle of radius r is strongly attached to the fluid α -fluid β interfaces, it require an energy, E which is related to the contact angle, θ and interfacial tension between two fluids, $\gamma_{\alpha\beta}$. In order to remove the particle from the interface, energy E required is given by Equation 2.3,

$$E = \pi r^2 \gamma_{\alpha\beta} (1 \pm \cos \theta)^2 \quad (2.3)$$

where hydrophilic particles having $\theta < 90^\circ$ will take negative sign in the bracket and positive sign will be applied for hydrophobic particles with $\theta > 90^\circ$. The extreme variation of this energy of removal with wettability indicates the ability of hydrophobic particles to stabilize emulsions. This is due to the high energy of interface, which is sharply contrasted to surfactant molecules which adsorb and desorb on a relatively fast timescale. Binks (2002) has pointed out that energy of removal is directly proportional to the square of the particle radius, thus lower energy is required as the particle size grows smaller and smaller, as shown in Figure 2.4. If the particle is so small (< 0.5 nm in radius) which is comparable to the surfactant molecules, the energy of detachment is only of several kT and may not works efficiently as stabilizers [37].

It was not new that particles could somehow behave like surfactant in certain condition. Binks (2002) has demonstrated that as particles grow smaller than 6 nm, it has the tendency to be adsorbed and desorbed on a relatively fast timescale, exhibiting surfactant-like behavior [37]. Therefore, nanosize particles could be used as a substitution of the surfactant whenever extreme environment is considered. However, nanoparticles of diameter ranging from 6 to 184 nm will caused IFT values to remain constant or slightly increase with concentration, which has greater adsorption at the interface to make it suitable for stabilizing emulsion, a phenomenon called Pickering emulsion [46]. In surfactant-polymer flooding by Wang et al (2010), entrapment of emulsion having various size of oil droplets caused the subsequent fluid injection to be diverted to other paths and hence, improving sweep efficiency [47]. Although it is a common practice in the industry to disperse micron-sized particles into emulsion for enhanced stability, it is not suitable for

reservoir application since pore clogging will occur and damage the reservoir permeability [48].

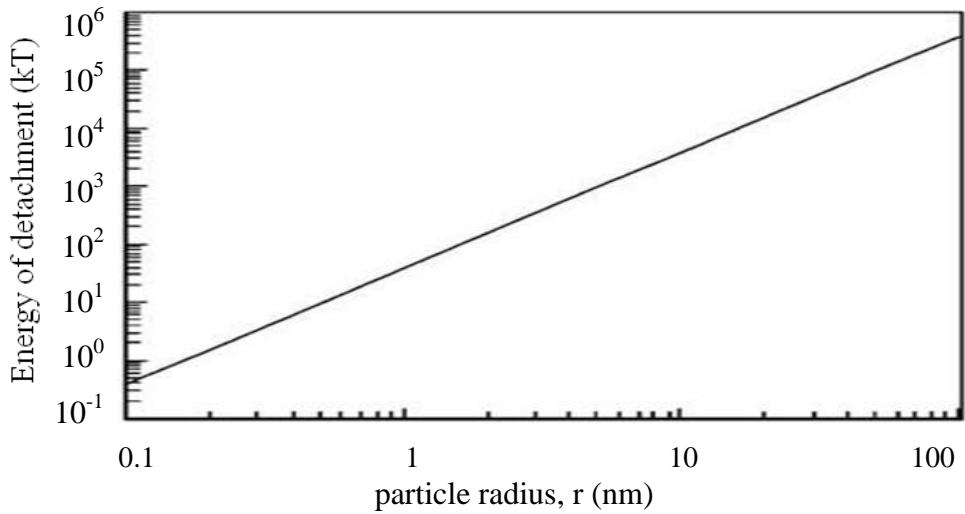


Figure 2.5: Variation of the energy required to remove a single spherical particle exhibiting a contact angle of 90° from a planar oil-water interface

2.3.2 Solid particles as rheology modifying agent

Although the application of polymers has found beneficial to the oil production, at some extent the recovery rate will decline due to the entrapment of polymer in pore spaces. Huh et al (1990) found that loss of mobility control will take place since polymer molecule was not able to propagate a longer distance [49]. In agreement to this problem, Skauge et al (2010) has observed that log-jamming caused the particles to block pores larger than the particle size due to the difference in the mass of particles and the solvent. Heavier particles will be accumulated at the entrance of the pore throats since less heavier water molecules will accelerate faster and caused blocking to the pore throat [50].

If viscosity of the displacing fluid can be altered in-situ, problems associated with the injection of high viscosity fluid into the reservoir may be eliminated. Few studies on liquid or solid particles suspension have exhibited rheological modification with the application of electric field or magnetic field [51, 43, 38]. In his study, Tian Hao (2002) has explained in detail the electro rheological (ER) effect; an effect that caused

the viscosity of the suspension to increase due to the formation of fibrillated network formed when polarized molecules re-orientated along the direction of the applied electric field. Two dynamic processes take place in electro rheological fluid; the ability of the particles to polarize and the capability to align along the direction of the electric field. The former is determined by the dielectric constant while the latter depends on the dielectric loss. The ability of particles to align and re-orientate with the applied field distinguished the ER materials from non-ER materials, although both of them could be polarized under an electric field as presented in Figure 2.6. This could be attributed to the high dielectric loss tangent, approximately around 0.1 at 1000 Hz, therefore large amount of bound surface charge would be generated at the interfaces to make it surface active [38].

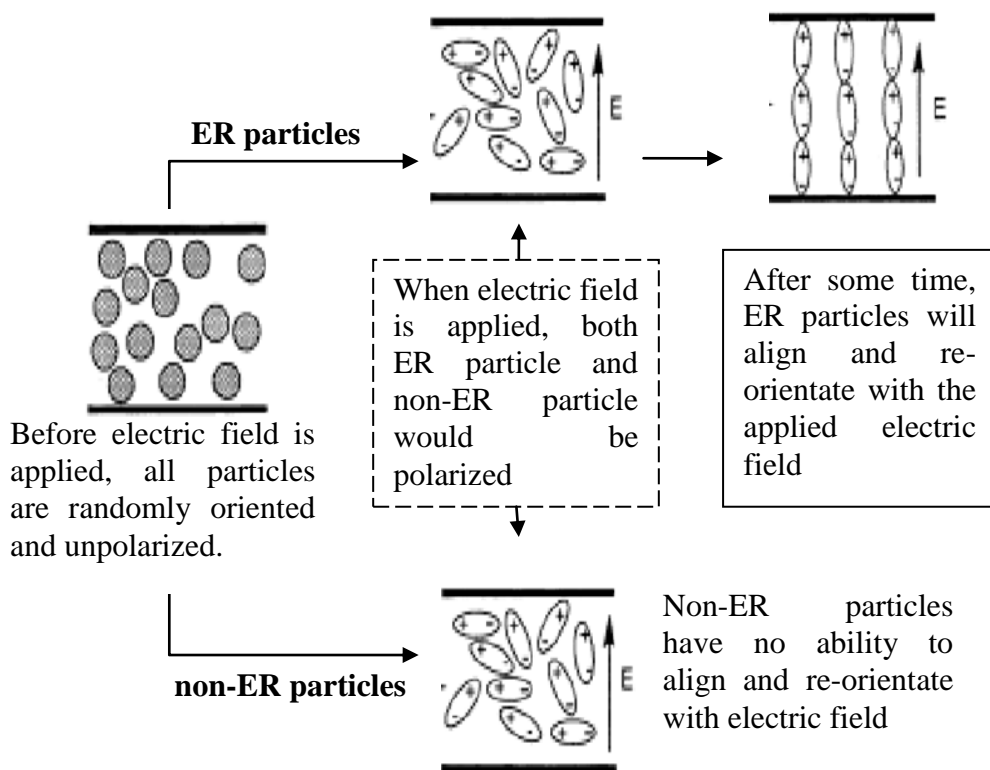


Figure 2.6: Schematic illustration of the (a) ER particles and (b) the non-ER particles behaviors before and after applying external electric field [38]

2.3.2.1 Physics of the electrorheological effect

Various polarization processes are responsible for the ER effect to occur. There are four types of polarizations i.e. electronic, atomic, Debye and interfacial polarization or also known as the Maxwell-Wagner polarization. The Debye and interfacial polarization usually appear at low frequency region, which are also known as the slow polarizations, whereby electronics and atomic polarizations usually take place at high frequency region. Permittivity of dielectric materials inferred the sensitivity of a medium to an electric field, which may attributed to these physical phenomena, wholly or partially; the displacement of the electronic cloud of atoms, the coherent orientation of electric dipoles and polarization effect at the interfaces, as presented in Figure 2.7.

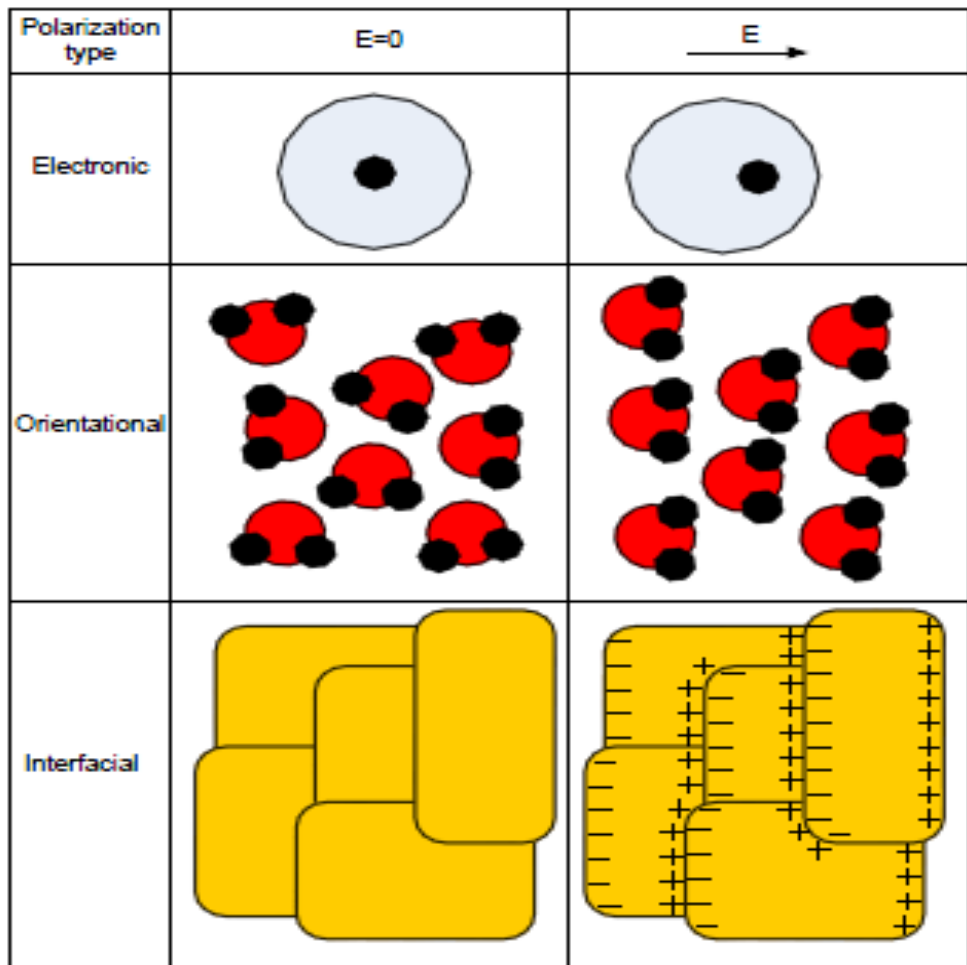


Figure 2.7: Physical phenomena of the polarization processes [52]

Hao and his co-workers have demonstrated that interfacial polarization, rather than other types of polarization, would contribute to the ER effect of the materials. The material, which has a large dielectric loss, could give a large interfacial polarization once it is dispersed into a liquid, namely, a large dielectric loss is required for a good ER material [53]. A general composition of an oil-field rock, sketched in Figure 2.8 shows the presence of free charges and interfaces to take into account the Maxwell-Wagner polarization effect. When electric field is applied, increase in the surface charge density at the interface can be observed, which greatly enhances the interfacial polarization.

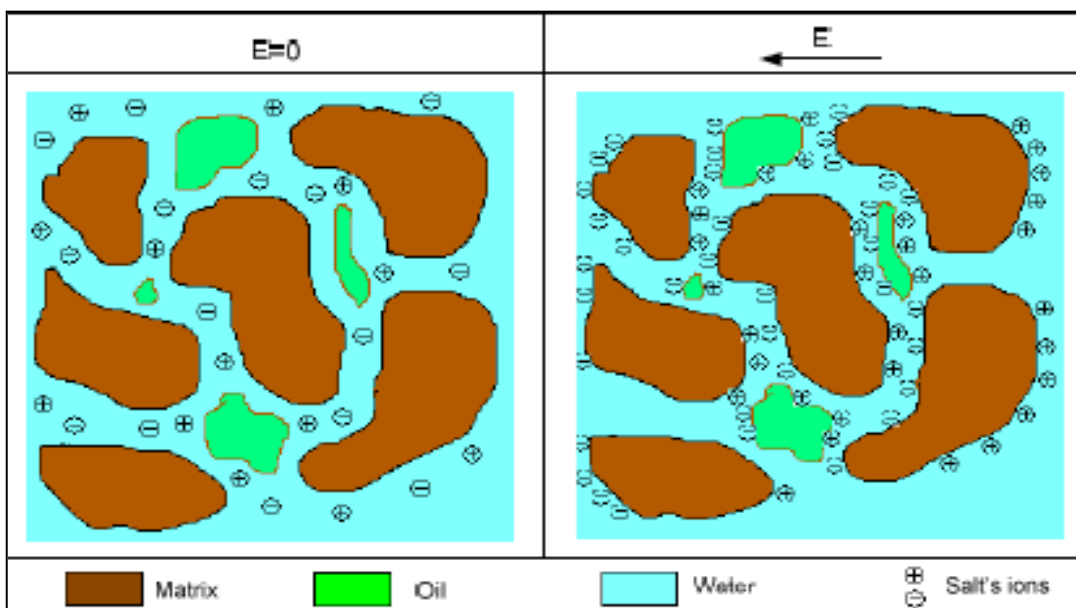


Figure 2.8: Increase in surface charge density enhances the interfacial polarization

In one of his studies, Hao (2002) concluded that particle surface properties give rise to the ER effect, specifically the large dielectric loss which contributes to the large interfacial polarization [38]. By understanding the physics of polarization processes, total polarization of heterogeneous material, P , is given by Equation 2.4,

$$P = P_I + P_D + P_A + P_E \quad (2.4)$$

where P_I , P_D , P_A and P_E stand for the interfacial, Debye, atomic and electronic polarization, respectively. Hence, the total dielectric constant, ε can be expressed as shown in Equation 2.5,

$$\begin{aligned}\varepsilon &= \varepsilon_s + \varepsilon_I + \varepsilon_D + \varepsilon_A + \varepsilon_E \\ &= \varepsilon_s + \varepsilon_I + \varepsilon_D + \varepsilon_\infty\end{aligned}\quad (2.5)$$

where ε_I , ε_D , ε_A and ε_E stand for the dielectric constant induced by the interfacial, the Debye, the atomic and the electronic polarizations, respectively. The high frequency dielectric constant, ε_∞ is represented by $\varepsilon_\infty = \varepsilon_A + \varepsilon_E$ and the static dielectric constant is given by ε_s . Dielectric constant and the dielectric loss are dependent on each other, the ratio of which is represented by dielectric loss tangent. If the dielectric loss originated from the slow polarization at low frequency region, high frequency dielectric constant, ε_∞ is negligible. Debye contribution could be neglected as well since dipole orientation is almost impossible for solid particles due to rigidity in the lattice. Thus, Equation 2.4 can be expressed as Equation 2.6;

$$\varepsilon = \varepsilon_s + \varepsilon_I \quad (2.6)$$

Large ratio between ε_s and ε infers that the solid particles suspension has a large dielectric loss tangent, which results in the large interfacial polarization. To explain the increase in apparent viscosity of the fluid, it is important to understand the dependence of apparent viscosity with the dielectric constant which correspondingly decreases with the increase in frequency applied. Smoluchowski has derived Equation 2.7 to express apparent viscosity, η ;

$$\eta = \eta_m \left\{ 1 + 2.5\phi \left[1 + \frac{1}{\sigma\eta_m r^2} \left(\frac{\zeta\varepsilon_m}{2\pi} \right)^2 \right] \right\} \quad (2.7)$$

where η_m represents the viscosity of the continuous phase, ϕ is the particle volume fraction, σ is the conductivity of the suspension, r is the particle radius, ζ is the zeta potential of the particle, ε_m is the dielectric constant of the continuous phase. However, there exists a few restrictions to apply this equation based on the

assumptions that was made during the derivation; (a) the suspension is dilute (ϕ is less than 10%) and (b) no overlapping between the electrical double layers (EDL) [38].

2.4 Selection of materials

Electrorheological (ER) effect can be found in a liquid or solid particles suspension under the application of an external electric field, with the observable changes in the rheological or structural properties e.g. apparent viscosity, yield stress and shear modulus [38, 54, 55, 56]. Figure 2.9 shows the structure of the ER system which consists of a liquid phase, a dispersed phase and an additive. In this research, inorganic metallic oxide has been used as the dispersed phase to create a heterogeneous ER fluid.

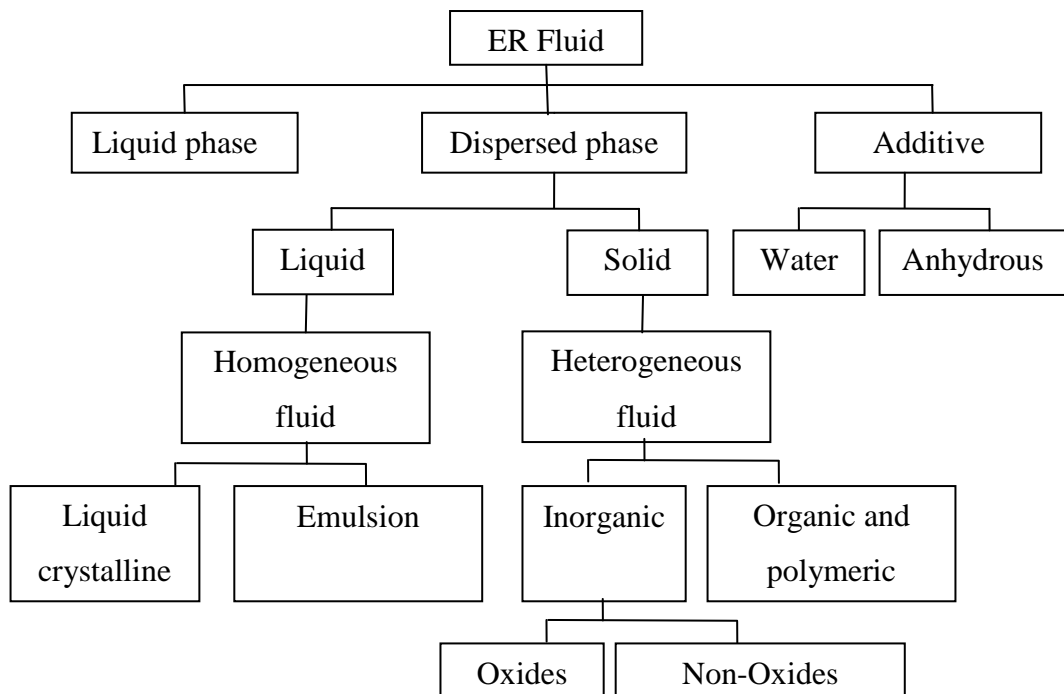


Figure 2.9: The structure of electro rheological systems

The water bridge mechanism was proposed by Stangroom (1983) to explain ER fluids [55]. He thought that a good ER fluid should meet the following requirements: (a) the liquid medium must be hydrophilic and the solid particles must be water-like and (b) porous material with the capability of adsorbing and keeping some amount of water; and (c) the water amount on the particle surface would determine the ER effect. Under an electric field, ions from water could move out of pores and migrate from one particle to another; therefore an adhesive water bridge could be formed between particles. Zhou et al (2010) have validated the role of adsorbed water to positively build up the ER effect of zeolite nanoparticles suspended in oil. For general ER fluids, the function of the adsorbed water was primarily assumed to improve particles interaction by increasing the permittivity of the dispersed particle. Secondly, high surface tension of water caused the particles to stick together, giving rise to the mobility of cations in the pores and on the surface of zeolite particles. Increase in the interfacial polarization give rise to the increase in dielectric loss, which results in the improvement of the turning ability of zeolite particle in silicone oil under the application of electric field [56].

Jianbo Yin (2006) found that the suspension stability of the nano-whisker TiO₂ ER fluid in the absence of additive was much better than that of the nano-spheres. No significant sedimentation observed due to the large length-to-diameter ratio of the nano-whiskers, while aggregation of nano-spheres caused sedimentation occurred in nano-spheres ER fluid. Under electric field, this nano-whisker ER fluid showed notable ER activity with dynamic yield stress of about 1.1 kPa at 3 kV mm⁻¹ and 10% particle volume fraction, which surpassed the yield stress (80 Pa) of ER fluid made of the raw material of TiO₂ nano-particles [57].

2.4.1 Metallic oxide nanoparticles

Recent developments of ER fluids are mostly focused on the anhydrous type due to the limitations faced by the aqueous ER fluids. Presence of water caused the aqueous ER fluids to have narrow working temperatures due to water evaporation at elevated temperatures, high current density due to higher conductivity of water, as well as erosion by water [38].

However for enhanced oil recovery purpose, erosion problems that associated to the water usage is not applicable anymore since water and other aqueous solution have been widely used in the reservoirs for stimulation purpose. Water-based fluids are more convenient to handle in terms of logistics and also injectivity of the fluids into the reservoirs. It is well known that the microstructure, surface properties, and composition of the particles, which would influence the physical and chemical natures of a material, are essential to the dielectric and polarization properties of the material. Therefore, it is possible to modify a material's dielectric and polarization properties by adjusting the synthetic procedure such that an ER material having a desired microstructure and composition can be produced [53]. In the following subsections, properties of dielectric metal oxides e.g. aluminium oxide, Al_2O_3 and zinc oxide, ZnO will be studied.

2.4.1.1 Aluminum oxide nanoparticles

Corundum ($\alpha\text{-Al}_2\text{O}_3$) is the thermodynamically stable morph of aluminum oxide (alumina, Al_2O_3). Being one of the most used inorganic materials in the chemical industry, alumina is widely used as adsorbents, catalysts or a catalyst support, and surface coatings in various industrial fields. Alpha alumina exhibits high chemical and mechanical stability at temperatures up to 1000°C and melting point of 2053°C. It has excellent mechanical hardness and abrasive resistance. The extent to which these properties are realized depends on various factors e.g. chemical composition, the structure and the microstructure of the layers obtained. Alumina is known to exist in several transient, meta-stable structures which include the γ -, η -, θ -, δ - and κ - phases. Alpha series are a group of alumina structures formed in alpha and kappa phases with hexagonal closed-pack (hcp) stacking of oxygen atoms, whereas gamma series consist of gamma, theta, eta and delta phases having face-centered cubic (fcc) stacking of oxygen atoms.

The $\alpha\text{-Al}_2\text{O}_3$ structure can be visualized as layers of hexagonal close-packed oxygen atoms with small Al atoms in two-thirds of the holes between the oxygen atoms coordinated in octahedral form. The atomic positions consist of 12 aluminium

atoms and 18 oxygen atoms. Even though the primitive unit cell of $\alpha\text{-Al}_2\text{O}_3$ is rhombohedral (spacegroup R-3c (No. 167)), it is commonly used to be described with the hexagonal symmetry in the literature. The unit cell dimensions are: $a = b = 4.7588 \text{ \AA}$ and $c = 12.992 \text{ \AA}$ [58].

In addition to the type of phase formed, the properties of the nanoparticles also depend on the features of the microstructure (porosity and cracks). An improvement in the properties takes place with increasing annealing temperature, as shown in Figure 2.10 [59].

Application of Al_2O_3 in oil and gas industry is not new. Porous material e.g. modified silica-alumina has been used for the removal of hydrogen sulfide, H_2S , a type of sour gas present in oil reservoirs. Al_2O_3 based material is chosen due to the chemical inertness and textural stability upon high temperature application [60; 61].

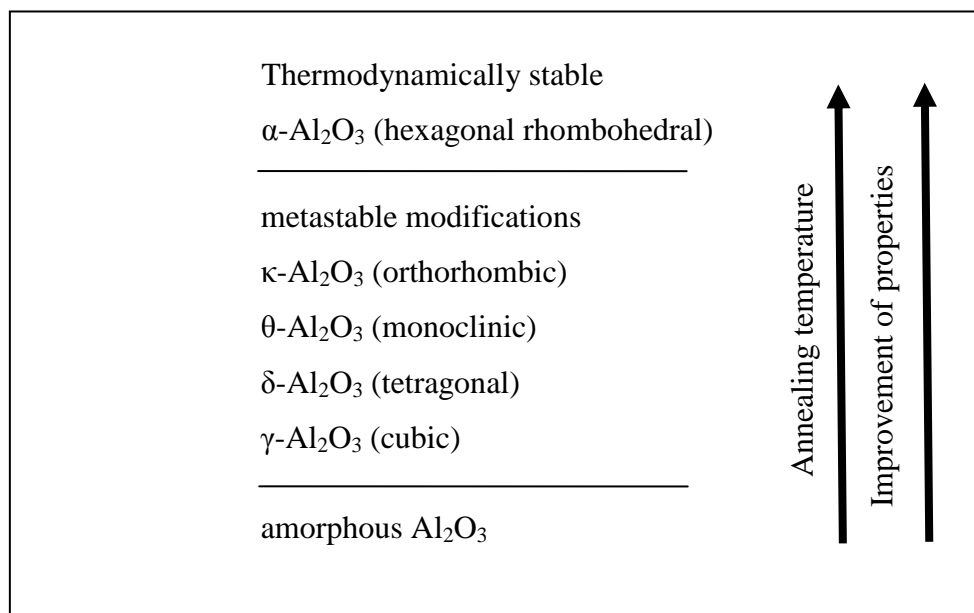


Figure 2.10: Phase formation of Al_2O_3 [59]

2.4.1.2 Zinc oxide nanoparticles

ZnO is a compound of group II and IV elements which has borderline ionicity due to their location in the periodic table, bridging the gap between covalent and ionic

semiconductors. It may crystallize into one of these crystal structures; zinc blende (B3), wurtzite (B4) and rock (Rochelle) salt (B1). Thermodynamically stable structure of ZnO is wurtzite; therefore most of the ZnO crystals exist under ambient condition will have this crystal structure. For a typical binary compound of Group II and IV, every atom of Group II will be surrounded by four atoms of Group IV, or vice versa, forming coordination at the edges of a tetrahedron [62]. Details of the crystal structures are shown in Figure 2.12.

Zinc oxide belongs to the space group P₆3mc in the Hermann-Maguein notation, having a hexagonal unit cell with two lattice parameters; *a* and *c*. The lattice constants mostly range from 3.2475 to 3.2501 Å for the *a*-parameter and from 5.2042 to 5.2075 Å for the *c*-parameter. The *c/a* ratio varies in a slightly wider range, from 1.593 to 1.6035, which typically has the value of 1.633 for ideal wurtzite structure. The deviation from that of the ideal wurtzite crystal is probably due to lattice stability and ionicity [62].

Zinc oxide, ZnO has been widely used for luminescence and photocatalytic due to its wide band gap and high exciton binding energy [63, 64]. It will crystallize to hexagonal structure when annealed at temperature 300°C and beyond, to give the most stable wurtzite phase [39]. Due to the dominant semiconducting nature of ZnO, it starts to conduct electricity when temperature applied is high enough to promote lattice vibration and create phonon-phonon interaction to make it behave as a conductor. For the current application, dielectric properties of the nanomaterials are the most significant properties to be considered. It is desirable to create interaction between dielectric particles and elements present in the oil reservoir with the application of electric or electromagnetic field.

2.5 Dielectric theory

Dielectric is defined as a material with an ability to store energy when an external electric field is applied. If a DC voltage source is placed across a parallel plate capacitor, dielectric material will store more charges between the plates compared to a

vacuum. The dielectric material increases the storage capacity of the capacitor by neutralizing charges at the electrodes, which ordinarily would contribute to the external field. The capacitance with the dielectric material, C is related to the capacitance of a vacuum, C_0 , the ratio of which is represented by the real part of dielectric constant, κ' or also known as relative permittivity, ϵ_r' , as indicated in the following equation.

$$\kappa' = \epsilon_r' = \frac{C}{C_0} \quad (2.8)$$

If a DC voltage source V is placed across a parallel plate capacitor, as presented in Figure 2.11, more charge is stored when a dielectric material is placed between the plates than if a vacuum is placed between the plates.

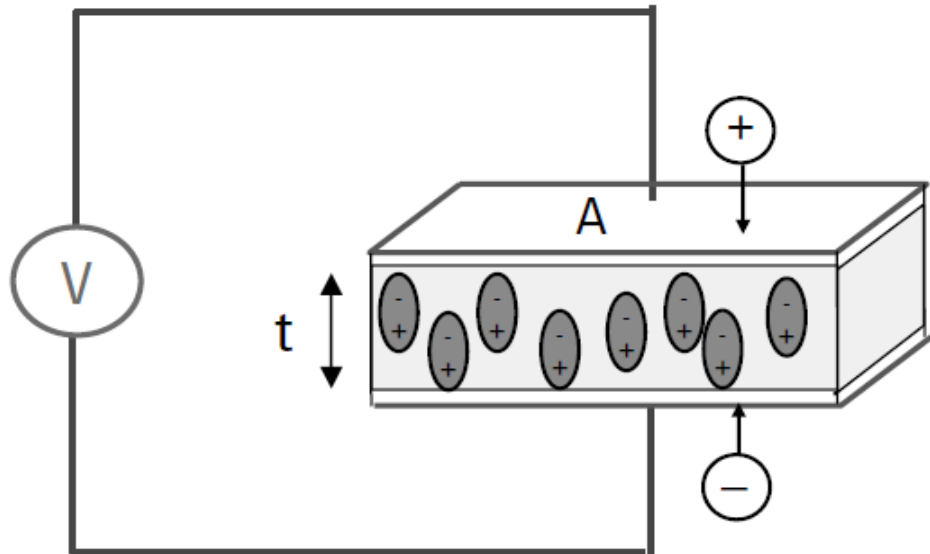


Figure 2.11: Parallel plate capacitor [65]

The complex dielectric constant κ consists of a real part κ' which represents the storage capacity and an imaginary part κ'' which represents the loss. The following notations are used for the complex dielectric constant interchangeably,

$$\kappa = \kappa^* = \epsilon_r = \epsilon_r^* \quad (2.9)$$

From the point of view of electromagnetic theory, the definition of electric displacement (electric flux density) D_f is:

$$D_f = \epsilon E \quad (2.10)$$

where $\epsilon = \epsilon^* = \epsilon_0 \epsilon_r$ is the absolute permittivity (or permittivity), ϵ_r is the relative permittivity, $\epsilon_0 \approx 1/36\pi \times 10^{-9} F/m$ is the permittivity of free space and E is the electric field. Permittivity describes the interaction of a material with an electric field E and is a complex quantity.

Dielectric constant (κ) is equivalent to relative permittivity (ϵ_r) or the absolute permittivity (ϵ) relative to the permittivity of free space (ϵ_0), as shown in Equation 2.10. The real part of permittivity (ϵ_r') is a measure of how much energy from an external electric field is stored in a material. The imaginary part of permittivity (ϵ_r'') is called the loss factor and is a measure of how dissipative or lossy a material is to an external electric field. The imaginary part of permittivity (ϵ_r'') is always greater than zero and is usually much smaller than (ϵ_r').

$$\kappa = \frac{\epsilon}{\epsilon_0} = \epsilon_r = \epsilon_r' - j\epsilon_r'' \quad (2.11)$$

The imaginary part of permittivity, ϵ_r'' can actually be expressed as a function of both dielectric relaxation (ϵ_{rd}'') and conductivity (σ).

$$\epsilon_r'' = \epsilon_{rd}'' + \frac{\sigma}{\omega \epsilon_0} \quad (2.12)$$

In many cases, the value of σ is very low, but when an electromagnetic field is applied, the material consumes a considerable energy and exhibits some high values of σ in particular frequency ranges. ϵ_{rd} represents relaxation, and it is the dissipation energy during polarization and depolarization. In microwave domain, σ is dominant, hence the effect of ϵ_{rd} is negligible (66). Thus, conductivity of a dielectric material can be expressed as;

$$\sigma = \omega \epsilon_0 \epsilon_r'' \quad (2.13)$$

When complex permittivity is drawn as a simple vector diagram, the real and imaginary components are 90° out of phase. The vector sum forms an angle δ with the real axis (ϵ_r'). The loss tangent or $\tan \delta$ is defined as the ratio of the imaginary part of the dielectric constant to the real part, given in Equation 2.14.

$$\tan \delta = \frac{\epsilon_r''}{\epsilon_r'} \quad (2.14)$$

It is a measure of relative lossiness of a material or the ratio of the energy lost to the energy stored.

2.5.1 Dielectric response with the applied frequency

When a dielectric is placed in a time-varying electromagnetic field, its response to the time varying electric field depends on the polarity of the molecules. In his explanation, S. Palit (2005) outlined the difference in the behavior of polar and non-polar dielectric in time variable electric field. If it is a non-polar dielectric, dipole moments are induced in the molecules which also changes with time as the external electric field changes with time. Therefore, as the frequency of the field is increased, the dipole moments change gradually with the field, for frequency from zero up to that of visible light ($\sim 10^{14}$ Hz). As a result, dielectric constant remains stable for this range of frequency. On the other hand, polar molecule has a permanent dipole moment. When an external field is applied, it will exert a torque on the dipole which makes alignment to the direction of applied field. As the frequency of the field increases, the dipole alignment tends to lag behind the field reversal since the inertial moment of the molecules is quite large. Water, as an example of polar molecule requires 10^{-11} s to respond to the change in the field. Thus, this explains how the dielectric constant of water remains around 80 for frequency up to 10^{10} Hz and falls rapidly to a value of a non-polar liquid around 10^{11} Hz, somewhat similar to the pattern shown in Figure 2.12 [67].

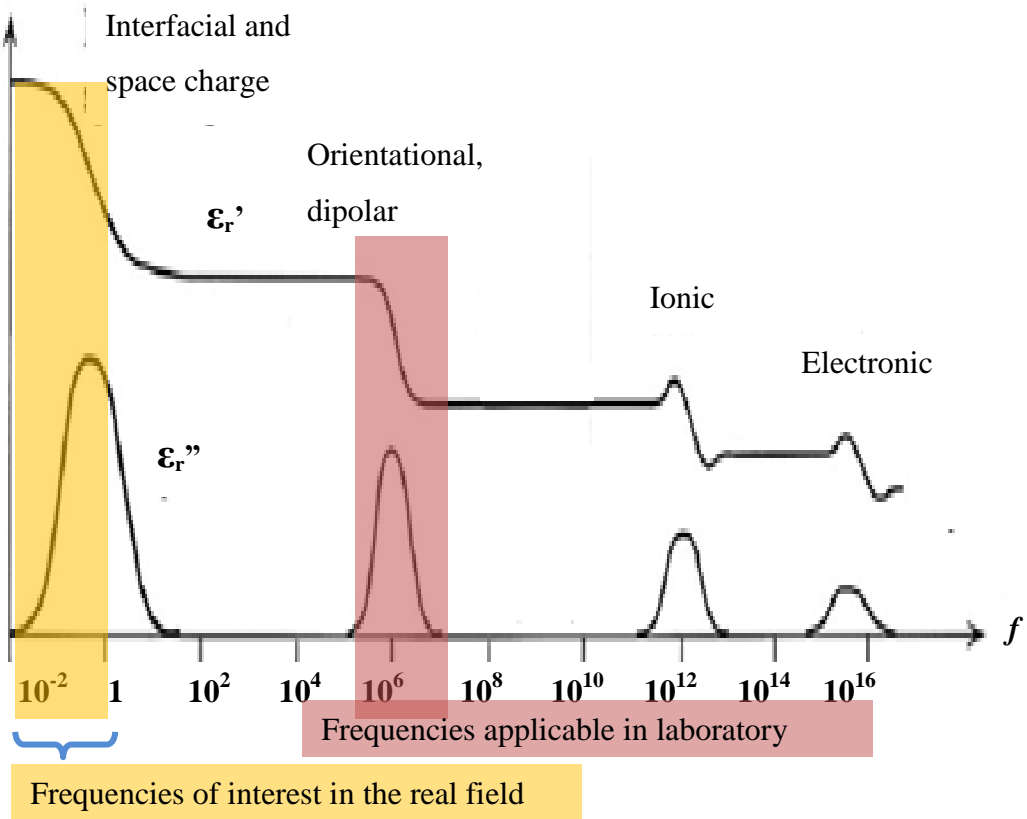


Figure 2.12: Dielectric response of solids over a wide range of frequencies [68]

2.6 Electromagnetic wave propagation theory

Similar to the constitutive relations in continuous medium mechanics, there are also constitutive relationships in electromagnetic. Constitutive relations describe the medium's properties and effects when two physical quantities are related. It can be viewed as the response of the medium as a system to certain input. In electromagnetic, there are four fundamental constitutive relationships to describe the response of a medium to a variety of electromagnetic input. Two of them describe the relationship between the electric field \mathbf{E} and the conductive current \mathbf{J} , and the electric displacement \mathbf{D} , and the other two describe the relationship between the magnetic field \mathbf{H} and the magnetic induction \mathbf{B} , and the magnetic polarization \mathbf{M} . In summary, governing equations of electromagnetic field, known as Maxwell's equations can be expressed in the following form:

$$\nabla \times \mathbf{H} = \mathbf{J} + \frac{\partial \mathbf{D}}{\partial t} \quad (2.15)$$

$$\nabla \times \mathbf{E} = -\frac{\partial \mathbf{B}}{\partial t} \quad (2.16)$$

$$\nabla \cdot \mathbf{B} = 0 \quad (2.17)$$

$$\nabla \cdot \mathbf{D} = \rho_e \quad (2.18)$$

Equation 2.15 was derived from the Ampere's law; it denotes that the electrical current (both the conductive current \mathbf{J} and the displacement current $d\mathbf{D}/dt$) induces the magnetic field. Equation 2.16 was derived from the Faraday's law; it describes the variation of the magnetic field induces the electrical field. Equation 2.17 and 2.18 are derived from the Gaussian Theorem, one for the magnetic field, and the other for the electrical field.

It is noticeable that in Equation 2.15 and 2.16, the electric field and the magnetic field are coupled with each other. They clearly state the coupling nature of the electromagnetic induction. Mathematically, it is relatively too complicated to solve and makes the physical nature more implicit. De-coupling these two equations allows more explicit explanation on their diffusion and wave propagation nature by some mathematical manipulations. Using the same argument and similar approach, similar results will be obtained for the second equation of the Maxwell equations (the Faraday's law) and give rise to Equation 2.19 and 2.20,

$$\nabla^2 \mathbf{H} = \sigma \mu \frac{\partial \mathbf{H}}{\partial t} + \epsilon \mu \frac{\partial^2 \mathbf{H}}{\partial t^2} \quad (2.19)$$

$$\nabla^2 \mathbf{E} = \sigma \mu \frac{\partial \mathbf{E}}{\partial t} + \epsilon \mu \frac{\partial^2 \mathbf{E}}{\partial t^2} \quad (2.20)$$

Obviously the two equations have been decoupled, i.e., only one physical quantity (field), either the electric field or the magnetic field, appears in one equation. After decoupling the electric field and the magnetic field we can further the discussion by look into the relativity of the material parameters for the electric and electromagnetic

properties. Without losing generality, an assumption can be made that the time variation of the electric field is in a simple harmonic form shown in Equation 2.21,

$$\mathbf{E} = \mathbf{E}_0 e^{-i\omega t}, \quad \frac{\partial \mathbf{E}}{\partial t} = -i\omega \mathbf{E}_0 e^{-i\omega t} = -i\omega \mathbf{E}, \quad \frac{\partial^2 \mathbf{E}}{\partial t^2} = (-i\omega)(-i\omega) \mathbf{E}_0 e^{-i\omega t} = -\omega^2 \mathbf{E} \quad (2.21)$$

Note that \mathbf{E} is a newly defined quantity without time varying component and omitted the subscript zero for the easy writing. Put this definition into Equation 2.22,

$$\begin{aligned} \nabla^2 \mathbf{E} &= \sigma\mu \frac{\partial \mathbf{E}}{\partial t} + \epsilon\mu \frac{\partial^2 \mathbf{E}}{\partial t^2} \\ &= -i\omega\sigma\mu\mathbf{E} - \omega^2\epsilon\mu\mathbf{E} \\ &= -\omega^2\epsilon\mu(1 + \frac{\sigma}{\omega\epsilon}i)\mathbf{E} \\ &= -k^2\mathbf{E} \end{aligned} \quad (2.22)$$

Following a similar approach, same results for the magnetic field could be obtained and hence give rise to a set of two, known as Helmholtz equations (Equation 2.23 and 2.24),

$$\nabla^2 H + k^2 H = 0 \quad (2.23)$$

$$\nabla^2 E + k^2 E = 0 \quad (2.24)$$

where k is defined as the squared complex wave number (Equation 2.25);

$$k^2 = \omega^2 \mu\epsilon(1 + \frac{\sigma}{\omega\epsilon}i) \quad (2.25)$$

It is clear that in the above equation when the second term in the bracket on the right hand side has a value much larger than one ($\sigma \gg \omega\epsilon$), then the k^2 has a significant imaginary part so that the Helmholtz equation is essentially representing a diffusion equation. Vice versa, if the ratio is much less than one, the k^2 has a significant real part so that the Helmholtz equation is essentially representing a wave equation. That is to say, in Equation 2.26 and 2.27 if $\sigma \gg \omega\epsilon$;

$$\nabla^2 H \approx \sigma\mu \frac{\partial H}{\partial t} \quad (2.26)$$

$$\nabla^2 E \approx \sigma\mu \frac{\partial E}{\partial t} \quad (2.27)$$

Since most earth materials do not have strong magnetic susceptibility, the electric conductivity is the controlling parameter in the process. Thus the above equation represents a conductive, or diffusion process, similar to the diffusion equation used to describe heat conduction, groundwater flow etc. On the other hand, $\sigma \ll \omega\epsilon$ will yield Equation 2.28 and 2.29;

$$\nabla^2 H \approx \epsilon\mu \frac{\partial^2 H}{\partial t^2} \quad (2.28)$$

$$\nabla^2 E \approx \epsilon\mu \frac{\partial^2 E}{\partial t^2} \quad (2.29)$$

Magnetic permeability is relatively weak for most earth materials and hence, the dielectric permittivity is the dominant parameter in this equation. Dielectric polarization is the controlling process other than conduction. The physical feature is the wave propagation-like process, similar to the mechanical waves.

CHAPTER 3

METHODOLOGY

This chapter consists of four major sections; synthesis and characterization of dielectric nanoparticles; nanofluid preparation and characterization; petrophysical properties characterization and evaluation of recovery by core flooding test, as shown in Figure 3.1. Sol gel method was used to synthesize two different types of material, namely ZnO and Al₂O₃. Recovery efficiency from both nanofluid injections were compared in the core displacement tests.

The as-prepared nanoparticles were characterized using x-ray diffraction (XRD), field emission scanning electron microscopy (FESEM), energy dispersed x-ray (EDX) and transmission electron microscopy (TEM). Validation of oil recovery mechanism was conducted by measuring surface tension at oil and water interface and dielectric properties of nanofluid at various applied frequency.

Petrophysical characterization of the porous medium and the fluids were conducted by using Darcy's law. Permeability, porosity and pore volume of the porous medium were calculated to determine the oil and water saturation during the core flooding test.

Fluid properties of the crude oil and brine e.g. viscosity and density were measured for calculation of significant parameters found in the core flooding test. Recovery evaluation was done by comparing the ratio between the displaced oil after EOR stage to the residual oil in place (ROIP). Calculation of the recovery will be further derived in this chapter.

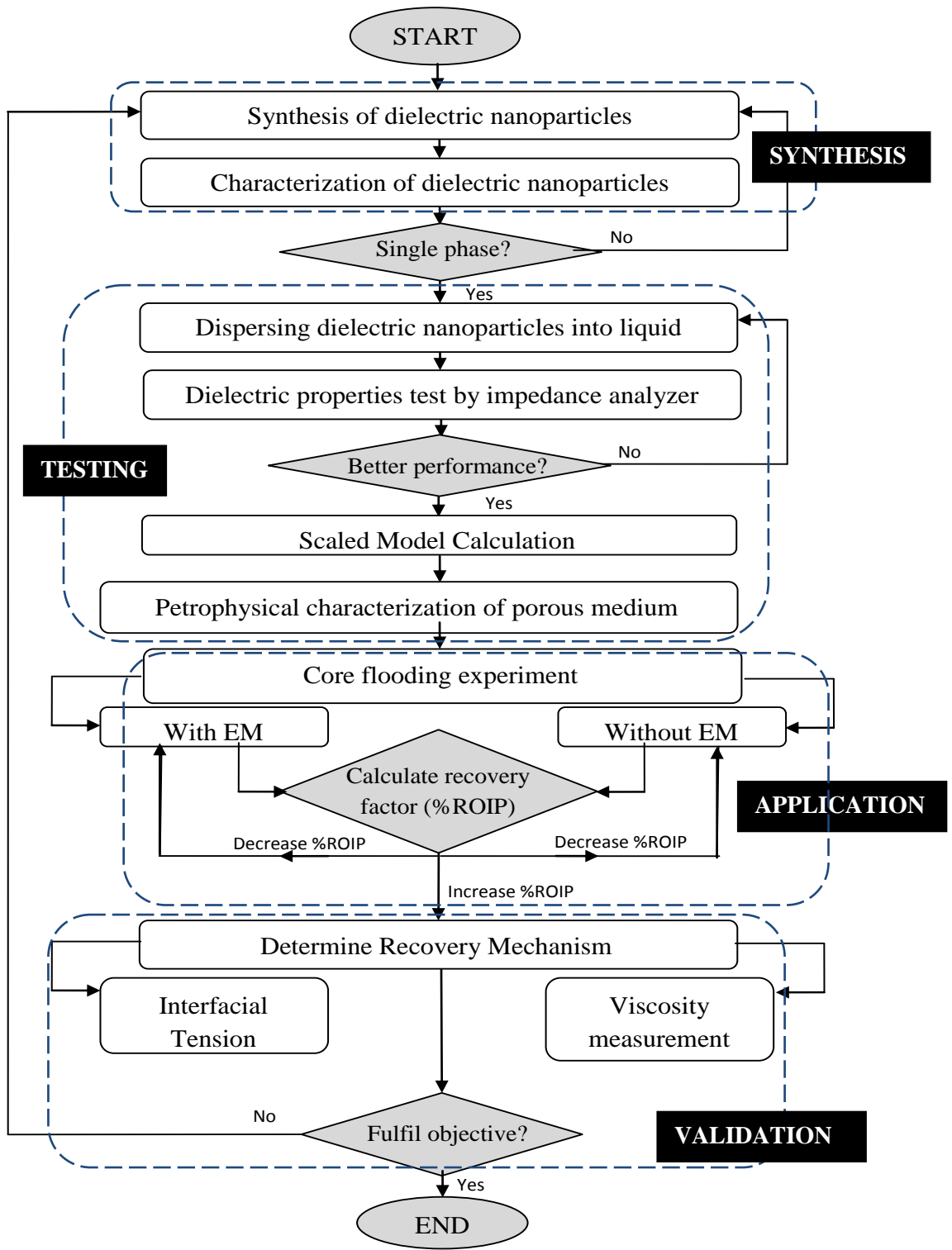


Figure 3.1: Flow chart of the methodology

3.1 Synthesis of Dielectric Nanoparticles

Two types of dielectric nanoparticles, ZnO and Al₂O₃ were prepared via sol-gel method. This method was chosen based on the high chemical homogeneity and purity of the final product, as well as flexibility to manipulate chemical composition, high repeatability and low production cost [69, 70].

To prepare ZnO nanoparticles, zinc nitrate hexahydrate was dissolved in doubly distilled water and was magnetically stirred to obtain homogeneous sol. Subsequently, nitric acid, HNO₃ was added to serve as a peptizing agent since stable colloid may form in low pH environment. At lower pH, the preferential absorption of H⁺ ion from HNO₃ onto the particle surface increases the surface charges and makes the particles repel each other and keeps a distance apart, i.e., creating electrostatic stabilization [71]. Among various peptizing agent, HNO₃ was chosen due to the ability of nitrate ions to reduce the temperature needed for phase transformation of crystals, i.e. from θ to α in Al₂O₃ as demonstrated by Thiruchitrambalam et al (2004) using sol gel method [69].

Gelation took place when the homogeneous sol was heated at temperature not exceeding 80°C, thus most of the –OH component would be removed at this stage. Gel formed was further heat treated in the drying oven at temperature 110°C to remove excess water. As-dried powder sample was crushed to ensure homogeneous dispersion of the powder particles before annealing. The fine powders were annealed in air at temperature range of 200°C to 500°C to obtain single phase hexagonal wurtzite crystals upon completion.

The synthesis process is summarized in Figure 3.2. In order to determine exactly how much metal nitrate precursor need to be reacted with the solvent to produce its oxides, stoichiometric calculation was done by considering the ratio of the weight of precursor without the presence of water to the weight of precursor in the presence of water. To dissolve 1 g of the precursor, 5 ml of the solvent has to be added into the mixture and magnetically stirred to obtain homogeneous solution. Homogeneity of the solution is proportional to the stirring duration. As the stirring duration increases, the

solution will become more homogeneous and thus yield better micro structural properties. Table 3.1 shows the stoichiometric calculation for 10g of ZnO nanoparticles.

Similar procedure was repeated for the synthesis of Al₂O₃ nanoparticles. Aluminum nitrate nonahydrate was used as the Al³⁺ metal ion precursor. As-dried powder formed was crushed and subsequently annealed at 900°C, 1000°C and 1100°C. Stoichiometric calculation to prepare 10 g of Al₂O₃ nanoparticles is shown in Table 3.2.

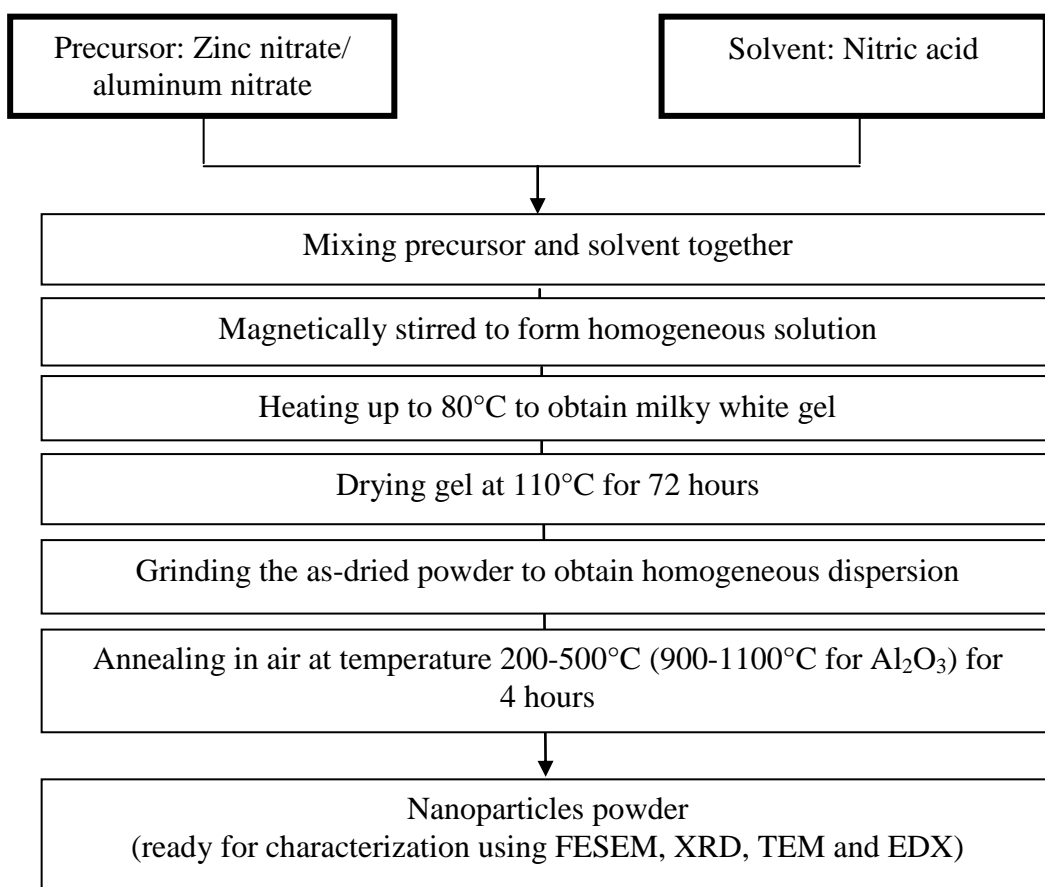


Figure 3.2: Synthesis of zinc oxide by sol gel method

Table 3.1: Stoichiometric calculation of ZnO

Precursor	With water	Molecular weight (with water presence), g/mol	Without water	Molecular weight (without water presence), g/mol	Prepare 10g of final product (without water), g	Prepare 10g of final product (with water), g
Zn(NO ₃) ₂ · 6H ₂ O	0.8 Zn 2 x N 12 x O 12 x H	65.409 28.0134 191.9928 12.09528	0.8 Zn 2 x N 6 x O	65.409 28.0134 95.9964	(189.4188/ 189.4188) x 10	(297.5105/ 189.4188) x 10
Total (g)		297.5105		189.4188	10.0000	15.7065

Table 3.2: Stoichiometric calculation of Al₂O₃

Precursor	With water	Molecular weight (with water presence), g/mol	Without water	Molecular weight (without water presence), g/mol	Prepare 10g of final product (without water), g	Prepare 10g of final product (with water), g
Al(NO ₃) ₃ · 6H ₂ O	0.8×Al 3 × N 18 × O 18 × H	26.9815 42.0202 287.9892 18.12492	0.8 Al 3 x N 9 x O	26.9815 42.02022 143.9946	(189.4188/ 189.4188) x 10	(375.11584/ 212.996) x 10
Total (g)		375.11584		212.996	10.0000	17.6114

3.2 Characterization of nanoparticles

Determination of the micro structural properties of the nanoparticles e.g. surface morphology, crystallography and elemental analysis were conducted by using analytical equipments available in UTP.

3.2.1 Field Emission Scanning Electron Microscopy (FESEM)

Supra 55VP Zeiss Variable Pressure Field Emission Scanning Electron Microscope (VP-FESEM) is a type of microscope that works with electrons (particles with a negative charge) instead of light, as shown in Figure 3.3. It operates based on the low energy secondary electrons generated at the impact point of the primary

electron beam that are intercepted by the weak electrical field at the sample surface. They are then accelerated to a high energy by the field of the electrostatic lens and focused on the annular *In-lens* detector inside the beam booster located above the objective lens.

Electron microscope has the ability to resolve objects ranging from part of nanometer to micrometer compared to light microscope that has a magnification in the range of 1000 and resolution of 200 nm. When the electron beam interacts with the specimen, it could expose useful information about the sample including its surface morphology and texture, size and shape of the features, composition and crystalline structure.



Figure 3.3: Supra 55VP Zeiss Variable Pressure Field Emission Scanning Electron Microscope (VP-FESEM)

3.2.2 Energy Dispersive X-Ray (EDX)

Energy Dispersed X-Ray Spectroscopy (EDX) is linked to the FESEM. It identifies type of elements present within the sample and quantifies its composition. Identification of elements present in a sample relies on the fundamental principle that each element has a unique atomic structure, which exhibit unique set of peaks on the x-ray spectrum. An incident x-ray beam will be focused onto the specimen being

tested, and therefore excite a ground state electron in an inner shell of the atom, leaving an empty space which is known as hole, as presented in Figure 3.4. To conserve the energy, an electron in outer, higher energy shell will fill in the hole and radiate the excess energy in the form of x-ray as it relocates itself in the lower energy shell. The elemental composition of the specimen to be measured is determined by observing the energy difference between these two shells, which is a characteristic of the atomic structure of the element from which they were emitted.

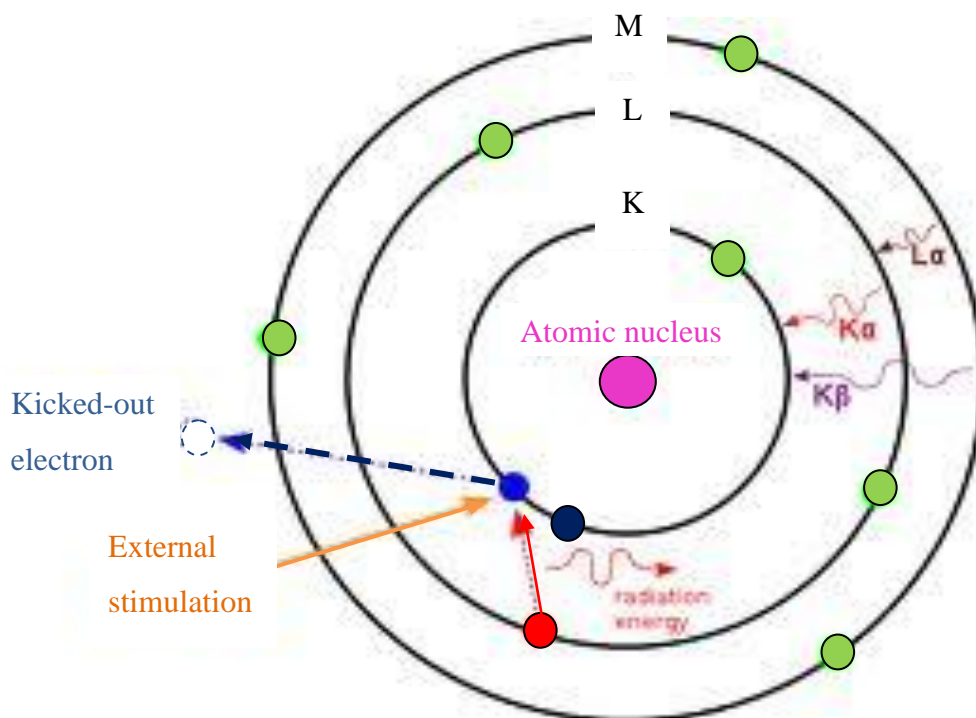


Figure 3.4: Fundamental principle of elemental detection

3.2.3 X-ray powder diffraction (XRD)

X-ray powder diffraction (XRD) is a characterization tool used for identifying the types of phases present in the specimen. The underlying principle of this tool is based on Bragg's Law ($2d \sin \theta = n\lambda$) which describes the relation between the angle (θ) and wavelength (λ) of focused x-ray with the distance between atoms, d-spacing (d) in the crystal. When a monochromatic beam of x-rays having wavelength of the same order of magnitude as the atomic spacing in the material incident on the material, x-rays are scattered in all directions which may undergo destructive interference as a

result of cancellation. However, if certain crystallographic planes been stroke at specific angles, the diffracted x-rays are reinforced rather than annihilated, as shown in Figure 3.4 [72].

The average particle size, d_{hkl} can be measured using Scherer's equation as described by Equation 3.1,

$$d_{hkl} = \frac{k\lambda}{\beta_{hkl} \cos \theta} \quad (3.1)$$

where k is the shape factor with typical value of 0.9, λ is the x-ray wavelength (\AA), β is the line broadening at half the maximum intensity (FWHM) in radians, and θ is the Bragg angle.

XRD measurements were conducted using a Bruker A&S D8 Advanced Diffractometer instrument equipped with a CuK α radiation source ($\lambda = 1.5406\text{\AA}$), at 40 kV and 30 mA. The scanning angle (2θ) used was in the range of range of 2–80° at scanning speed and step size of 1.00°/min and 0.05°, respectively. By using EVA software, the resultant spectra were compared with the standard reference to confirm the phase of tested specimen. Information such as Bragg angle (2θ), full width half maximum (FWHM), d-spacing and lattice parameter were also determined using this software.

3.2.4 Transmission Electron Microscope (TEM)

TEM offers information on micro texture and nanostructure of electron-transparent specimens. The electron beam passes through the solenoids, down the column, makes contact with the screen where the electrons are converted to light and form an image. During transmission, the speed of electrons directly correlates to electron wavelength; the faster electrons move, the shorter wavelength and the greater the quality and detail of the image. When greater numbers of electrons were able to pass through the specimen, the image form at that particular area will appear lighter, whereby darker areas reflect the dense areas of the specimen. Differences in the

brightness provide information on the structure, texture, shape and size of the specimen.

To obtain a TEM analysis, samples need to be sliced thin enough for electrons to pass through, a property known as electron transparency. Few milligrams of nanoparticles were dispersed in 2-propanol and sonicated for about 1 hour. The mixture was then allowed to settle for about 1 hour at room temperature. Two layers consisting of sediment and clear solution were formed. Only few drops of clear solution needed to be dropped on a carbon-coated copper grid. This copper grid was then transferred to a chamber of the TEM. As shown in Figure 3.5, TEM used in this research was model Zeiss Libra 200FE for analysis at 200 kV and magnification from 8X to 1,000,000X.

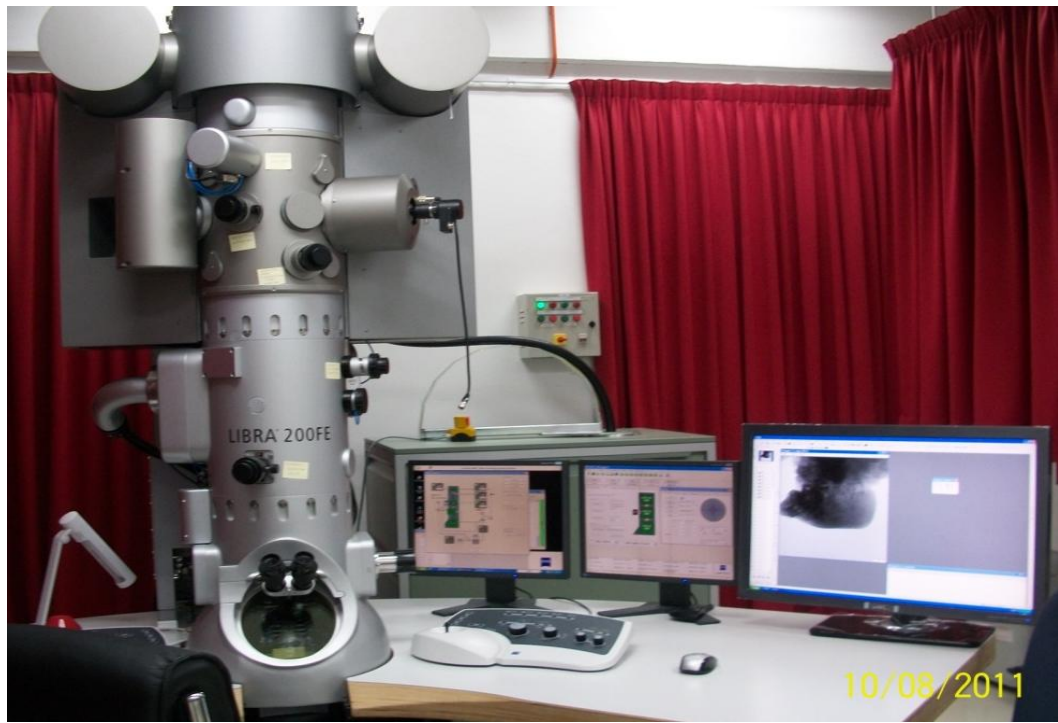


Figure 3.5: Libra 200FE Zeiss Transmission Electron Microscope

3.3 Nanofluid Preparation and Characterization

Nanoparticles powder has to be dispersed in liquid medium to enable injection into reservoir. Its preparation steps and characterization e.g. dielectric properties, oil-

aqueous phase interfacial tension and viscosity will be described in the following subsection.

3.3.1 Preparation of Nanofluids

Since ZnO and Al₂O₃ nanoparticles were prepared in powder form, they have to be stably suspended in suitable liquid to enable injection into porous medium for enhanced oil recovery purpose. The nanoparticles suspension or termed as nanofluids from this point onwards, were prepared using two steps method. In the first step, both nanoparticles were dispersed in deionized water as the base fluid and magnetically stirred for 1 hour. An anionic surfactant, SDS of 90.0% purity was added into the suspension to improve the stability of the suspended nanoparticles. Second step involved agitation of the suspension in an ultrasonic bath at temperature 25°C for 1 hour to ensure homogeneous dispersion of nanoparticles in the base fluid.

3.3.2 Dielectric properties measurement

Dielectric properties of the nanofluids were determined by using Agilent 4294A Impedance Analyzer, attached with the 16451B Liquid Dielectric Fixture as depicted in Figure 3.6. Parallel capacitance and resistance of the fluids were measured to determine the properties e.g. dielectric permittivity, loss factor and loss tangent, which were calculated using Equation 3.2, 3.3 and 3.4;

$$k' = \frac{C_p}{C_o} \quad (3.2)$$

$$k'' = \frac{1}{\omega C_0 R_p} \quad (3.3)$$

$$\tan \delta = \frac{k''}{k'} \quad (3.4)$$

where, C_p is the capacitance of air, measured in Farad, C_0 is the capacitance of the material under test, measured in Farad, k' is the relative permittivity, k'' is the relative

loss factor, $\tan \delta$ is the loss tangent and R_p is the parallel resistance of the material under test, measured in ohm.

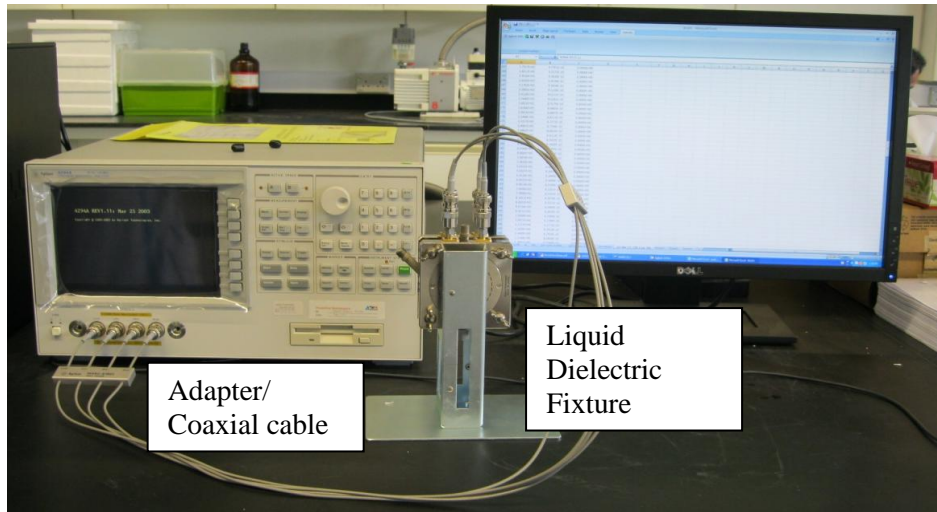


Figure 3.6: Agilent 4294A Impedance Analyzer with 16451B Liquid Dielectric Fixture

3.3.3 Oil-aqueous phase interfacial tension (IFT) measurement

Interfacial tension between oil and injection fluids e.g. ZnO and Al₂O₃ nanofluids, aqueous SDS and brine were measured by using Data Physics SVT20N Spinning Drop Video Tensiometer, equipped with SVTS 20 software package, as shown in Figure 3.7 and 3.8, respectively.

The measurements were conducted by controlling the tilt angle and rotation of the oil drop present in the capillary block, known as drop phase into the excess injection fluids, known as outer phase at 10,000 rpm. If the IFT is not low enough and the length of the oil drop captured by the charged-coupled device (CCD) camera is smaller than 4 times its diameter; IFT, γ measured in mN/m is calculated based on spinning drop contours according to Laplace-Young method shown in Equation 3.5,

$$\gamma = 2.74156e^{-3} \frac{(\rho_h - \rho_d)\omega^2}{C} \quad (3.5)$$

where ρ_h is the density of the heavy (outer) phase (g/cm^3), ρ_d is the density of the light (drop) phase (g/cm^3), ω is the rotational velocity (rpm), D is the measured drop width (mm) and C is a coefficient determined by the ratio of the length to the width of the oil drop.

In this measurement series, oil-brine IFT was measured as the reference value for the next reduction in IFT by using other fluids. IFT of oil-SDS aqueous solution was measured since it serves as the base fluid for the nanoparticles suspension, therefore knowing the IFT value of oil-SDS alone is crucial to determine the effect of nanoparticles addition on the recovery efficiency.

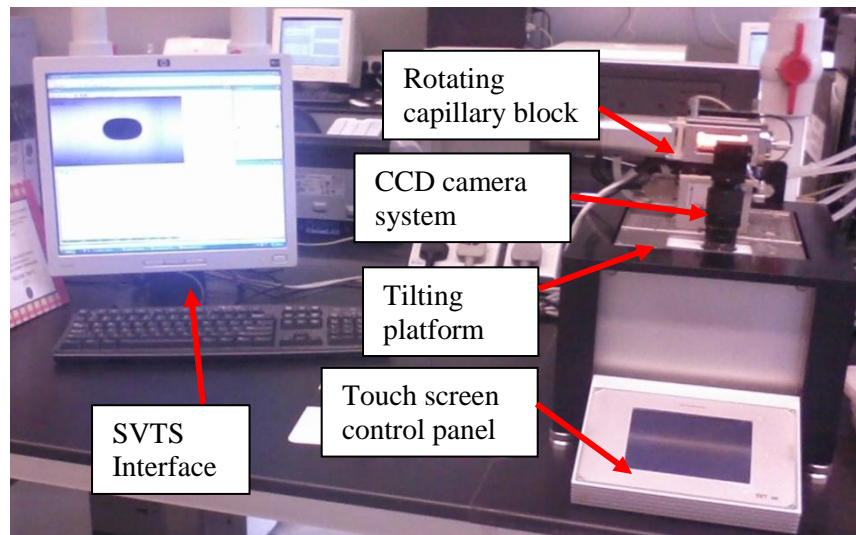


Figure 3.7: SVT 20N DataPhysics Spinning Drop Tensiometer

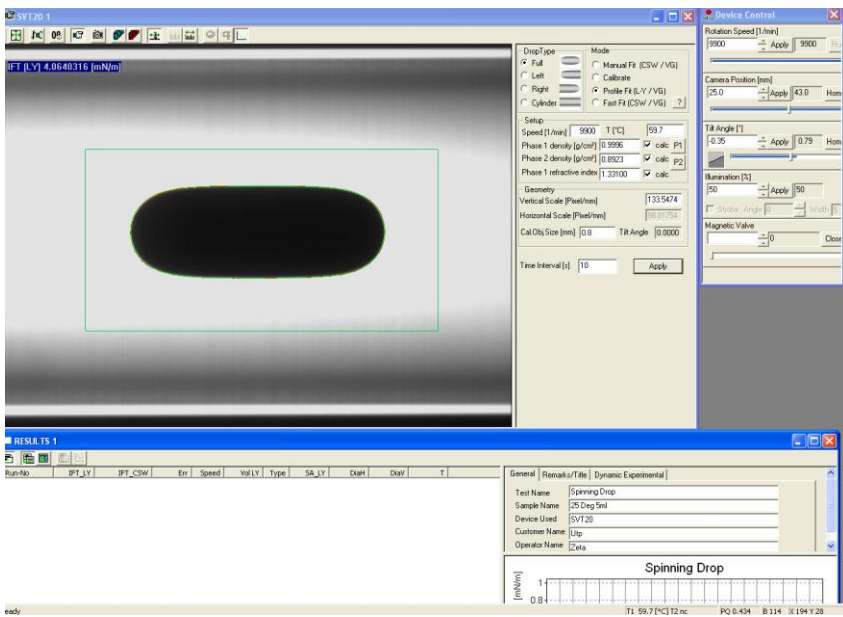


Figure 3.8: The interface of SVTS 20 software for IFT calculation

3.3.4 Viscosity Measurement

Viscosity of the fluids was measured by using Brookfield CAP 2000+Viscometer, as shown in Figure 3.9. Spindle 01 was used throughout the measurement of all samples, in maximum rotation of 100 rpm at ambient temperature, 25°C.



Figure 3.9:
Brookfield
CAP 2000+
Viscometer

3.4 Electromagnetic Wave Transmission System

To stimulate the dielectric properties of the nanomaterials, low frequency EM wave has to be transmitted into the oil reservoir through sediment layers of various permittivity and conductivity value. In order to ensure that the transmitted EM wave will reach to the targeted location either in real field or laboratory, a scaled model calculation was done prior to the core flooding experiment with the irradiation of EM wave. By having suitable frequency and skin depth applicable in the laboratory scale, the dimension of the scaled model can be determined.

3.4.1 Scaled Model Calculation

Calculation of the scaled model was made to choose scale factor and frequency to be used in the experiment. Based on the transmitter-reservoir position as shown in the schematic diagram in Figure 3.10, the dimension e.g. depth and position of the transmitter and reservoir in the scaled laboratory experimental setup can be determined and can be directly correlated to the dimension in the field scale.

The proposed idea is to apply a non-invasive method i.e. transmitting EM wave from the seafloor into oil reservoir through sediment layers by using a transmitter which is located on the seafloor as a means to stimulate dielectric nanoparticles injected into the reservoir beforehand. In some cases, oil reservoirs are buried at depth more than 1,800 meter (5,000 feet) give limitations to the selection of EOR method due to the large distance between seafloor and the oil reservoir, which may cause the reservoir to have high temperature and high pressure. Therefore, the parameters to be used in designing a scaled laboratory experimental setup i.e. scale factor, n , wavelength, λ and penetration depth, δ was calculated by using Equation 3.6, 3.7 and 3.8;

$$n^2 f_{fs} = f_{lab} \quad (3.6)$$

$$\lambda = \sqrt{\frac{8\pi^2}{\mu\sigma\omega}} \quad (3.7)$$

$$\delta = \sqrt{\frac{2}{\mu\sigma\omega}} \quad (3.8)$$

where f_{lab} is the frequency used in the laboratory experiment, f_{fs} is the frequency to be used in the real field, μ is the permeability in free space, σ is the conductivity of the medium and ω is the angular frequency applied. Wavelength calculated using the equation above denotes the wavelength of the transmitted EM wave at particular frequency, whereas the penetration depth will give information on how far the distance travelled by the transmitted wave before its amplitude decays by a factor of $1/e$. All parameters calculated using Equation 3.8, 3.9 and 3.10 are presented in Table 3.3.

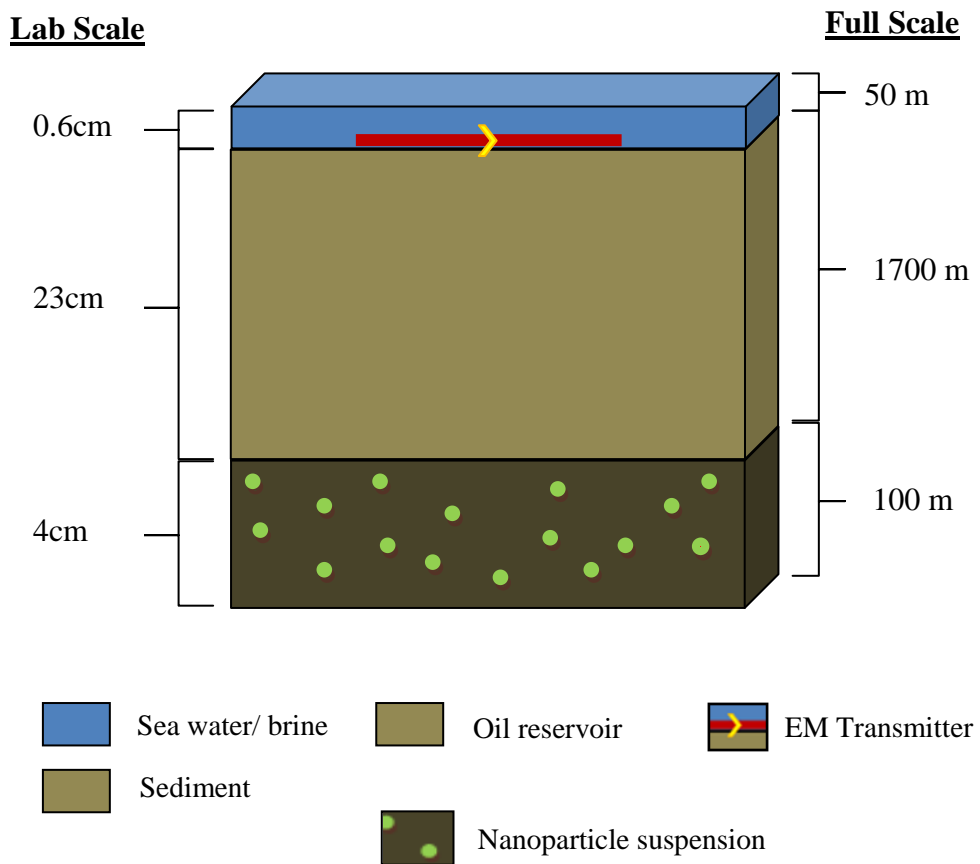


Figure 3.10: Schematic diagram of the transmitter-oil reservoir system

Table 3.3: Parameters calculated for designing the scaled experimental setup

d_{fs} (m)	d_{lab} (m)	f_{fs} (Hz)	f_{lab} (MHz)	λ_{fs} (m)	λ_{lab} (m)	L_{trans} (cm)	δ_{fs} (m)	δ_{lab} (m)
1781	0.23	100	5996.15	1414.21	0.183	9.1	225.050	2.9
1781	0.23	50	2998.07	2000.00	0.258	12.9	318.269	4.1
1781	0.23	25	1499.04	2828.43	0.365	18.3	450.100	5.8
1781	0.23	5	299.81	6324.56	0.817	40.8	1006.454	13.0
1781	0.23	1	59.96	14142.14	1.826	91.3	2250.499	29.1
1781	0.23	0.75	44.97	16329.93	2.109	105.4	2598.652	33.6

3.4.2 Core Flooding Experimental Setup

The core flooding experimental setup can be classified into three major sections; the injection section, the displacement section and the collection section. Injection section consists of displacement pump, control valve, pressure gauge and injection fluids e.g. brine, oil and nanofluids. All components are connected together by suitable nylon tubing and compatible connectors. Porous medium comprises of silica beads packed in a sealed acrylic column serves as the main component in the displacement section, while measuring cylinders and control valve belong to the collection section. A heater with thermocouple were used to keep the bath temperature remain constant at 60°C. If core flooding test is to be conducted in the presence of electromagnetic waves, an aluminum rod connected to an 80 MHz wave function generator will be fixed on top of the displacement column, at the height specified from the scaled model calculation. As presented in Figure 3.11, all core flooding tests were conducted at ambient pressure in the water bath; which serves to maintain constant temperature throughout the core flooding procedure, as well as to create EM wave propagation medium of similar permittivity and conductivity with the full scale environment.

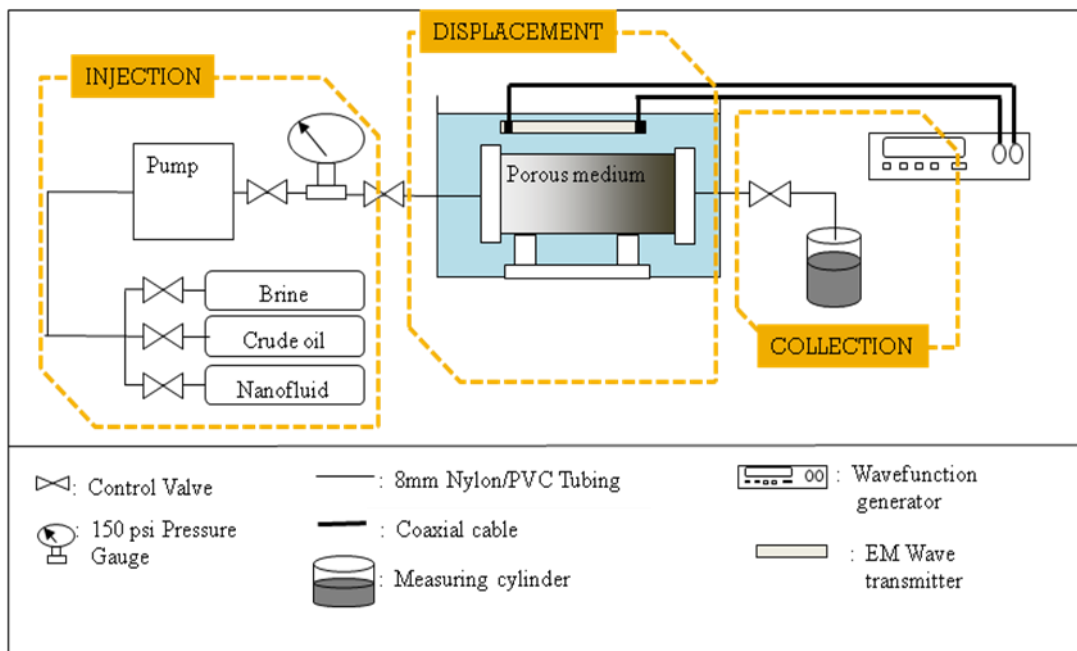


Figure 3.11: Schematic diagram of core flooding setup

3.5 Petrophysical Characterization

Petrophysical characterization comprises of measurement of the properties of the reservoir rocks and fluids used in the experiment. It can be divided into 2 parts; porous material e.g. silica beads pack and fluids e.g. crude oil and brine.

3.5.1 Fluids characterization

Arabian Heavy crude oil was used throughout this research. Details of the oil can be found in Table 3.4. Fluid properties e.g. viscosity and density were measured to understand their behavior with temperature, especially at reservoir temperature.

Table 3.4: Details of the crude oil for viscosity measurement

Type of Crude	Arabian Heavy
Origin	Saudi Arabia
API Gravity	28.1
Density @ 25°C	0.886
Equipment used	Tamson Viscometer Unit TVB445
Tube size	1B
Tube calibration constant	0.05

Kinematic viscosity is measured by noting the time it takes for the oil to travel through the orifice of a capillary under the force of gravity. The orifice of the kinematic viscometer tube produces a fixed resistance to flow. Different sized capillaries are available to support fluids of varying viscosity, thus in this test size IB was used. The time taken for the fluid to flow through the capillary tube can be converted directly to a kinematic viscosity using a simple calibration constant provided for each tube, which is 0.05 for tube 1B, as shown in Figure 3.12.

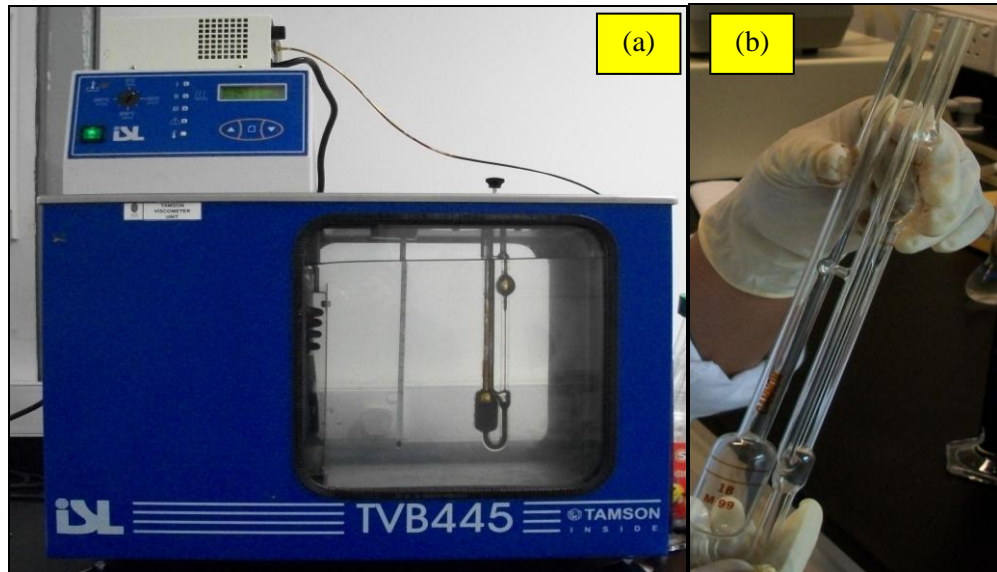


Figure 3.12: Kinematic viscosity measurement device (a) Tamson Viscometer Unit TVB445 and (b) Capillary tube 1B

3.5.2 Reservoir rocks characterization

The material of which a petroleum reservoir rock may be composed can range from very loose and unconsolidated sand to a very hard and dense sandstone, limestone, or dolomite. The grains may be bonded together with a number of materials, the most common of which are silica, calcite, or clay. Knowledge of the physical properties of the rock and the existing interaction between the hydrocarbon system and the formation is essential in understanding and evaluating the performance of a given reservoir [73].

Rock properties are determined by performing laboratory analyses on cores from the reservoir to be evaluated. The cores are removed from the reservoir environment, with subsequent changes in the core bulk volume, pore volume, reservoir fluid saturations, and, sometimes, formation wettability. The effect of these changes on rock properties may range from negligible to substantial, depending on characteristics of the formation and property of interest, and should be evaluated in the testing program. There are basically two main categories of core analysis tests that are performed on core samples regarding physical properties of reservoir rocks e.g. porosity, permeability and saturation. These rock properties are essential for reservoir engineering calculations as they directly affect both the quantity and the distribution of hydrocarbons and, when combined with fluid properties, control the flow of the existing phases (i.e. gas, oil, and water) within the reservoir.

3.5.2.1 Permeability

Permeability is a property of the porous medium that measures the capacity and ability of the formation to transmit fluids. The rock permeability, k , is a very important rock property because it controls the directional movement and the flow rate of the reservoir fluids in the formation. This rock characterization was first defined mathematically by Henry Darcy in 1856. In fact, the equation that defines permeability in terms of measurable quantities is called Darcy's Law [73]. Darcy developed a fluid flow equation that has since become one of the standard mathematical tools for petroleum engineer. If a horizontal linear flow of an

incompressible fluid similar to a system shown in Figure 3.13 is established through a core sample of length L and a cross-section of area A , then the governing fluid flow is defined in Equation 3.9,

$$q = -\frac{kA}{\mu} \frac{dP}{dL} \quad (3.9)$$

where q is the flow rate through the porous medium, cm^3/s ; A is the cross-sectional area across which flow occurs, cm^2 ; k is the proportionality constant, or permeability, Darcy; μ is the viscosity of the flowing fluid, cp ; dp/dL is the pressure drop per unit length, atm/cm . The physical interpretation of the negative sign in Darcy law (Equation 3.9) can be defined as the directional pressure increases in one direction while the length increases in the opposite direction.

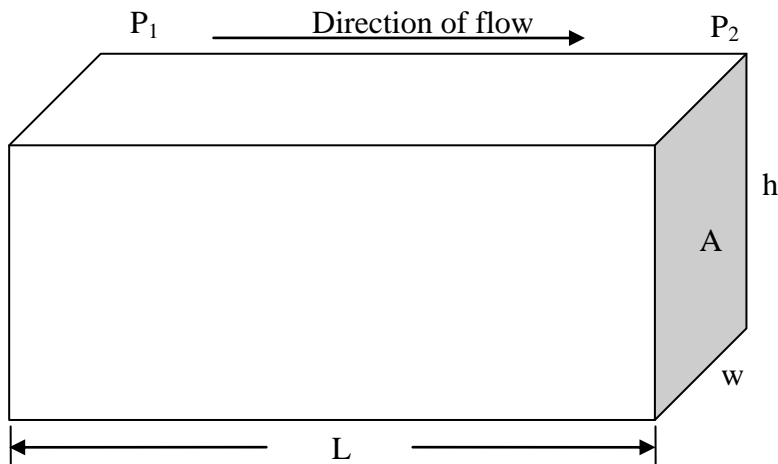


Figure 3.13: Linear flow model

Since p_1 is always greater than p_2 , the pressure terms can be rearranged, which will eliminate the negative term in the equation. The resulting equation is shown in Equation 3.10:

$$q = \frac{kA(p_1 - p_2)}{\mu L} \quad (3.10)$$

In this research, unconsolidated cores made of packed silica beads were used as a porous medium, to replicate the reservoir material. A 15 cm acrylic tube, with radius 1.688 cm was used as a column to contain glass beads mixtures of various sizes; average mesh size of 30-60 μm , 90-150 μm and 425-600 μm , as shown in Figure 3.14. Permeability, porosity and pore volume of six different bead size combinations were analyzed to find suitable mixture for measurement purpose. The details were tabulated in Table 3.5.

Glass beads were filled in a PVC tube, sealed at both ends and packed by using Sieve Shaker, to ensure maximum packing by forcing the grains to occupy the voids. The column were then weighed to obtain its dry weight and connected to a dosing pump to enable injection of fluid e.g. brine into the column for permeability measurement using Darcy's Law. The set up of the experiment is shown in Figure 3.14.

Table 3.5: Glass beads mixtures of different combination, mixed at equal ratio

Average mesh size (μm)	30-60 (A)	90-150 (B)	425-600 (C)
30-60 (A)	AA	AB	AC
90-150 (B)		BB	BC
425-600 (C)			CC

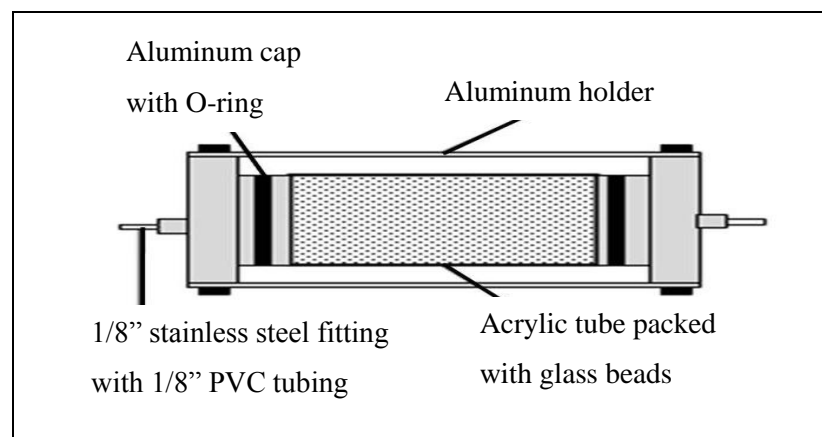
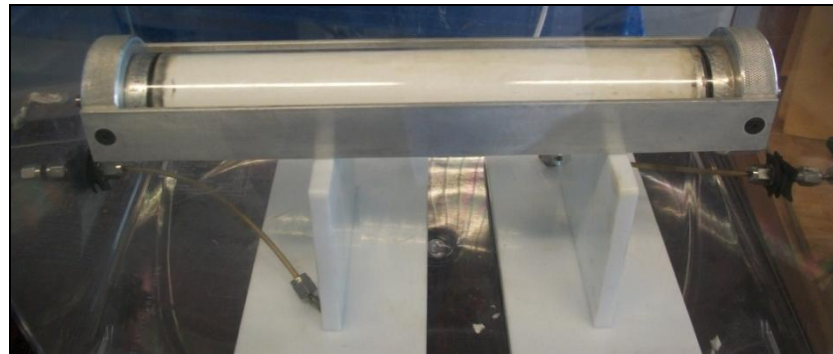


Figure 3.14: Measurement column serves as unconsolidated cores for petro physical characterization and core flooding experiment

3.5.2.2 Porosity

The porosity of a rock is a measure of the storage capacity (pore volume) that is capable of holding fluids. Quantitatively, the porosity is the ratio of the pore volume to the total volume (bulk volume). If the porosity of a rock sample was determined by saturating the rock sample 100 percent with a fluid of known density and then determining, by weighing, the increased weight due to the saturating fluid, this would yield an effective porosity measurement because the saturating fluid could enter only the interconnected pore spaces. This important rock property is determined mathematically by a generalized relationship shown in Equation 3.11:

$$\varphi = \frac{\text{Interconnected Pore Volume}}{\text{Bulk Volume}} \quad (3.11)$$

where φ is the effective porosity usually expressed in term of ratio or percentage. The effective porosity is the value that is used in all reservoir engineering calculations because it represents the interconnected pore space that contains the recoverable hydrocarbon fluids. As the sediments were deposited and the rocks were being formed during past geological times, some void spaces that developed became isolated from the other void spaces by excessive cementation. Thus, many of the void spaces are interconnected while some of the pore spaces are completely isolated.

3.5.2.3 Fluid Saturation

Saturation is defined as that fraction, or percent, of the pore volume occupied by a particular fluid (oil, gas or water). This property is expressed mathematically by Equation 3.12;

$$\text{Fluid Saturation} = \frac{\text{Total volume of the fluid}}{\text{Pore volume}} \quad (3.12)$$

Applying the above mathematical concept of saturation to each reservoir consists of oil and water only gives,

$$S_o = \frac{\text{Volume of oil}}{\text{Pore Volume}} \quad (3.13)$$

$$S_w = \frac{\text{Volume of water}}{\text{Pore Volume}} \quad (3.14)$$

where S_o and S_w are the saturation value of the oil and water, respectively. The saturation of each individual phase ranges between zeros to 100 percent. By definition, the sum of the saturations is 100%, therefore,

$$S_o + S_w = 1.0 \quad (3.15)$$

The fluids in most reservoirs are believed to have reached a state of equilibrium and, therefore, will have become separated according to their density, i.e., oil overlain by gas and underlain by water. In addition to the bottom (or edge) water, there will be connate water distributed throughout the oil and gas zones. The water in these zones will have been reduced to some irreducible minimum. The forces retaining the water in the oil and gas zones are referred to as capillary forces because they are important only in pore spaces of capillary size. Connate (interstitial) water saturation S_{wc} is important primarily because it reduces the amount of space available between oil and gas. It is generally not uniformly distributed throughout the reservoir but varies with permeability and lithology. Another particular phase saturation of interest is called the critical saturation and it is associated with each reservoir fluid. The definition and the significance of the critical saturation for each phase are described below.

a) Critical oil saturation, S_{oc}

For the oil phase to flow, the saturation of the oil must exceed a certain value which is termed critical oil saturation. At this particular saturation, the oil remains in the pores and, for all practical purposes, will not flow.

b) Residual oil saturation, S_{or}

During the displacement of the crude oil system from the porous media by water, there will be some remaining oil left that is quantitatively characterized by saturation value that is larger than the critical oil saturation. This saturation value is a called the residual oil saturation, S_{or} . The term residual saturation is usually associated with the non-wetting phase when it is being displaced by a wetting phase.

c) Critical water saturation, S_{wc}

The critical water saturation, connate water saturation, and irreducible water saturation are extensively used interchangeably to define the maximum water saturation at which the water phase will remain immobile.

3.6 Core Flooding Tests

In the core flooding test, there are four major stages carried out for each EOR fluids; SDS (as controlled set of experiment), Al_2O_3 nanofluid and ZnO nanofluid, as shown in Figure 3.15. There are two strategies applied in the tests to identify the role of few parameters in improving oil production, which are:

1. Injection of SDS solution, ZnO nanofluid and Al_2O_3 nanofluid in the absence of electromagnetic waves to observe the role of nanoparticles alone in recovering more oil
2. Injection of ZnO nanofluid and Al_2O_3 nanofluid in the presence of electromagnetic waves to investigate the role of electromagnetic waves in activating the dielectric properties of both nanoparticles.

The core displacement tests were performed at temperature 60°C in ambient pressure, following the procedure as shown in Figure 3.15. To prepare the reservoir material, the glass bead pack was first saturated with continuous injection of brine of concentration 30,000 ppm at a rate of 2.5 ml/min to establish base permeability (calculated from Equation 3.10), a condition when differential pressure between inlet and outlet become stable. Subsequently, Arabian heavy crude oil having dynamic viscosity 16.5 cP at room temperature was injected into the brine saturated glass beads pack to flush out brine until oil emerged from the outlet and collected as the effluent. By carrying out this step, pore spaces are ensured to be filled with oil and brine of known initial saturation.

Once critical water saturation, S_{wc} is achieved and initial amount of oil contains in the porous medium can be determined, water flooding process takes place by continuously injecting brine of the same concentration at the same flow rate to replicate the secondary recovery stage. In estimate, 40% of the initial (original) oil in place will be displaced out during this stage before reaching residual oil saturation, S_{or} , leaving the remaining oil to be recovered in the next stage.

During enhanced oil recovery (EOR) stage, up to 2 pore volumes of EOR fluids were injected at a rate of 2.5 ml/min. In the absence of EM wave, three types of fluid were injected in different set of experiments. In the first experiment, SDS solution of concentration 0.3 wt% acts as a controlled experiment and therefore incremental recovery obtained from this injection will be used as the baseline or reference value in the subsequent experiments.

In the presence of EM wave, 59.96 MHz square wave alternating current was irradiated onto the porous medium during both nanofluid injections. Beyond 2 pore volumes (PV) of injection, critical oil saturation, S_{oc} is reached and EOR fluid injections were stopped. Recovery efficiency, E_R was calculated using the volume of oil recovered in EOR stage as a percentage of the oil present after water flooding (ROIP), as presented by Equation 3.16;

$$E_R (\%) ROIP = \left(\frac{\text{Volume of oil recovered in EOR fluid injection}}{\text{Volume of Remaining Oil in Place (ROIP)}} \right) \times 100 \quad (3.16)$$

A measurement model was designed in this experiment to overcome the limitation of the existing core flooding equipment, known as Relative Permeability System (RPS). By using the RPS, core flooding experiments can be conducted in reservoir temperature and pressure. However in this case, since electromagnetic wave is going to be applied throughout the nanofluid flooding, metal casing of the core holder made electromagnetic wave transmission into the porous medium impossible. Therefore, a measurement model as shown in Figure 3.14 was fabricated and used throughout the experiments.

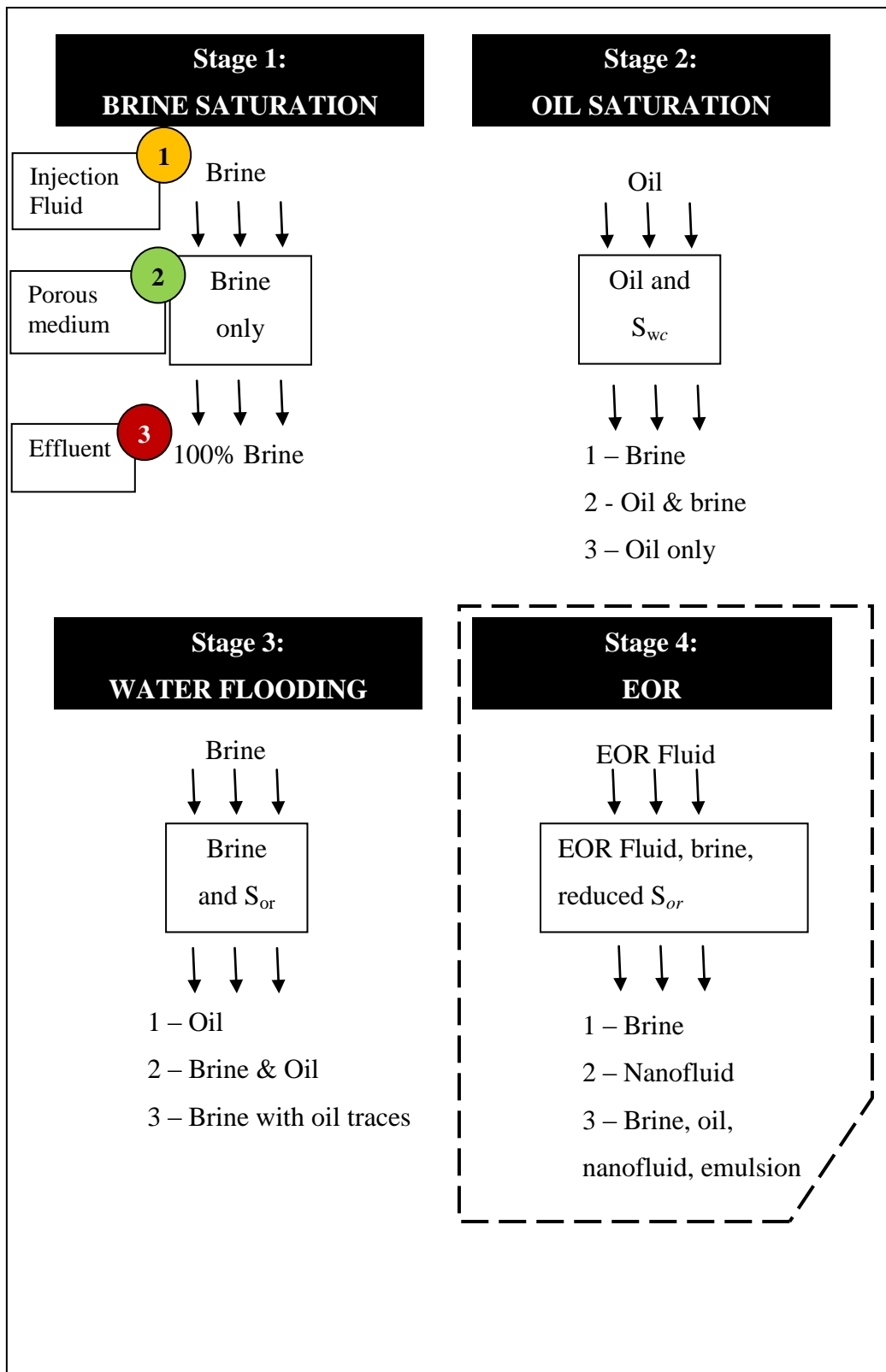


Figure 3.15: Stages of core flooding carried out for each EOR fluid

CHAPTER 4

RESULTS AND DISCUSSIONS

This chapter is divided into four major parts; nanoparticles characterization, nanofluid preparation and characterization, petro physical characterization and core displacement tests. All relevant results are tabulated and plotted to give clear picture on the findings.

4.1 Nanoparticles Characterization

As-synthesized nanoparticles were characterized using FESEM, EDX, XRD and TEM to understand their micro structural and crystallographic properties.

4.1.1 Characterization of zinc oxide nanoparticles

In the analysis of the structural properties of ZnO, five samples annealed at 200°C, 250°C, 300°C, 400°C and 500°C were compared. During synthesis, ZnO nanoparticles have been annealed in a programmable furnace at these five temperatures to observe the effect of annealing temperature on impurities removal and also crystallinity improvement. The annealing processes for all samples were conducted for 4 hours each at the same heating and cooling rate, as presented in Figure 4.1.

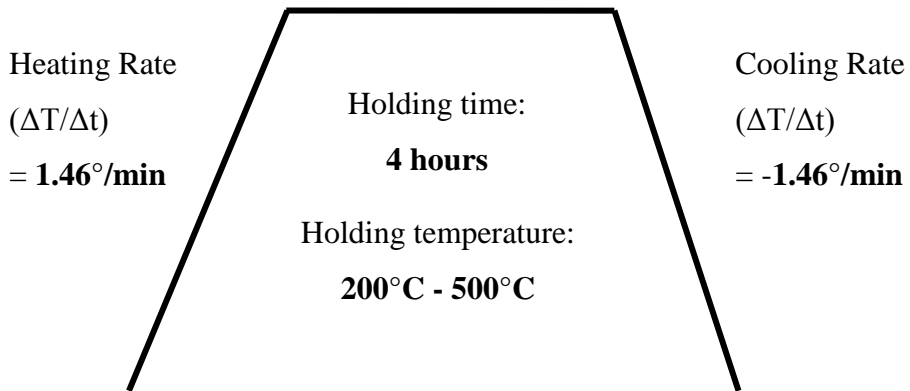


Figure 4.1: Variables considered in annealing process of ZnO nanoparticles

4.1.1.1 Field Emission Scanning Electron Microscopy (FESEM)

Figure 4.2 shows the FESEM images of the zinc oxide nanoparticles annealed at various temperatures. In overall, homogeneity in the shape and distribution of the particles was improved with the increase in annealing temperature. On top of that, the annealing temperature dominated microscopic structure and the morphology of ZnO particles i.e. from rod-like shape to flaky and pyramidal shape as shown in Figure 4.2(a)–(e). Yang et al (2008) had observed the growth of ZnO crystal in higher temperature; thermal energy is the driving force for the ZnO crystal to overcome anisotropic growth and hence, gives granular shape to the ZnO crystal [74]. At 500°C, formation of bigger particles having hexagonal bipyramidal shape of major axis length in the range of 1 to 5 μm was attributed to the diffusion of atoms across the grain boundaries. Particles of irregular shapes are also visible, most probably due to the presence of amorphous fraction, in agreement to the observation done by Kumar et al (2011) [75]. Music et al (2003) had further inspected ZnO particles morphology at various temperatures and found that they were actually hexahedrons of irregular shapes and sizes, as depicted in Figure 4.2(e) [76]. Since particles formed have tendency to agglomerate, the estimation of particle size was difficult and requires XRD analysis to calculate the average particle size using Scherrer equation, which will be further discussed in the following subsection.

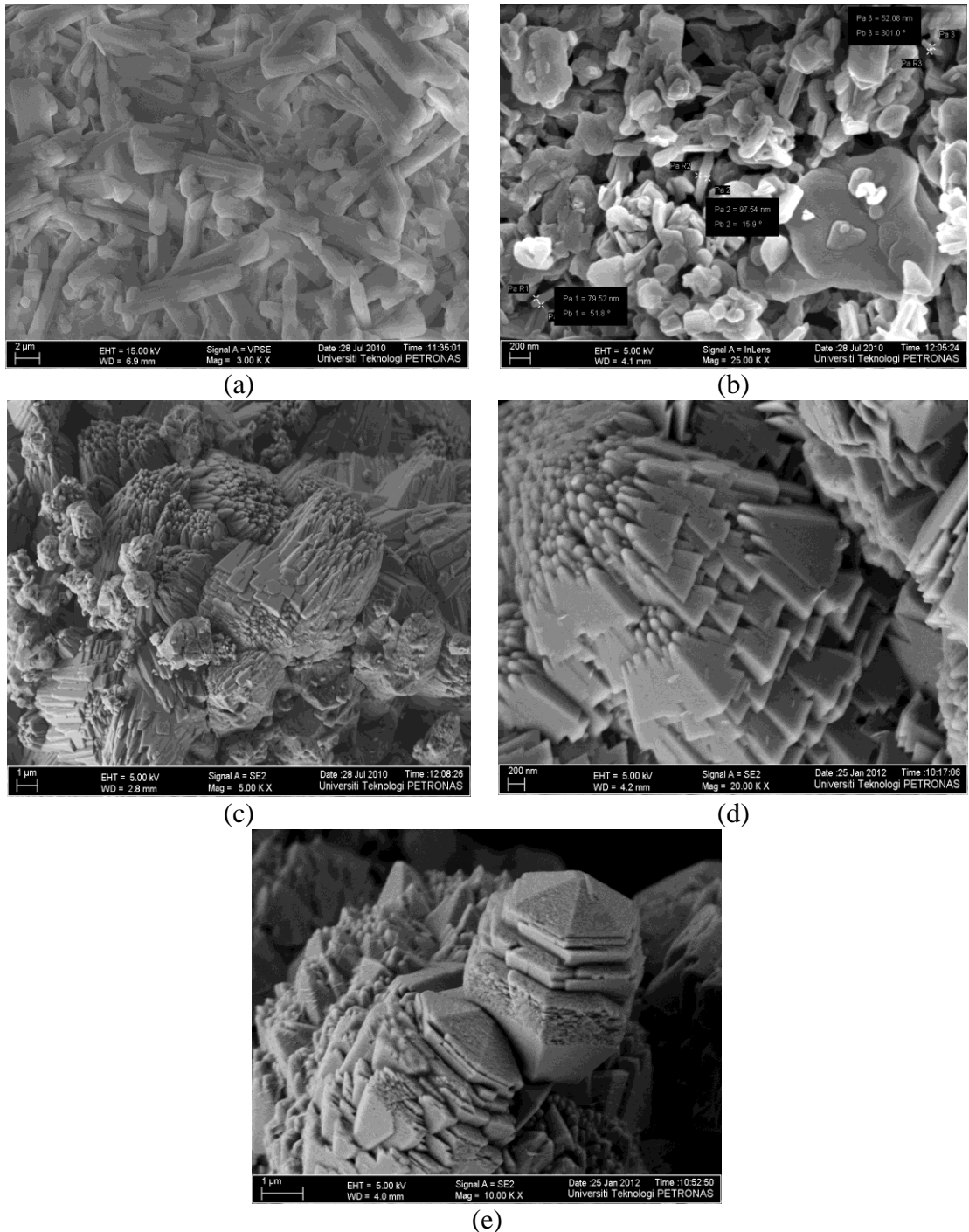


Figure 4.2:FESEM images for ZnO nanoparticles annealed at temperature (a) 200°C, (b) 250°C,(c) 300°C, (d) 400°C and (e) 500°C

4.1.1.2 X-Ray Diffraction (XRD)

In Figure 4.3, XRD patterns for all three ZnO samples are shown. All the detectable peaks can be indexed to the ZnO wurtzite structure, except for the sample annealed at 200°C. The reflection peaks clearly became sharper with increasing thermal decomposition temperature, indicating an enhancement of crystallinity. In other words, it was the “lowest-energy” theory that decided the preferential growing plane [63, 74]. From the analysis, annealing temperature of 200°C was not sufficient to remove excess zinc nitrate which was not completely decomposed during chemical reaction. However, at temperature 250°C, crystallinity starts to improve although small peaks of very low intensity present at low diffraction angles suggested that impurities are still present in the sample. Beyond 250°C, impurities starts to disappear and stable hexagonal wurtzite phase begin to form [77]. The average particles size in nanometers, D_{hkl} were determined by means of an X-ray line-broadening method using Scherer equation (Equation 4.1),

$$D_{hkl} = \frac{k\lambda}{\beta_{hkl} \cos \theta} \quad (4.1)$$

where k is the Scherrer constant, which was chosen to be 0.89 in this analysis, λ is the wavelength of the X-ray used in the diffractometer, β_{hkl} is the peak width at half-maximum intensity and θ is the peak position.

Crystallinity and annealing temperature had contributed to the average crystallite size of the ZnO nanoparticles, whereby size of the crystals were larger as the annealing temperature increase and atoms become more orderly arranged. As shown in Table 4.1, crystallite size of ZnO nanoparticles increases from 45.67 nm (annealed at 250°C) to 96.10 nm and 84.37 nm, after being annealed at 400°C and 500°C, respectively. Crystallinity improvement of these wurtzite structures can be observed by the change in the lattice constants; a and c . The lattice constants mostly range from 3.2475 to 3.2501 Å for the a -parameter and from 5.2042 to 5.2075 Å for the c -parameter. The c/a ratio varies in a slightly wider range, from 1.593 to 1.6035, which typically has the value of 1.633 for ideal wurtzite structure. The deviation from that of the ideal wurtzite crystal is probably due to lattice stability and ionicity. Morkoc et al

(2009) has reported that free charge is the dominant factor responsible for increasing lattice constants, as well as defects in crystals such as zinc antisites, oxygen vacancies, and threading dislocations [62].

Table 4.1: Comparative values of crystal planes, d-spacing, lattice parameter, structure and crystallite size of ZnO nanoparticles annealed at various temperatures

X-Ray Diffraction						
Samples	Standard Reference Card No. (SS>NNNN)	Crystal planes (h k l)	d-spacing (Å)	d_{hkl} (nm)	Lattice parameter	Structure
ZnO 500	89-0511 (C)	(1 0 1)	2.475	84.37	$a = 3.249$ $c = 5.205$ $c/a = 1.60$	Hexagonal
ZnO 400	79-2205 (C)	(1 0 1)	2.478	96.10	$a = 3.250$ $c = 5.207$ $c/a = 1.60$	Hexagonal
ZnO 300	89-0511 (C)	(1 0 1)	2.473	44.95	$a = 3.249$ $c = 5.205$ $c/a = 1.60$	Hexagonal
ZnO 250	79-2205 (C)	(1 0 1)	2.474	45.67	$a = 3.250$ $c = 5.207$ $c/a = 1.60$	Hexagonal
ZnO 200	70-1361 (C)	(1 0 0)	6.924	67.57	$a = 7.038$ $c = 11.182$ $c/a = 1.59$	Monoclinic

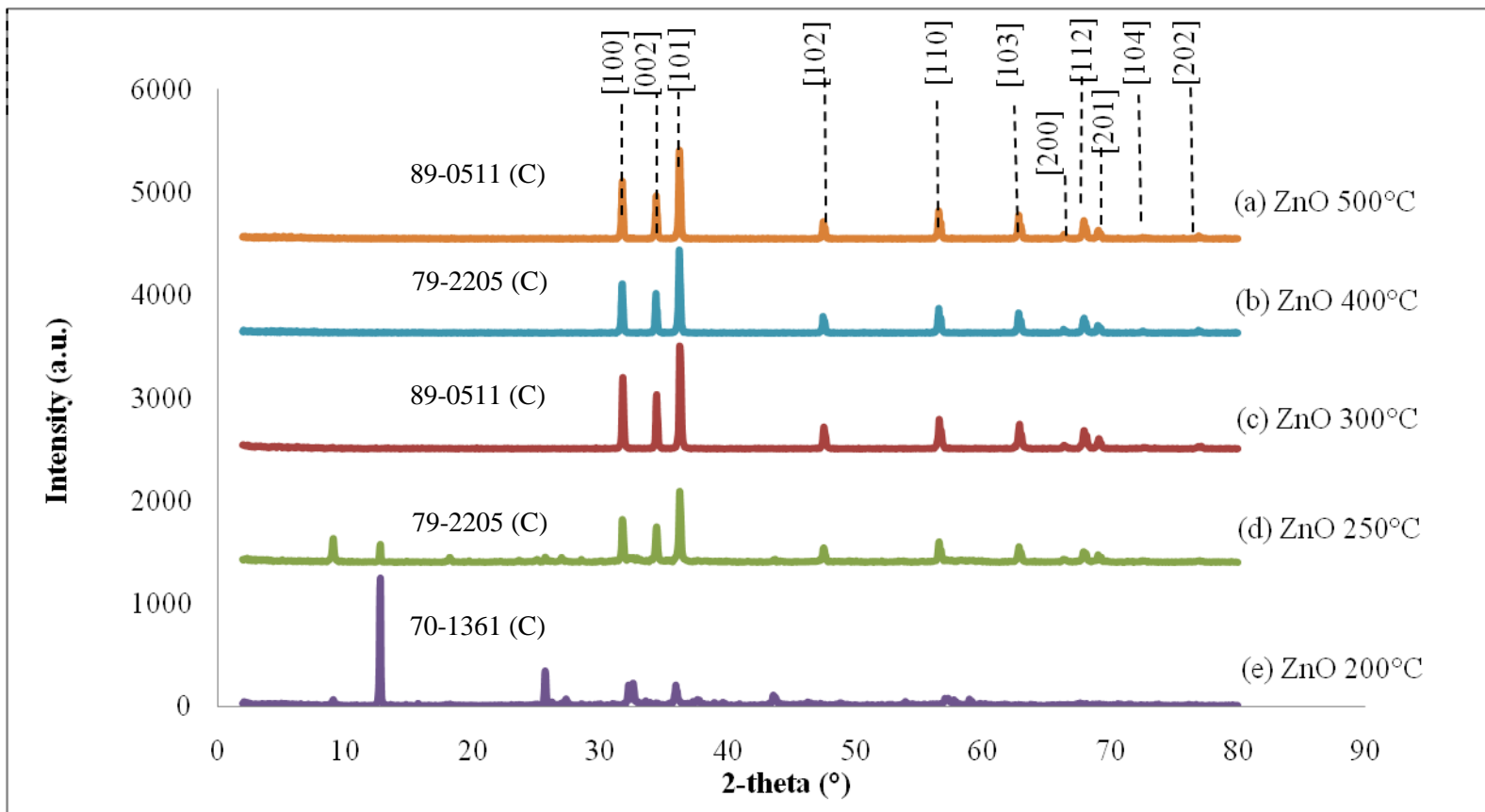


Figure 4.3: XRD pattern for ZnO nanoparticles annealed at temperature (a) 500°C, (b) 400°C, (c) 300°C, (d) 250°C and (e) 200°C

4.1.1.3 Energy Dispersive X-Ray (EDX)

Elemental composition of the samples was identified from EDX analysis by using OXFORD INCA X-ray Microanalysis system. The atomic and weight percentages of these elements together with the deviation analysis were gathered in Table 4.2. From the EDX analysis, presence of Zn and O are evident by the relative abundance of each of the element which is comparable to the theoretical stoichiometric values. It can be concluded that ZnO nanoparticles produced were of high purity, with the presence of no element other than Zn and O in the compound. Zinc to oxygen atoms ratio should be kept unity based on the chemical formula, however from the elemental analysis, a slight deviation in the atomic percentage was observed. Standard atomic weight of oxygen atom is 15.9994g/mol and 65.38g/mol for zinc. From this EDX analysis, there is a huge deviation in weight percentage for zinc oxide samples sintered at temperature 200°C and 250°C, however smaller deviation was observed for the zinc oxide sample annealed at 300°C as the annealing temperature is sufficient to remove residual impurities.

4.1.1.4 Transmission Electron Microscope (TEM)

Based on the TEM micrographs shown in Figure 4.4, 2-propanol or iso-propanol was not a good dispersion agent for ZnO nanoparticles. Severe agglomeration can be observed even though nanoparticles suspension was agitated in an ultrasonic bath for one hour. However under magnification of 200,000 times, image of rod-like particles having nearly hexagonal shape of different diameter and length can be observed, as shown in Figure 4.4(a). In comparison to the d -spacing calculated using Scherrer method from XRD analysis, 0.49% deviation was found in determination of the d -spacing from TEM imaging. Based on a study conducted by Khorsand Zak et al (2011), this deviation was attributed to presence of strain on the particles by atoms on the surface due to surface effect, especially when the particles to be measured are very small. However this strain effect does not present in XRD measurement [78].

Table 4.2: Elemental distribution analysis of ZnO nanoparticles annealed at various temperatures

Sample	Element	Measured weight (%)	Standard atomic weight (g/mol)	Theoretical percentage of weight (%)	Percentage difference (%)	Measured atomic ratio	Theoretical atomic ratio	Percentage difference (%)
ZnO 500	O	17.58	15.9994	19.66	-10.58	46.56	50.00	-6.88
	Zn	82.42	65.3800	80.34	2.59	53.44	50.00	6.88
ZnO 400	O	19.55	15.9994	19.66	-0.56	49.82	50.00	-0.36
	Zn	80.45	65.3800	80.34	0.14	50.18	50.00	0.36
ZnO 300	O	20.36	15.9994	19.66	3.56	51.09	50.00	2.18
	Zn	79.64	65.3800	80.34	-0.87	48.91	50.00	-2.18
ZnO 250	O	28.53	15.9994	19.66	45.12	61.99	50.00	23.98
	Zn	71.47	65.3800	80.34	-11.04	38.01	50.00	-23.98
ZnO 200	O	51.79	15.9994	19.66	163.42	81.44	50.00	62.88
	Zn	48.21	65.3800	80.34	-39.99	18.56	50.00	-62.88

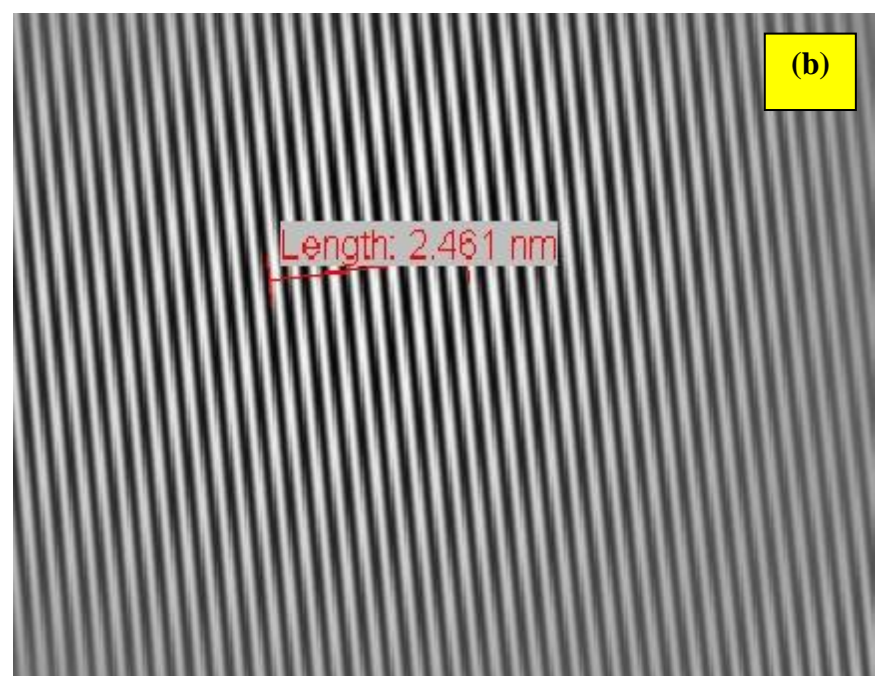
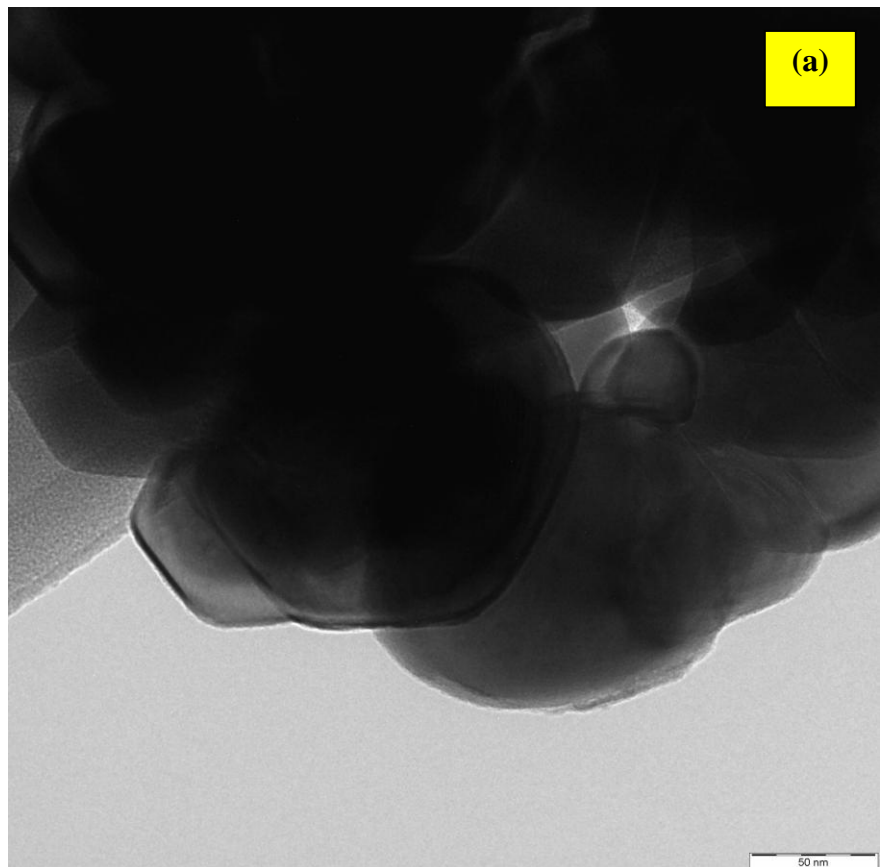


Figure 4.4: TEM micrographs of ZnO 300 dispersed in isopropanol (a) under magnification of 200,000 times and (b) diffraction line to determine the d -spacing

4.1.2 Characterization of aluminium oxide nanoparticles

In the analysis of the structural properties of Al_2O_3 , three samples annealed at 900°C, 1000°C and 1100°C were compared to observe the effect of annealing temperature on impurities removal, as well as crystallinity improvement. The annealing processes for all samples were conducted for 4 hours at the same heating and cooling rate, at holding temperature ranging from 900°C to 1100°C, as presented in Figure 4.5.

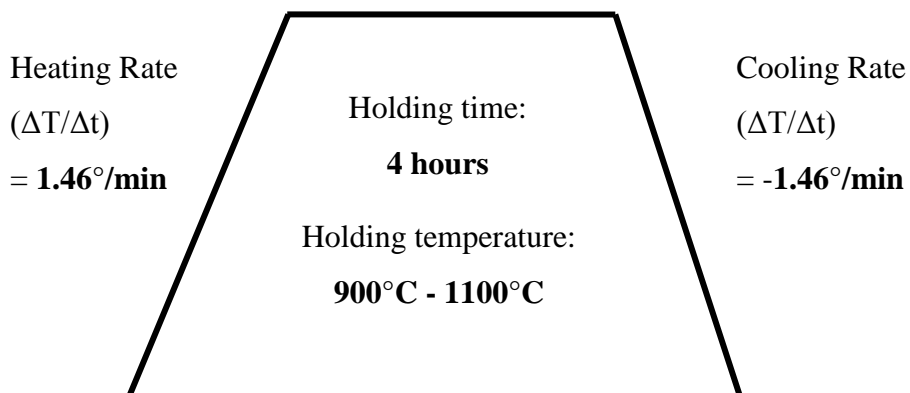


Figure 4.5: Variables considered in annealing process of Al_2O_3 nanoparticles

4.1.2.1 Field Emission Scanning Electron Microscopy (FESEM)

FESEM images for Al_2O_3 nanoparticles are shown in Figure 4.6(a), (b) and (c). From the morphology analysis, crystallinity and homogeneity of the nanoparticles began to improve when the annealing temperature increases. As shown in Figure 4.6(a), at 900°C, homogeneous fibrous network of nanoparticles could be observed in throughout the sample. Continuation of firing through 1000°C did not change the morphology significantly; however the texture appears to be coarser and more void space is present between the particles, as shown in Figure 4.6(b). Upon heating to 1100°C, pore networks were clearly observed on the surface and distinct

grain boundaries formed to give spherical features of dimensions around 60 to 200 nm, which is depicted in Figure 4.6(c). Jones et al (2007) had demonstrated almost similar results and predicted that this phenomenon was attributed to the smaller particles being sintered together causing a collapse in the small pores resulting in the formation of larger, less dense pores [79]. More accurate estimation of the crystallite size of Al_2O_3 nanoparticles will be further discussed in the following subsection.

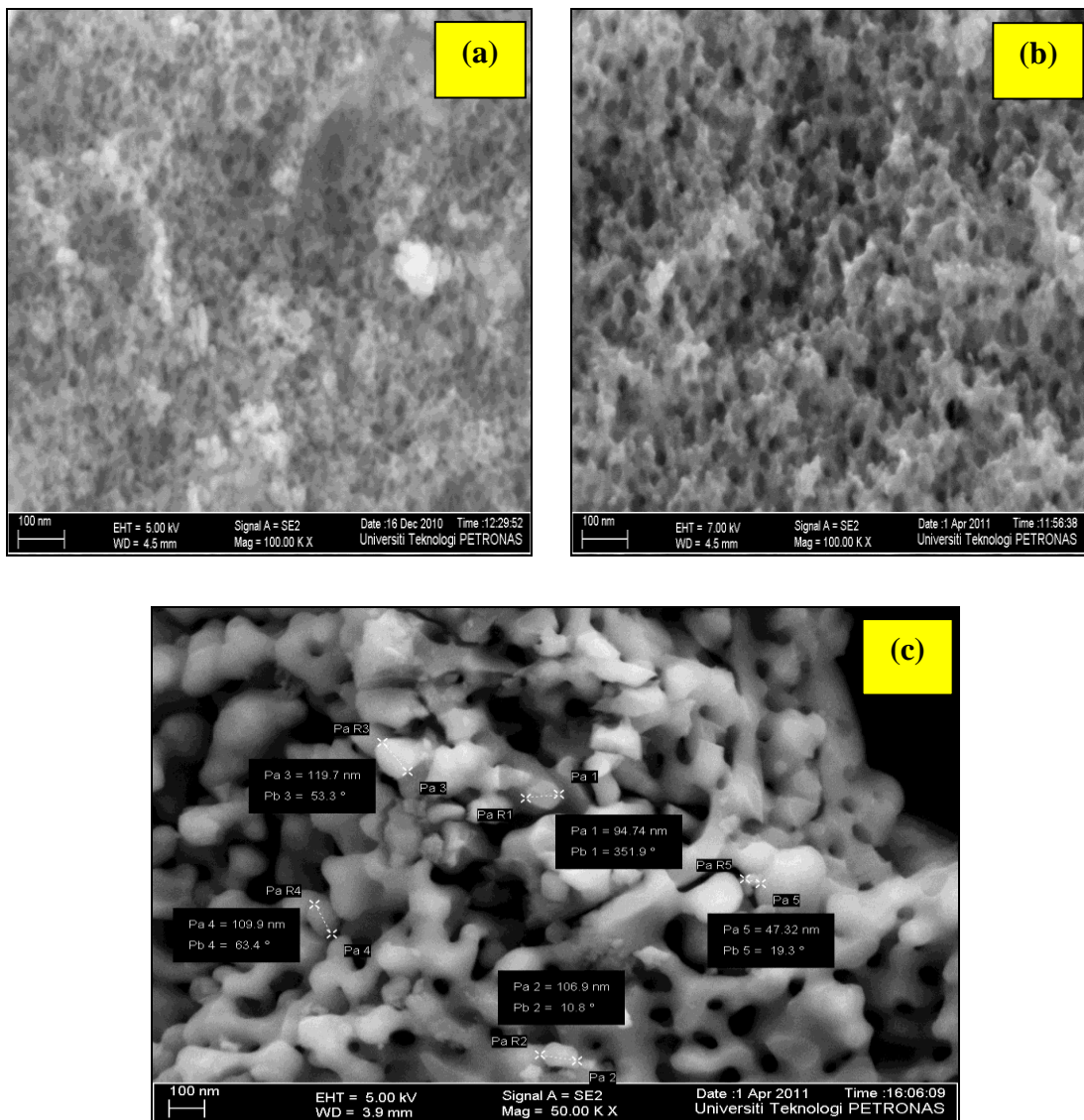


Figure 4.6: FESEM images of Al_2O_3 nanoparticles annealed at temperature (a) 900°C, (b) 1000°C and (c) 1100°C

4.1.2.2 X-Ray Diffraction (XRD)

XRD patterns for Al₂O₃ nanoparticles annealed at three different temperatures are shown in Figure 4.8. All visible peaks of sample annealed for 4 hours in air at 1100 °C can be indexed to the Al₂O₃ hexagonal structure. Annealing temperature does play a significant role in improving the crystallinity of the final product. Transformation of alumina gel to γ -alumina upon annealing occurs at 900°C and subsequently to α -alumina at about 1200°C [80]. Diffraction patterns for material annealed at temperature lower than 1000 °C are highly attenuated due to the presence of amorphous state having good adsorbent properties owing to their high specific surface area and more active sites on their surfaces [81]. However, it can be seen that Al₂O₃ peaks have became better defined and have higher intensities as the annealing temperature is increased.

As summarized in Table 4.3, it is observed that there is a little change in the lattice parameters when the annealing temperature is increased. Changes in the lattice parameter can be affected by free charge, impurities, stress, particle size, quantum size effects and temperature [81, 82]. For Al₂O₃, the phase transformation of the xerogels after annealed at increasing temperature is shown in Figure 4.7. As the xerogels formed, orthorhombic boehmite phase dominates the structure and transformed into tetragonal δ -Al₂O₃ around 900°C, before it begins to exhibit hexagonal α -Al₂O₃ at 1100°C. From a study conducted by Jones et al (2007), these phase changes are known to be topotactic, a condition where changes in the crystal structure are accomplished with no changes in crystalline morphology. However, each phase change is accompanied by a change in porosity [79].

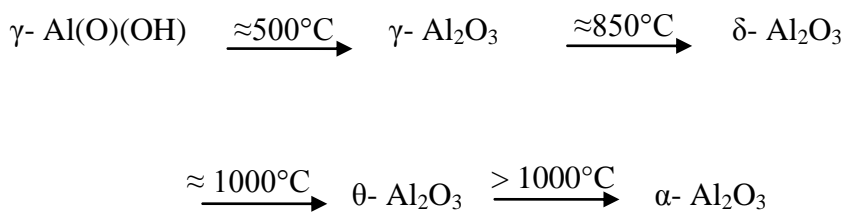


Figure 4.7: Phase transformation of Al₂O₃ xerogel after annealed at increasing temperature [71]

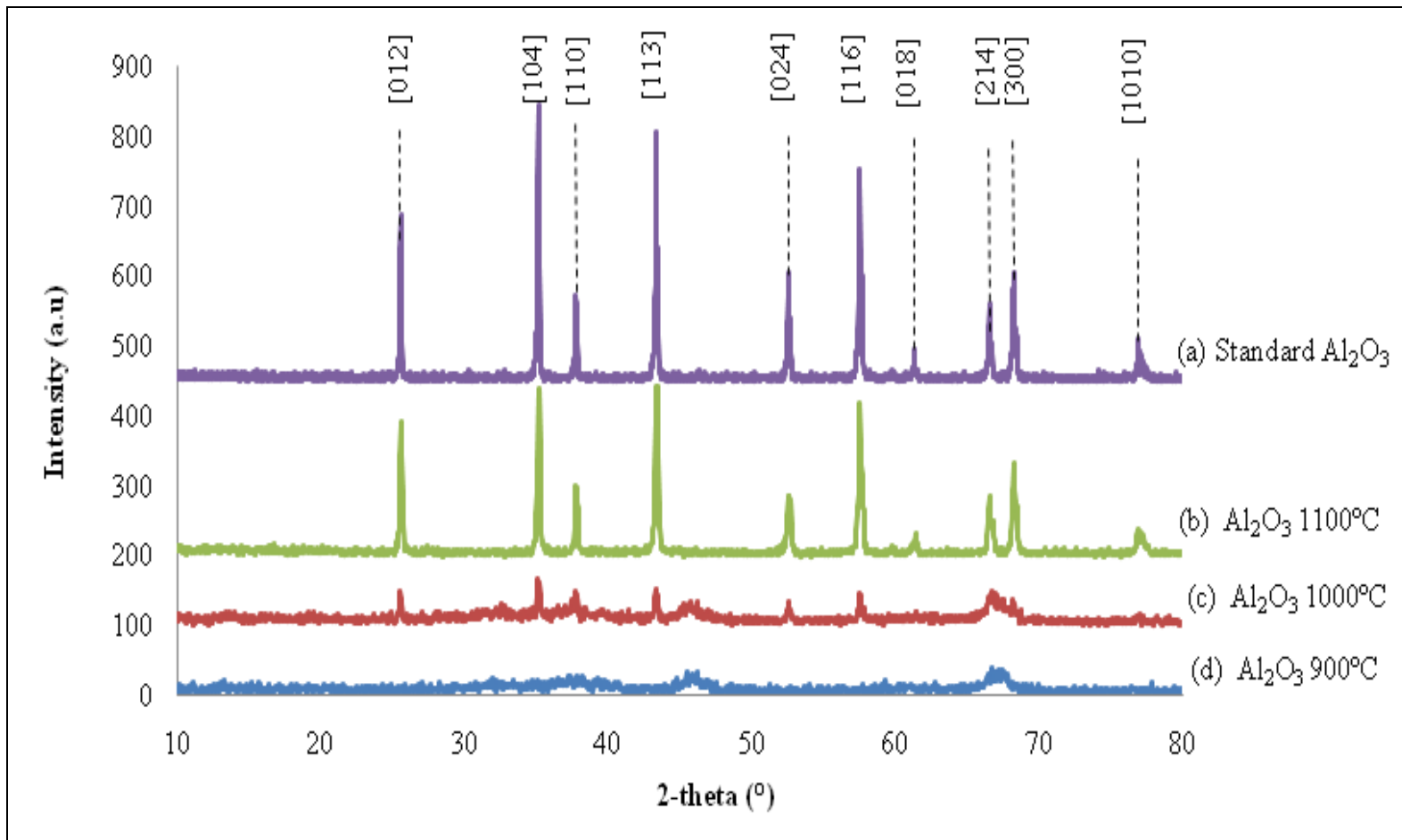


Figure 4.8: XRD Pattern for (a) standard Al_2O_3 nanoparticles and annealed at temperature (b) 1100°C, (c) 1000°C and (d) 900°C

Table 4.3: Comparative Values of Crystal Planes, d-spacing, Lattice Parameter, Structure, Crystallite Size of Al_2O_3 Nanoparticles Annealed at Various Temperatures

X-Ray Diffraction						
Samples	Standard Reference Card No. (SS-NNNN)	Crystal planes (h k l)	d-spacing (Å)	d_{hkl} (nm)	Lattice parameter	Structure
Al_2O_3 1100°C	81-1667 (C)	(1 1 3)	2.084	38.3	$a = 4.76$ $c = 12.99$ $c/a = 2.73$	Hexagonal
Al_2O_3 1000°C	83-0065 (C)	(1 0 4)	2.554	55.7	$a = 7.86$ $c = 5.65$ $c/a = 0.72$	Monoclinic
Al_2O_3 900°C	88-1609 (C)	(2 1 4)	1.402	15.6	$a = 5.59$ $c = 23.66$ $c/a = 4.23$	Tetragonal

4.1.2.3 Energy Dispersive X-Ray (EDX)

Elemental composition of the samples was identified from EDX analysis by using OXFORD INCA X-ray Microanalysis system. The atomic and weight percentages of these elements together with the deviation analysis were gathered in Table 4.4. From the EDX analysis, presence of aluminum and oxygen atoms is evident by the relative abundance of each of the element which is comparable to the theoretical stoichiometric values. It can be concluded that Al_2O_3 nanoparticles produced were of high purity, with an observable enhancement in the purity of the chemical composition as the annealing temperature increases from 900°C to 1100°C. After annealed at temperature lower than 1100°C, huge difference in the weight ratio takes place, which attributed to the presence of impurities derived from starting materials and metal ions having a different melting temperature [75]. Aluminum to oxygen atoms ratio should be kept 2:3 based on the chemical formula, however from the

elemental analysis, a slight deviation in the atomic percentage was observed. Standard atomic weight of oxygen atom is 15.9994g/mol and 26.9815g/mol for aluminum. From this EDX analysis, it can be concluded that annealing temperature higher than 1100°C is required to sufficiently remove residual water and impurities.

Table 4.4: Comparison of Weight and Atomic Ratio from EDX Analysis of Al_2O_3 Nanoparticles

Sample	Element	Measured Weight Ratio (%)	Standard Atomic Weight (g/mol)	Theoretical Weight Ratio (%)	Percentage Difference (%)	Measured Atomic Ratio (%)	Theoretical Atomic Ratio (%)	Percentage Difference (%)
Al_2O_3 1100°C	O	54.01	15.9994	47.07	14.73	66.45	60.00	10.75
	Al	45.99	26.9815	52.93	-13.10	33.55	40.00	-16.13
Al_2O_3 1000°C	O	52.21	15.9994	37.22	40.26	64.82	60.00	8.03
	Al	47.79	26.9815	62.78	-23.87	35.18	40.00	-12.05
Al_2O_3 900°C	O	54.42	15.9994	37.22	46.19	66.82	60.00	11.37
	Al	45.58	26.9815	62.78	-27.39	33.18	40.00	-17.05

4.1.2.4 Transmission Electron Microscope (TEM)

TEM micrographs shown in Figure 4.9 gives the information on the d-spacing and morphology of the synthesized Al_2O_3 nanoparticles. Since Al_2O_3 nanoparticles was severely agglomerated in iso-propanol, identification of the morphology and particle size could not accurately done. Under magnification of 200,000 X, image of particle having nearly hexagonal shape can be observed, as shown in Figure 4.9(a). In comparison to the d -spacing calculated using Scherrer method from XRD analysis, 35.32% deviation was found in determination of the d-spacing from TEM imaging, as depicted in Figure 4.9(b). Based on a study conducted by Khorsand Zak et al (2011), this deviation was attributed to presence of strain on the particles by atoms on the surface due to surface effect, especially when the particles to be measured are very small. However this strain effect is not present in XRD measurement [78].

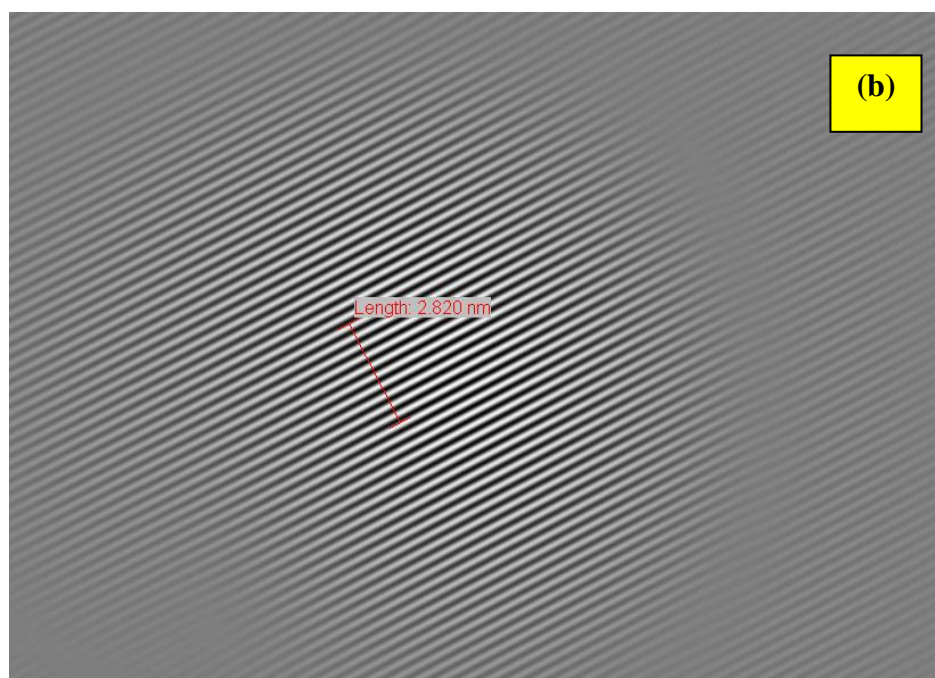
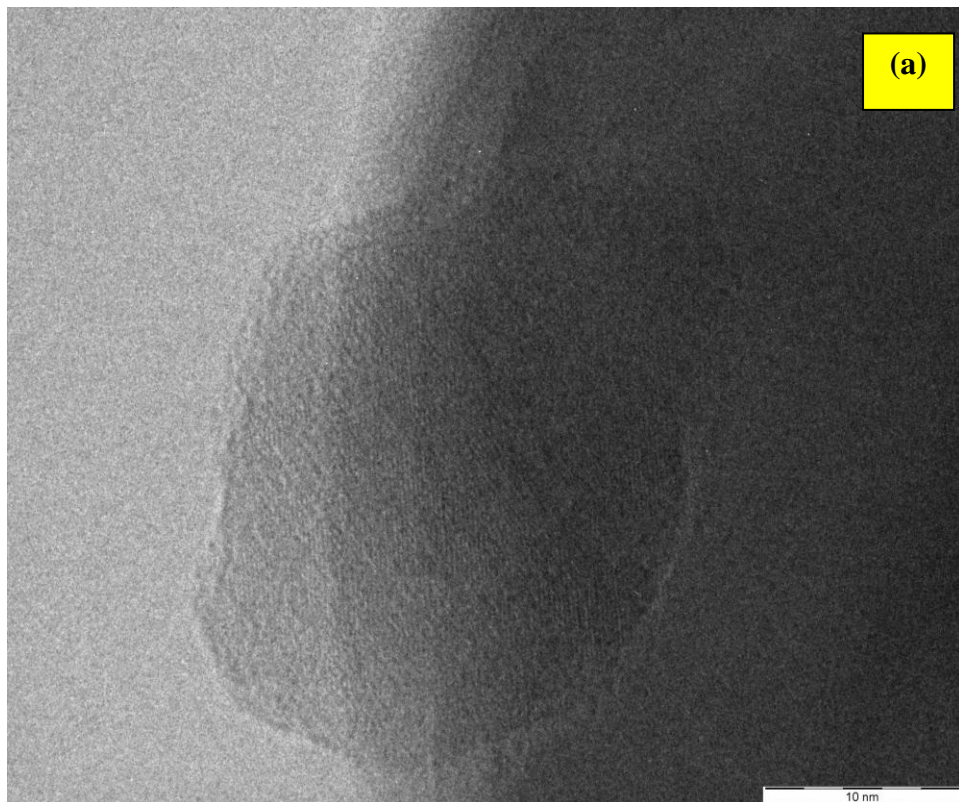


Figure 4.9: TEM micrographs of Al_2O_3 dispersed in isopropanol (a) under magnification of 200,000kX and (b) diffraction line to determine the d -spacing

4.2 Nanofluid Characterization

In this section, both nanoparticles that were previously dispersed in deionized water were tested for dielectric properties, interfacial tension and viscosity.

4.2.1 Dielectric properties

Comparison of the dielectric properties i.e. dielectric constant or permittivity, loss factor and loss tangent were done to determine which material will give better performance as ER fluid. Figure 4.10, 4.11 and 4.12 show the frequency dependent spectra of the dielectric properties of both Al₂O₃ and ZnO nanoparticles suspensions. Al₂O₃ annealed at temperature 1100°C and ZnO annealed at temperature 300°C were chosen as the best samples based on their micro structural properties and crystallography. Relationship between the dielectric properties of both nanoparticles suspension with respect to the frequency was studied by deducing the relative permittivity, loss factor and loss tangent values from the parallel capacitance measurement.

4.2.1.1 Permittivity

Permittivity of a material indicates the amount of energy from external field that can be stored in a material. The higher the permittivity value, more charges can be stored inside [83]. For ER material, permittivity or dielectric constant of the material indicates the ease of polarization to take place when it is exposed to an electric field. From the dielectric permittivity spectra shown in Figure 4.10, it is found that permittivity decreases sharply when frequency is increased. Reduction in the permittivity indicates that the space charge carriers cannot follow the change of measuring electric field. Heating up the sample during the sintering process increases the number of thermally activated charge carriers accumulated at the grain boundaries. Therefore at low frequency region, increase in the activated charge carriers leads to an increase in the dielectric permittivity, which corresponds to the increase in space charge polarization [84]. High permittivity value at frequency

between 10^2 - 10^5 Hz infers the ability of ZnO nanoparticles suspension to store larger amount of energy in the low frequency range, as compared to Al₂O₃ which has lower permittivity. In overall, similar behaviour has been exhibited by both nanofluids which have significant frequency dispersion being observed in the low frequency region but begin to behave independently beyond 10^5 Hz. Existence of water as the base fluid also contributes to the extremely high permittivity at low frequency region where interfacial polarization process dominates the polarization mechanism [85]. Large quantity of the boundary atoms resided in the grain interfaces and within a few atomic layers from the interface are the unique characteristics of nanostructured materials. Frequency of the external electric field plays a major role in the polarization process by maximizing the contribution of space-charge polarization and orientational polarization occurring at the interfaces into the dielectric permittivity [84].

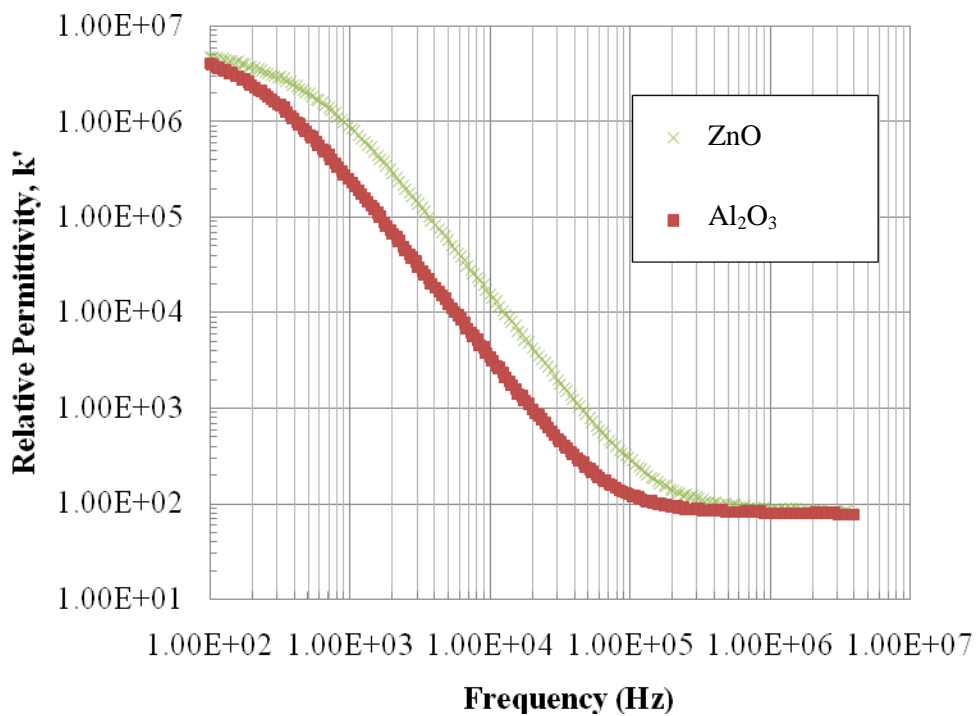


Figure 4.10: Relative permittivity spectra of ZnO and Al₂O₃ nanofluids measured in frequency sweep of 100 Hz to 4 MHz

4.2.1.2 Loss Factor

The dielectric loss factor relates to the inability of molecules to undergo realignment with an alternating electric field. This ability is reliant on frequency of the alternating field, the temperature of the sample, the size of the molecules involved, and their polarity [86]. From Figure 4.11, it is clearly shown that Al_2O_3 has higher dielectric loss as compared to ZnO for the entire frequency range (10^2 - 10^7 Hz). At the lowest measurable frequency (10^2 Hz), dielectric loss of Al_2O_3 is 2.60×10^6 , which is 45.3% higher than that of ZnO at the same frequency. This may be attributed to the extrinsic crystal structure defects that the material has e.g. high porosity, random crystallite orientation and impurities, as described in the FESEM and EDX analysis [87].

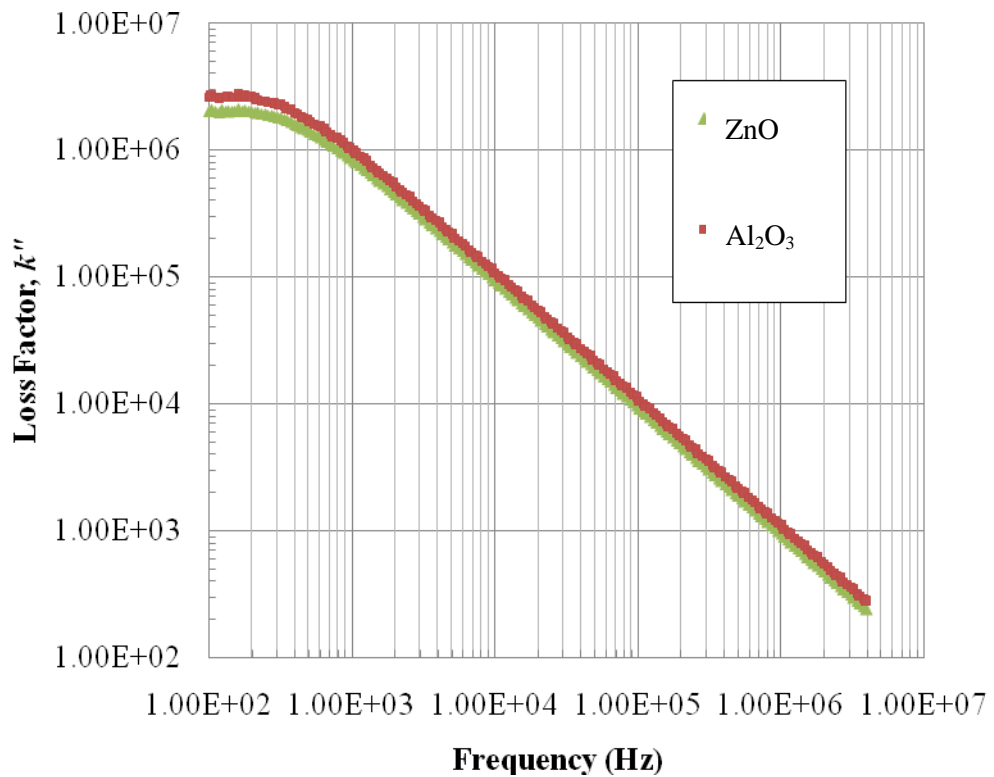


Figure 4.11: Loss factor spectra of ZnO and Al_2O_3 nanofluids measured in frequency sweep of 100 Hz to 4 MHz

4.2.1.3 Loss tangent

Loss tangent could be used to summarize both abovementioned dielectric properties. It is a ratio of dielectric loss, k'' to the dielectric constant, k' . High loss tangent infer that the material has high ability to convert the stored energy into another form of energy e.g. heat.

From Figure 4.12, it is clearly shown that Al_2O_3 has higher loss tangent compared to ZnO , which implies that higher interfacial polarization will occur in Al_2O_3 nanofluid [38]. However, it peaks at different frequency values, which clearly indicates that for lower frequency application, Al_2O_3 gives the better ER performance compared to ZnO which peaks at slightly higher frequency.

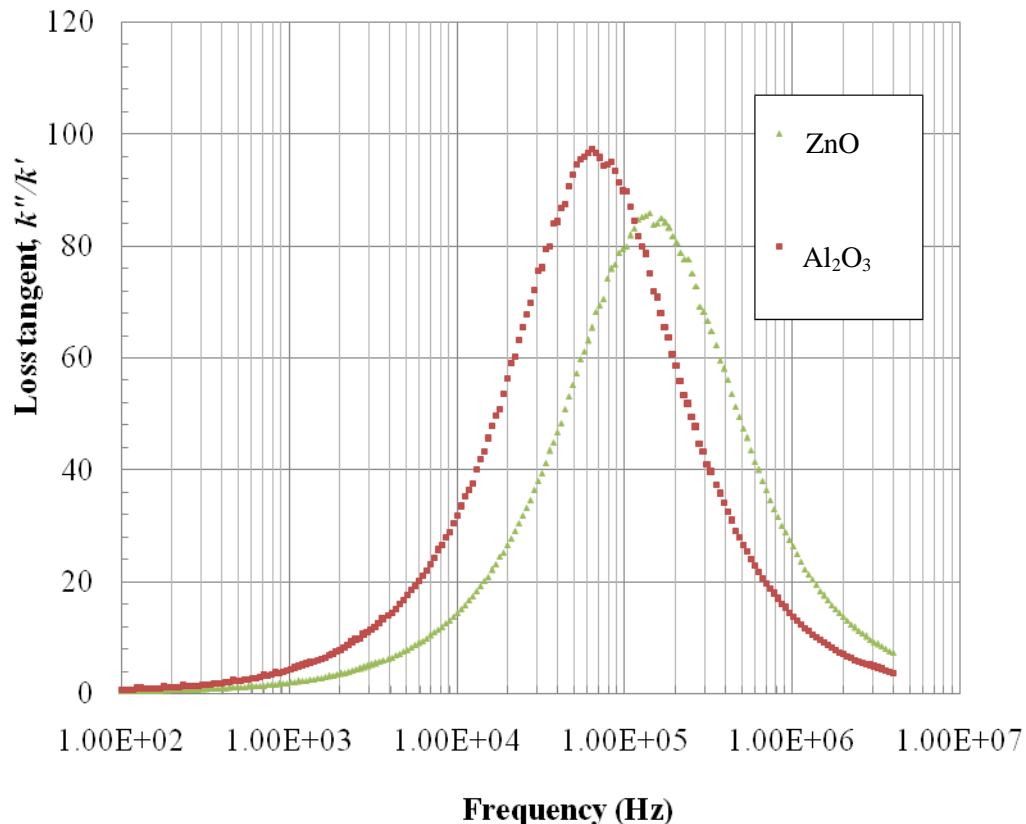


Figure 4.12: Loss tangent spectra of ZnO and Al_2O_3 nanofluids measured in frequency sweep of 100 Hz to 4 MHz

4.2.2 Interfacial tension (IFT) measurement

Interfacial tension values between crude oil and various injection fluids containing nanoparticles and surfactant were measured and compared, as presented in Table 4.5. There were four types of fluids involved in the measurement. Dynamic or time dependent measurement methods were often used to obtain equilibrium tension values in a prolonged duration, as shown in Figure 4.13 [88]. Initially, oil-brine IFT value was measured as 19.59 mN/m, almost in the range of typical oil-brine IFT, which is around 20-50 mN/m [89]. When 0.3 wt% of aqueous SDS solution is in contact with the crude oil, the IFT value was tremendously decreased to 2.82 mN/m. When SDS molecules are adsorbed at the interface, their hydrophobic tails will reside on the non-polar phase, and their hydrophilic head preferentially orientated towards the aqueous solution, leading to tremendous reduction in interfacial tension [90].

When the same aqueous SDS solution was used as the base fluid for the nanoparticles suspensions, the IFT values slightly increases as compared to that of the base fluid itself. In mixed systems, the more rapidly adsorbing surfactant was originally located at the interface, and gradually, particles will be irreversibly adsorbed at the interface to replaced surfactant molecules, leading to an increase in surface tension. Once at the interface, a particle can be thought of as irreversibly absorbed, behavior unlike surfactants, which are generally thought to be in a state of dynamic equilibrium, absorbing and desorbing on a fast timescale [91]. Other factor which contributes to the increase in IFT values is the particles size. Kinetic study of CdSe nanoparticles on oil-water interface conducted by Kutuzov et al. (2007) shows that when nanoparticle size decreases, the rate of adsorption of the nanoparticles will subsequently decrease. Therefore lower IFT value could be observed in ZnO nanofluids having larger particle size in average, in comparison with Al₂O₃ nanofluids [92].

Table 4.5: Dynamic interfacial tension value between crude oil and injection fluids

Time (s)	IFT (mN/m)			
	Brine	SDS	ZnO	Al ₂ O ₃
60	20.719	2.825	4.018	4.157
120	21.197	2.833	4.044	4.411
180	20.831	2.856	4.145	4.372
240	20.165	2.865	4.108	4.373
300	20.397	2.872	4.032	4.393
360	19.934	2.881	4.190	4.417
420	20.530	2.897	4.105	4.438
480	20.371	2.900	4.099	4.487
540	20.628	2.902	4.113	4.371
600	20.682	2.904	4.108	4.383
660	20.411	2.910	4.096	4.363
720	20.412	2.915	4.128	4.375
780	20.897	2.920	4.127	4.389
840	20.207	2.925	4.104	4.468
900	19.907	2.932	4.186	4.519
960	19.778	2.935	4.129	4.502
1020	20.450	2.940	4.097	4.408
1080	20.142	2.949	4.119	4.464
1140	20.117	2.955	4.173	4.352
1200	20.131	2.957	4.171	4.512
1260	20.003	2.958	4.169	4.410
1320	19.688	2.965	4.101	4.415
1380	19.784	2.971	4.170	4.366
1440	19.851	2.975	4.092	4.525
1500	19.675	2.981	4.108	4.512
1560	19.965	2.988	4.107	4.353

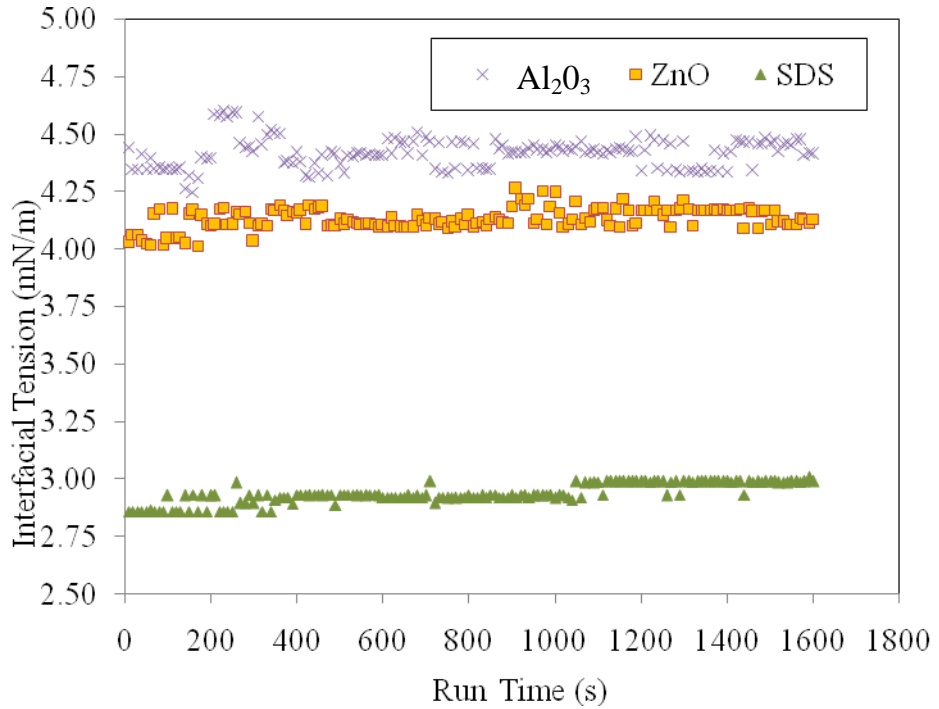


Figure 4.13: Dynamic IFT measurement of the injection fluids

4.2.3 Viscosity measurement

Table 4.6 shows the kinematic viscosity of the base fluid and the nanoparticles suspension. As predicted earlier, viscosity of the suspensions will be higher than its base fluid with nanoparticles addition. Among those three injection fluids, Al_2O_3 nanofluid has slightly higher viscosity which could be due to particle clustering and interactions and also interparticle potential such as Van der Waals forces [93].

Table 4.6: Kinematic viscosity of the injection fluid

Injection fluid	Viscosity (cP)
SDS	0.94
ZnO	1.24
Al_2O_3	1.60

Again, particle size exhibit significant effect on the properties of the suspension as their viscosity increases in proportion to the particle size reduction. This was proven from calculation using Derjaguin–Landau–Verwey–Overbeek (DLVO) theory which states that the total inter-particle potential energy is mainly the sum of van der Waals attraction and electrical double layer repulsion. Therefore, when particle size is reduced, the interparticle repulsion force increases as the total surface area increases, resulting in net increase of bulk viscosity of the suspension [94].

Since changes in the viscosity of the nanofluids in the presence of electromagnetic waves irradiation could not be measured, an indirect approach of measuring the viscosity was conducted by using Darcy equation (Equation 3.10), from which the viscosity value at particular fluid injection could be deduced, provided the flow rate, dimension of the porous medium and viscosity of the fluid are known.

4.3 Petrophysical properties characterization

Prior to core flooding experiments, the properties of fluids and porous medium to be used throughout the experiments were measured and evaluated to know the exact amount of fluid that could be contained in a porous medium at particular injection stage.

4.3.1 Reservoir fluid properties

Arabian Heavy crude oil was used as the reservoir fluid throughout the experiments. Thus, to understand its rheology variation with temperature, kinematic viscosity was measured by varying the temperature of the crude oil. From this measurement, relationship between the kinematic viscosity of the crude oil and temperature was found to be inversely proportional. Efflux time describes the time taken for the crude oil to travel through the orifice of a capillary under the force of gravity, which became shorter as the temperature gets higher. The relationship between efflux time and kinematic viscosity with temperature is tabulated and plotted in Table 4.7 and Figure 4.14, respectively. However, only data derived from

measurement at 60°C was used in this research since it is the typical temperature of oil reservoirs in Arabian fields.

Table 4.7: Viscosity of the Arabian Heavy crude oil with temperature variation

T (°C)	Efflux Time (s)	Viscosity (mm ² /s @ cSt)
30.0	407.71	20.39
40.0	368.28	18.41
50.0	283.10	14.16
60.0	233.19	11.66
70.0	156.97	7.85
80.0	124.53	6.23

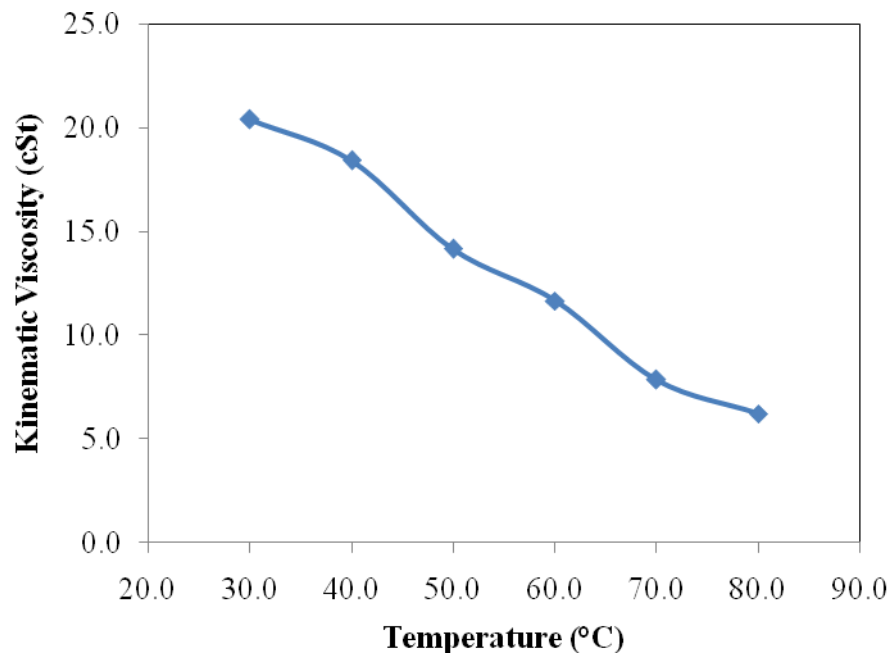


Figure 4.14: Plot of kinematic viscosity versus temperature of the Arabian Heavy crude oil from 25°C to 80°C

4.3.2 Reservoir rock properties

Permeability and porosity of the glass beads mixtures were measured. As shown in Table 4.8, permeability of different mixtures varied due to the bead size variation in

the packing. It can be concluded than uniform bead size packing will contribute to a high permeability value, whereas mixture of different sizes will give smaller permeability value.

Table 4.8: Permeability and porosity of the glass bead packs

Average mesh size (μm)	Permeability (mD)	Porosity (%)
30-60 / 30-60 (AA)	1268.03	36.14
90-150 / 90-150 (BB)	2536.06	39.03
425-600 / 425-600 (CC)	4347.53	29.02
30-60 / 90-150 (AB)	380.40	29.75

In this research, mixture of two mesh sizes 30-60 / 90-150 was used throughout the core displacement tests due to the good porosity and permeability range, which are approximately similar to that of Arabian oil reservoirs of our interest.

4.4 Core Displacement Tests

There are two strategies applied in the core displacement tests to identify the role of few parameters in improving oil production, which are:

1. Injection of SDS solution, ZnO nanofluid and Al₂O₃ nanofluid in the absence of electromagnetic waves to observe the role of nanoparticles alone in recovering more oil.
2. Injection of ZnO nanofluid and Al₂O₃ nanofluid in the presence of electromagnetic waves to investigate the role of electromagnetic waves in activating the dielectric properties of both nanoparticles.

4.4.1 Effect of nanoparticles addition into the base fluid

In a series of core displacement tests, the performance of both type of nanofluids were evaluated. In the first experiment, brine was injected continuously at a rate of 2 ml/min during water flooding stage, followed by the 2 pore volume (PV) injection of the base fluid, 0.3 wt% SDS, which serves as the controlled experiment. In other experiments, the same amount of nanofluids was injected and their performances were compared. As shown in Figure 4.15, the incremental recovery curves for SDS and ZnO injection resembled similarities between them in terms of patterns although 26.4% more residual oil in place, ROIP was recovered with ZnO.

After 0.6 PV of SDS injections, oil production was declining and plateau region observed on the curve after 0.8 PV and beyond indicates that no more oil could be displaced. With ZnO nanofluid injection, a steady increase in the oil production was observed until 0.8 PV and shows a sudden decline in the production before reaching plateau beyond 1.0 PV injection.

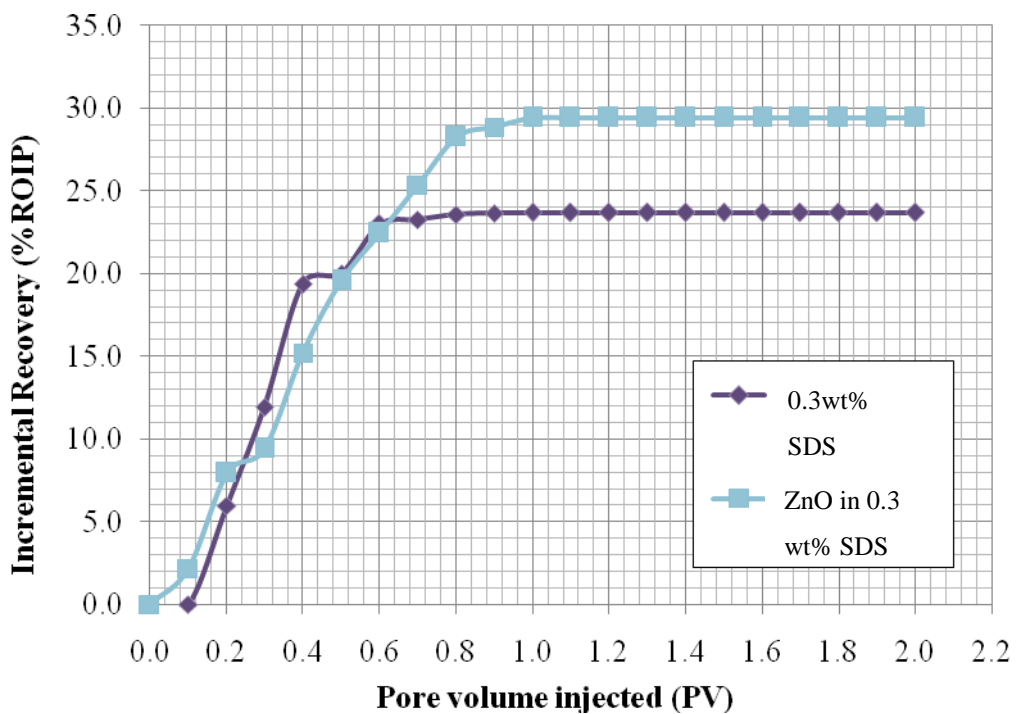


Figure 4.15: Comparison of the incremental recovery versus pore volume injected of the base fluid and ZnO nanofluid

However, dissimilar pattern was observed for Al_2O_3 nanofluid injection with slower increment of oil being displaced after each 0.1 PV of fluid injected, as plotted in Figure 4.16. Even though the rate of oil production is slower than the other two fluids, production of oil was continuously observed before it begins to decline after 1.8 PV of fluid injection. Due to this condition, the injection was prolonged and stopped at 2.5 PV since oil production remains stagnant after 2.1 PV.

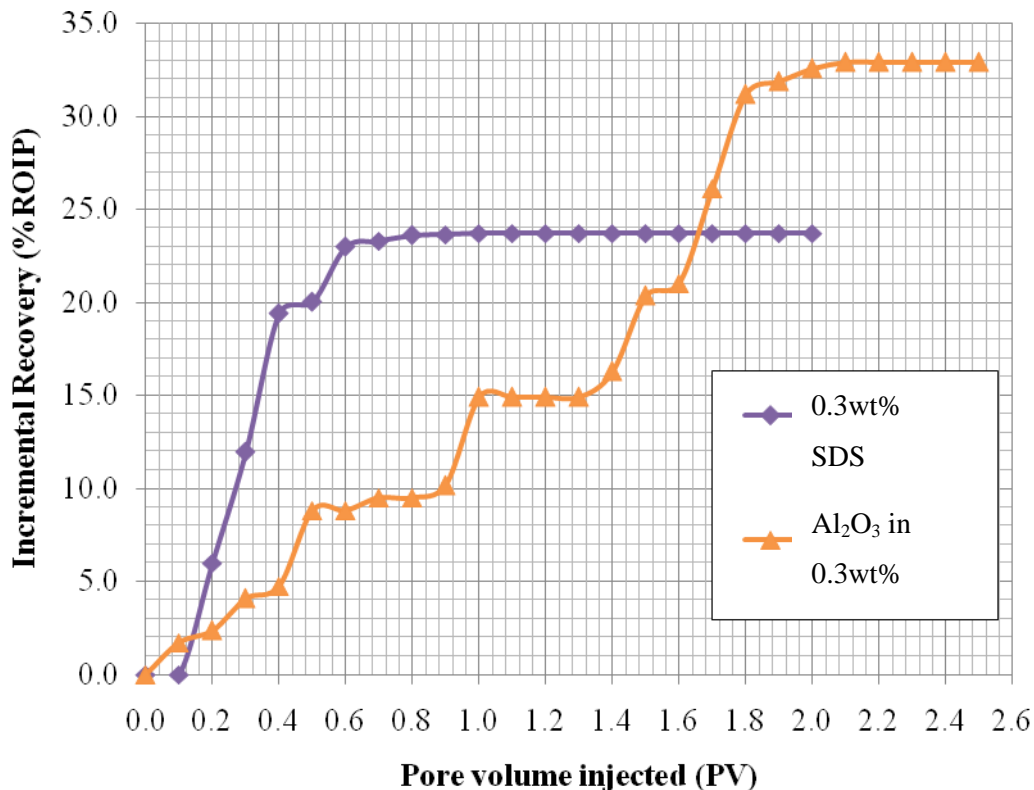


Figure 4.16: Comparison of the incremental recovery versus pore volume injected of the base fluid and Al_2O_3 nanofluid

In comparison, Al_2O_3 nanofluid injection gives the highest recovery of 32.88% ROIP, which is 11.8% more oil recovered compared to that of ZnO nanofluid and 41.2% more oil recovered in comparison with the SDS injection, as clearly depicted in Figure 4.17. To explain the increase in the recovery efficiency of both nanofluids as compared to aqueous SDS solution, it could be correlated with the viscosity increase in the injection fluids in the presence of nanoparticles. Although SDS reduces the IFT of water and oil, this reduction is not large enough to cause significant oil dispersion in the fluid. Even though the IFT values become slightly higher with the presence of

nanoparticles, tiny globules of oil are formed and are better dispersed in the mixture of nanofluid, brine and oil [44].

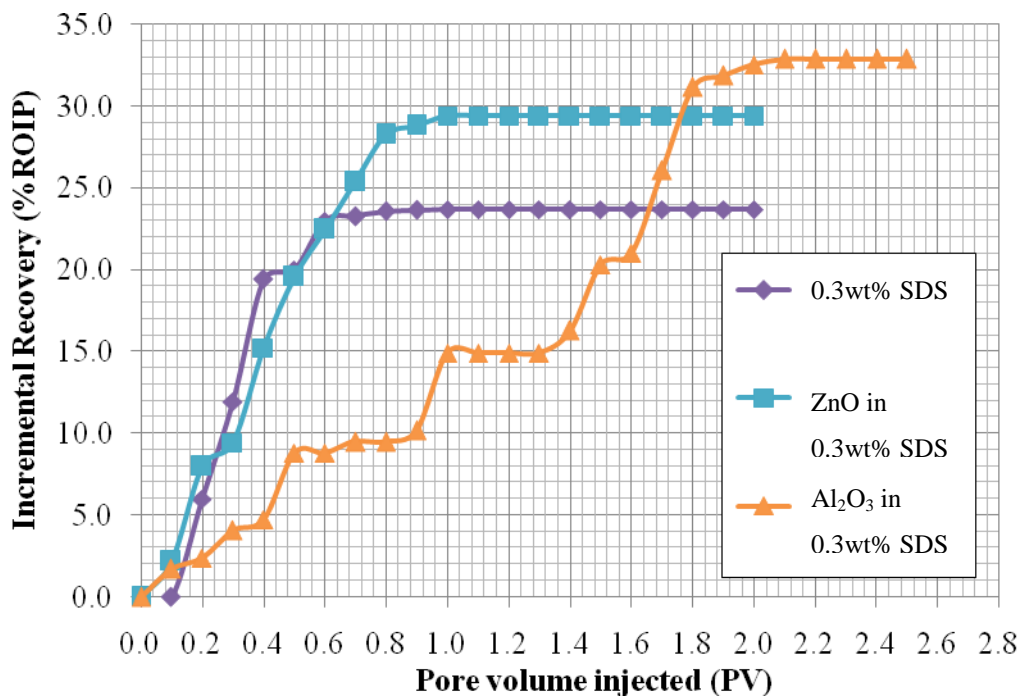


Figure 4.17: Comparison of the incremental recovery versus pore volume injected in the absence of EM waves for all injection fluids

4.4.2 Effect of EM irradiation on the recovery efficiency

Irradiation of EM waves on the porous medium during nanofluid injection shown a dramatic increase in the amount of oil recovered, as shown in Figure 4.18 and 4.19. In the case of ZnO nanofluid injection as shown in Figure 4.18, 63.9% ROIP more oil was recovered in the presence of 59.96 MHz of EM waves, as compared to the recovery in the case of absence.

Similar trend was observed during Al₂O₃ nanofluid injection, where 54.2% ROIP was successfully recovered when subjected in EM field, as depicted in Figure 4.19. In contrast, only 5.12% more ROIP recovered in Al₂O₃ nanofluid injection when compared with ZnO nanofluid in the presence of EM wave, as presented in Figure 4.20

It can be concluded that higher recovery observed was due to the change in the apparent viscosity of the nanofluid when subjected in EM field. In EM field, dielectric particles undergo polarization which in turn creates electric dipoles caused by the separation of positive and negative charges. These dipoles will make alignment with the applied field and as a result, creates a temporary chain-like structure which contributes to the increase in apparent viscosity of the nanofluid [95].

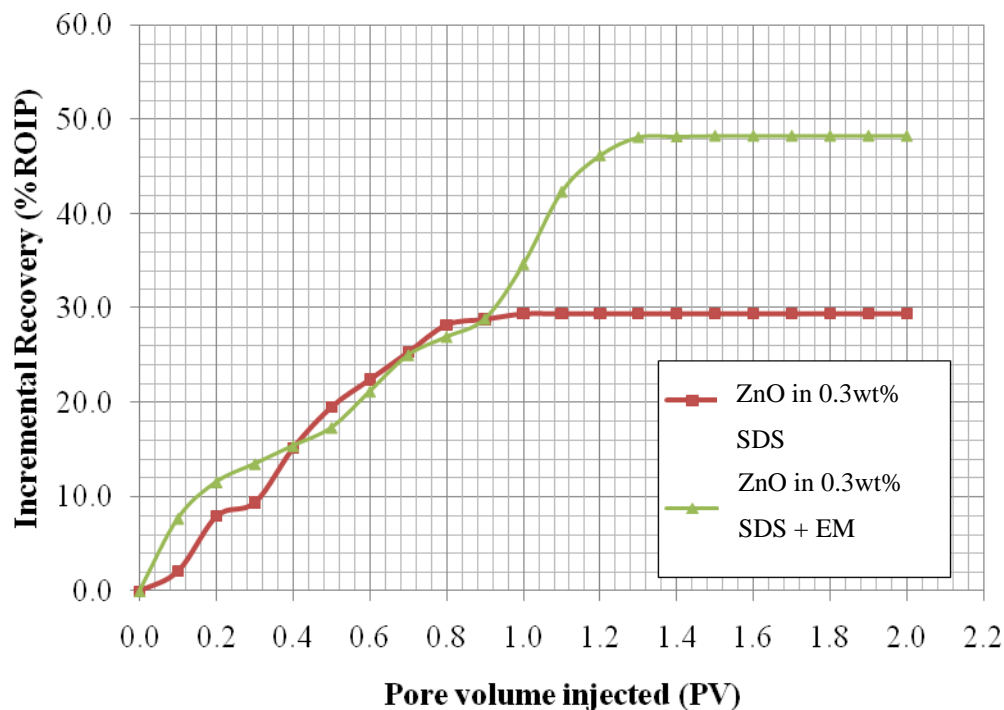


Figure 4.18: Comparison of the incremental recovery versus pore volume of ZnO nanofluid injected in the presence of EM waves

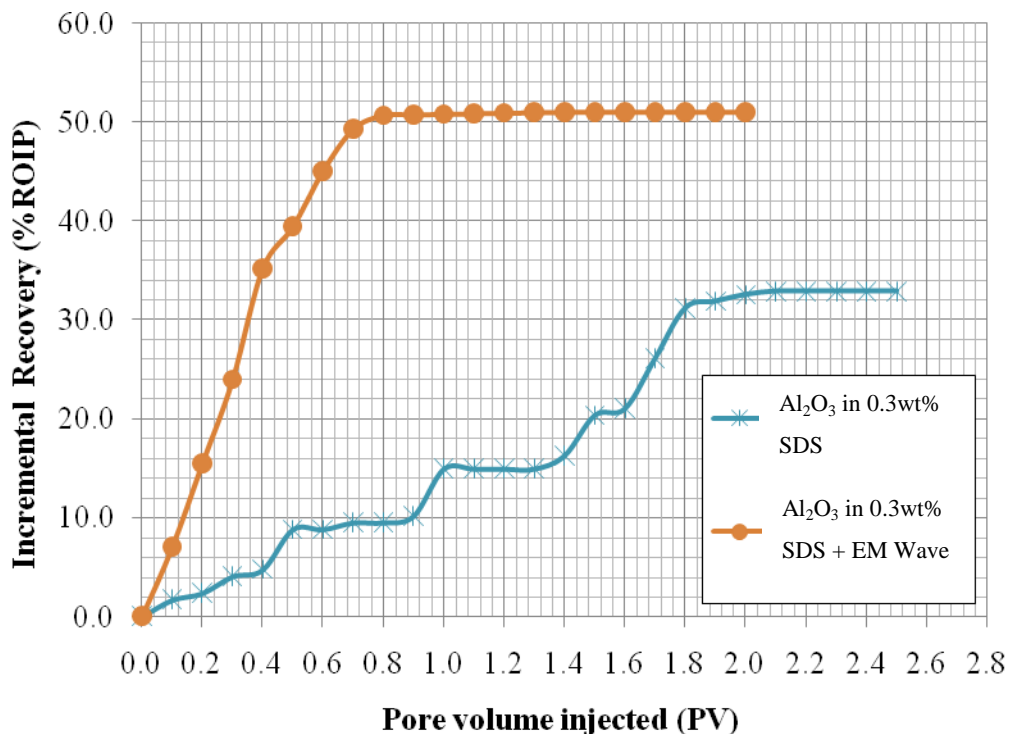


Figure 4.19: Comparison of the incremental recovery versus pore volume of Al₂O₃ nanofluid injected in the presence of electromagnetic wave

To explain the higher recovery efficiency observed in Al₂O₃ nanofluid injection in comparison with ZnO nanofluid in the presence of electromagnetic waves, it can be correlates to their dielectric properties. From the dielectric loss study of both nanofluids, Al₂O₃ nanofluid has 45.3% higher dielectric losses than that of ZnO due to the processes of polarization, re-orientation and conduction when electric field is applied. This may be attributed to the extrinsic crystal structure defects of the material e.g. porosity, crystallite orientation, etc, which was clearly observable from the FESEM, XRD and EDX analysis. Since Al₂O₃ has higher loss tangent compared to ZnO, it implies that higher interfacial polarization will occur in Al₂O₃ nanofluid when electromagnetic field is applied.

In the frequency range of 100 Hz to 4 MHz, Al₂O₃ nanofluid is expected to yield higher oil recovery efficiency due to the higher dielectric losses it has, in comparison to the ZnO (refer to Figure 4.11), which indicates more charges bound at the surface

and hence, more interfacial polarization will occur for effective viscosity enhancement, as a result of electro rheological (ER) effect.

Therefore, better sweep efficiency can be achieved with the increase in apparent viscosity, as in the case of polymer flooding. Addition of nanoparticles could increase the viscosity of water; therefore water-oil mobility ratio could be minimized to achieve better sweep efficiency. Furthermore, it has been widely presumed that with the reduction in the mobility ratio, shorter time will be needed to reach residual oil saturation, which was clearly observed during Al_2O_3 nanofluid injection, which is clearly depicted in Figure 4.19 [96].

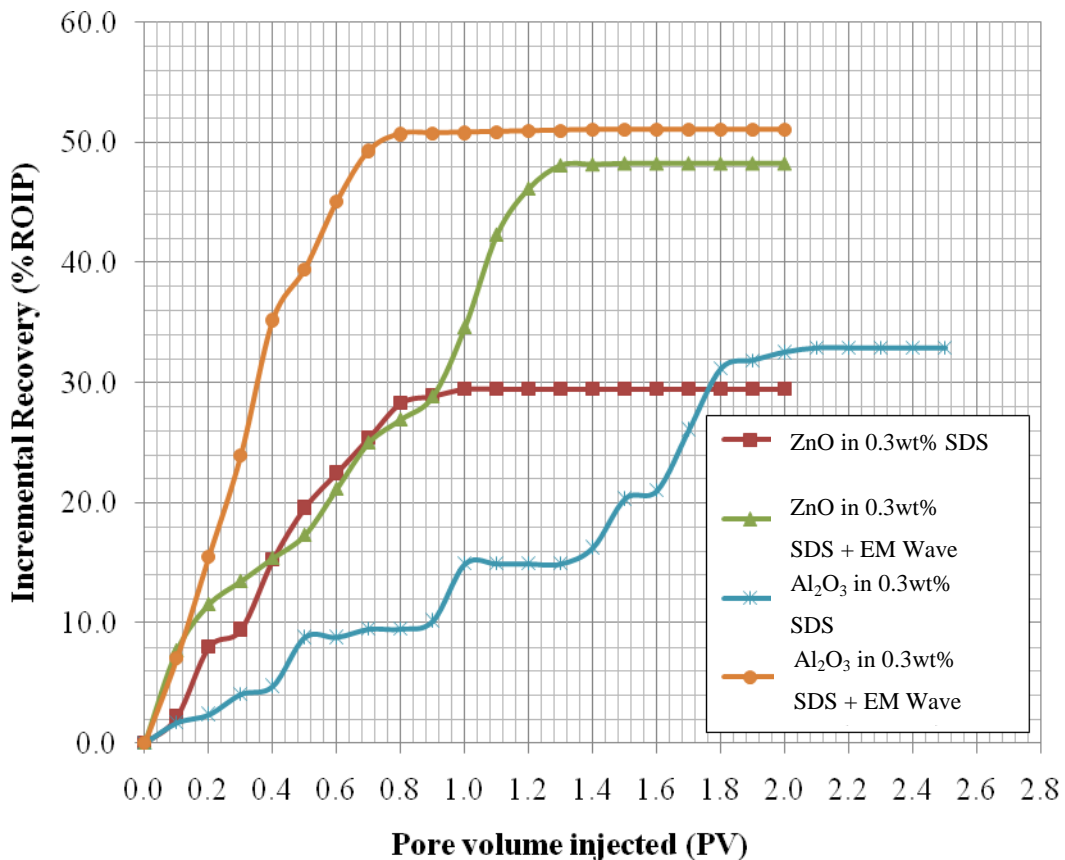


Figure 4.20: Comparison of the incremental recovery versus pore volume of both types of nanofluids injected in the presence/absence of EM waves

During core flooding experiments, few observations have been done on the effluent collected at the outlet, as shown in Figure 4.21. Initially, only clear pink

solution of brine is displaced when 0.1-0.2 PV of nanofluid is injected. This mark the process of mobilization of dispersed oil ganglion to form connections between other oil ganglions and become a large oil bank. However, when the fluid injection is continued, continuous oil drops flow through the outlet for the next 0.5 to 0.7 PV.

Beyond those injection volumes, mixtures of oil, brine and nanofluid started to be produced in the form of cloudy, opaque brown solution which came out from the outlet mostly after 0.5 PV of the injection fluids are injected through the inlet. The cloudy solution was found to be as macro emulsion, which is formation of tiny droplets of oil in aqueous phase due to a reduction in IFT between oil and water by the presence of surfactant (SDS) in the base fluid [21].

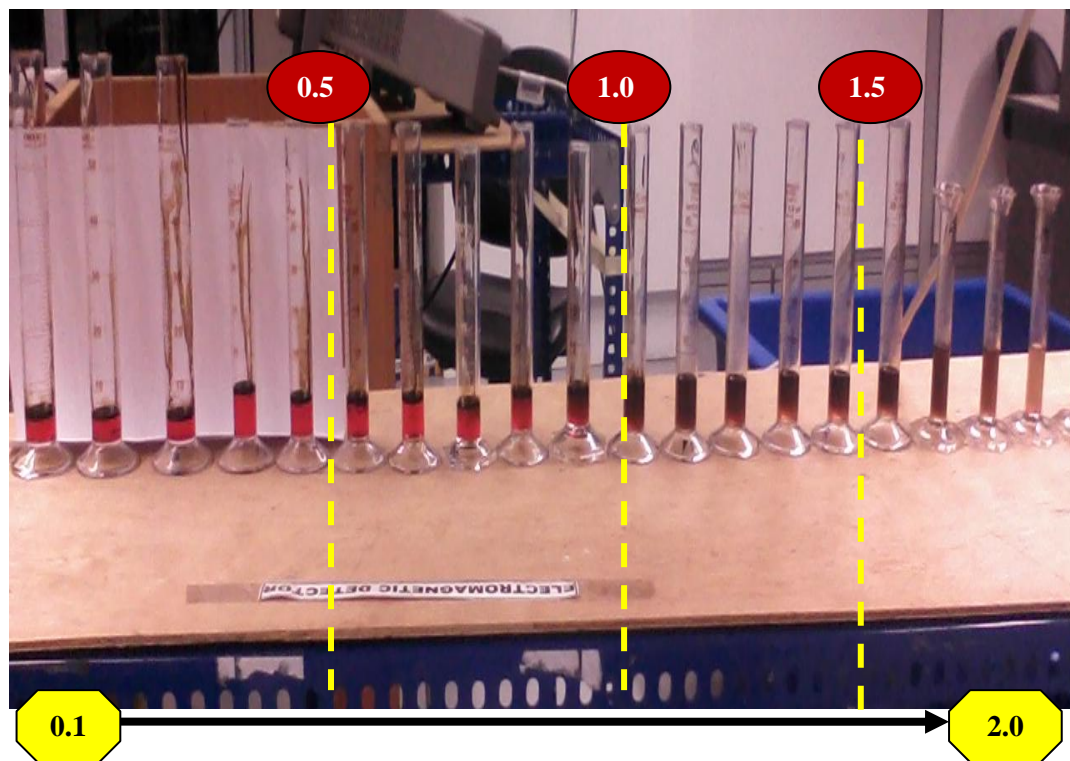


Figure 4.21: Effluent collected at the outlet during EOR fluid injections, from 0.1 until 2.0 pore volumes

After water flooding, disconnected oil ganglia left behind a flood front and dispersed in the swept zones. Therefore, an EOR agent is needed to connect these oil ganglia and mobilized them to flow. As the nanofluids interact with the formation, two processes are expected to occur. First, low concentration of SDS present in the

base fluid reduces the IFT between oil and water, therefore induced coalescence between previously dispersed oil ganglia. Subsequently, formation of emulsion increases the viscosity of the flood front and also viscosity of the nanofluids are found to be higher than brine, thus sweep efficiency is improved and results in higher residual oil recovery.

Although SDS reduces the IFT of water and oil, this reduction is not large enough to cause significant oil dispersion in the fluid. Even though the IFT values become slightly higher with the presence of nanoparticles, tiny globules of oil are formed and are better dispersed in the mixture of nanofluid, brine and oil [44]. Summary of the recovery efficiency obtained from all injection fluids after 2 PV of injection in the absence and presence of EM wave is gathered in Table 4.9.

4.4.3 Pressure drop as an indication of viscosity change

Figure 4.22 until 4.25 exhibit the relationship between incremental oil recovery and pressure drop for both type of nanofluids flooding in the absence and presence of EM wave irradiation. Pressure drop was found to be higher during nanofluid flooding due to the high viscosity emulsion generated in-situ, as well as the nature of nanofluids having viscosities higher than brine and SDS solution. Interaction between oil, SDS and nanofluid solutions create in-situ emulsification and hence, increase resistance to water flow and oil recovery as well, which resulted from the improved sweep efficiency [97].

As shown in Table 4.10, an obvious discrepancy was found in the experimentally measured pressure drop for nanofluid flooding, especially when EM wave was irradiated to the porous medium. When the viscosity of the displacing fluid is empirically determined from the instantaneous pressure drop reading, an unreasonable value of the viscosity of fluid/emulsion formed was deduced, in agreement to similar observation done by Arhuoma et al (2009), for all core displacement tests [97]. In the presence of EM wave irradiation after 0.8 PV injection of Al_2O_3 nanofluid (Figure 4.22 and 4.23), pressure drop was found to be 29.7 psi, corresponds to 109.98% increase in the viscosity of the displacing fluid in comparison to the

viscosity calculated in the absence of EM irradiation. Due to this viscosity contrast, higher recovery was achieved in the presence of EM irradiation.

Similar trend was observed after 0.8 PV injection of ZnO nanofluid as shown in Figure 4.24 and 4.25, with 140.41% increase in the viscosity of the displacing fluid when irradiated with EM wave at pressure drop of 24.6 psi. Explanation to this could be done by recalling the idea of ER effect to change viscosity of dielectric suspensions in applied electric field. Physically after water flooding, flows of nanofluid in the porous medium through water channels create interaction with oil and therefore produce in-situ emulsion. This emulsion has a higher viscosity and tends divert the flow to unswept region by blocking high permeability zone. As a result, the built-up pressure is gradually increased due to effective blockage of the water channel, and sharply decreased when the differential pressure overcomes the capillary forces and the viscous forces imposed by the nanofluids and in-situ emulsion [98].

Table 4.9: Petrophysical Characterization and Recovery Evaluation

EOR Injection fluid	SDS	NanoZnO	NanoZnO	NanoAl₂O₃	NanoAl₂O₃
EM Wave Irradiation (59.96 MHz)			Yes		Yes
Parameters*					
Dry weight (g)	1248.40	1264.42	1274.91	1264.56	1269.10
Wet Weight (g)	1318.80	1331.98	1344.84	1330.06	1333.60
Weight difference	70.40	67.56	69.93	65.50	64.50
Density of brine (g/cm ³)	1.02	1.02	1.02	1.02	1.02
Bulk volume, BV (cm ³)	233.88	233.88	249.787	233.88	233.88
Pore volume, PV (cm ³)	69.02	66.24	68.56	64.22	63.24
Porosity, PV/BV (%)	29.51	28.32	27.45	27.46	27.04
Permeability (mD)	157.43	169.78	169.24	107.79	113.18
Original Oil In Place, OOIP (ml)	65.00	65.00	62.00	60.50	61.75
Initial water saturation	0.058	0.019	0.096	0.058	0.023
Recovery by Water flooding (ml)	48.25	47.75	49.00	45.75	44.00
E _R by WF (%OOIP)	74.23	75.00	79.03	75.62	71.26
Residual Oil in Place, ROIP (ml)	16.75	17.25	13.00	14.75	17.75
Volume recovered in EOR stage (ml)	3.97	5.08	6.27	4.85	9.00
Recovery Efficiency, E_R (%ROIP)	23.70	29.42	48.23	32.88	50.70

*Note: Derivation and calculation of quantities listed in Table 4.9 could be found in Appendix D.

Table 4.10: Relationship between incremental oil recovery with the pressure drop

PV Injected	Alumina			Alumina EM			ZnO			ZnO EM		
	Pressure drop (psi)	Viscosity (cP)	Incremental Recovery (%ROIP)	Pressure drop (psi)	Viscosity (cP)	Incremental Recovery (%ROIP)	Pressure drop (psi)	Viscosity (cP)	Incremental Recovery (%ROIP)	Pressure drop (psi)	Viscosity (cP)	Incremental Recovery (%ROIP)
0.1	8.4	29.40	1.01	30.0	73.5	7.04	15.90	58.43	2.17	28.9	105.87	7.69
0.2	8.9	31.15	1.41	31.7	77.7	15.49	12.00	44.10	7.97	21.4	78.40	11.54
0.3	9.2	32.20	2.42	29.5	72.3	23.94	14.10	51.82	9.42	24.1	88.29	13.46
0.4	9.6	33.60	2.83	28.5	69.8	35.21	14.10	51.82	15.22	24.5	89.75	15.38
0.5	9.3	32.55	5.25	29.8	73.0	39.44	13.60	49.98	19.57	24.2	88.65	17.31
0.6	10	35.00	5.25	29.6	72.5	45.07	9.90	36.38	22.46	24.5	89.75	21.15
0.7	9.8	34.30	5.66	29.4	72.0	49.30	8.60	31.61	25.36	24.6	90.12	25.00
0.8	9.9	34.65	5.66	29.7	72.8	50.70	10.20	37.49	28.26	24.6	90.12	26.92
0.9	10.3	36.05	6.06	29.9	73.3	50.76	12.10	44.47	28.84	24.9	91.22	28.85
1.0	10.6	37.10	8.89	29.4	72.0	50.82	12.70	46.67	29.42	24.5	89.75	34.62
1.1	10.9	38.15	8.89	29.5	72.3	50.87	12.90	47.41	29.42	23.9	87.56	42.31
1.2	10.7	37.45	8.89	29.1	71.3	50.93	13.40	49.25	29.42	23.9	87.56	46.15
1.3	11.2	39.20	8.89	28.9	70.8	50.99	14.00	51.45	29.42	23.9	87.56	48.08
1.4	11.1	38.85	9.70	27.8	68.1	51.04	14.50	53.29	29.42	24.6	90.12	48.15
1.5	11.6	40.60	12.12	27.0	66.1	51.04	15.00	55.13	29.42	24.5	89.75	48.23
1.6	11.6	40.60	12.53	26.5	64.9	51.04	14.90	54.76	29.42	26.0	95.25	48.23
1.7	11.6	40.60	15.56	26.4	64.7	51.04	15.40	56.60	29.42	26.5	97.08	48.23
1.8	12.5	43.75	18.59	24.1	59.0	51.04	16.30	59.90	29.42	26.9	98.55	48.23
1.9	11.6	40.60	18.99	25.9	63.5	51.04	16.80	61.74	29.42	27.1	99.28	48.23
2.0	11.8	41.30	19.39	23.3	57.1	51.04	17.60	64.68	29.42	27.1	99.28	48.23

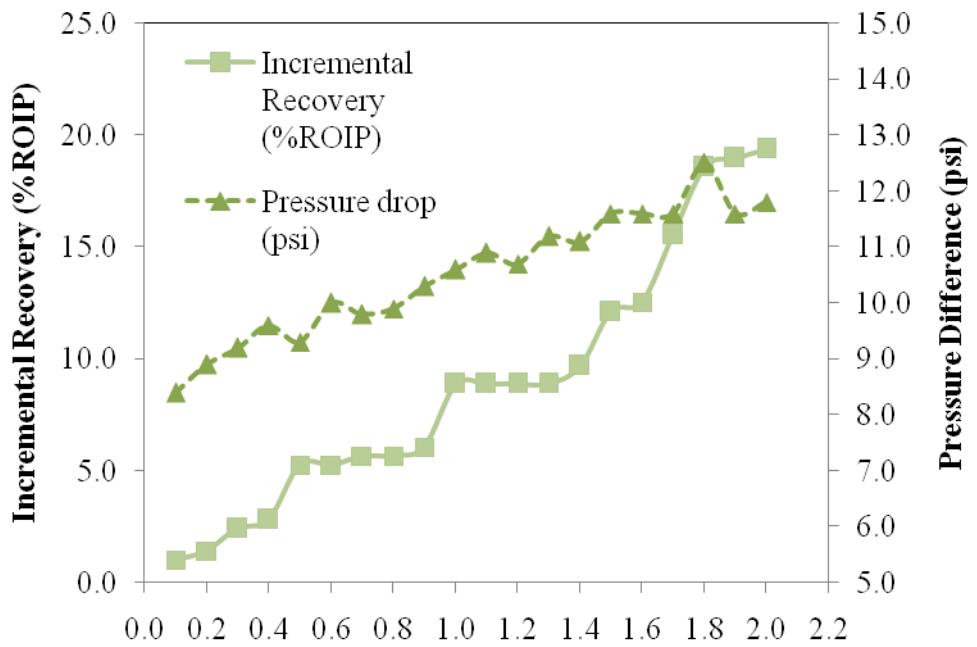


Figure 4.22: Incremental oil recovery and pressure difference for 2 PV injection of Al_2O_3 nanofluid

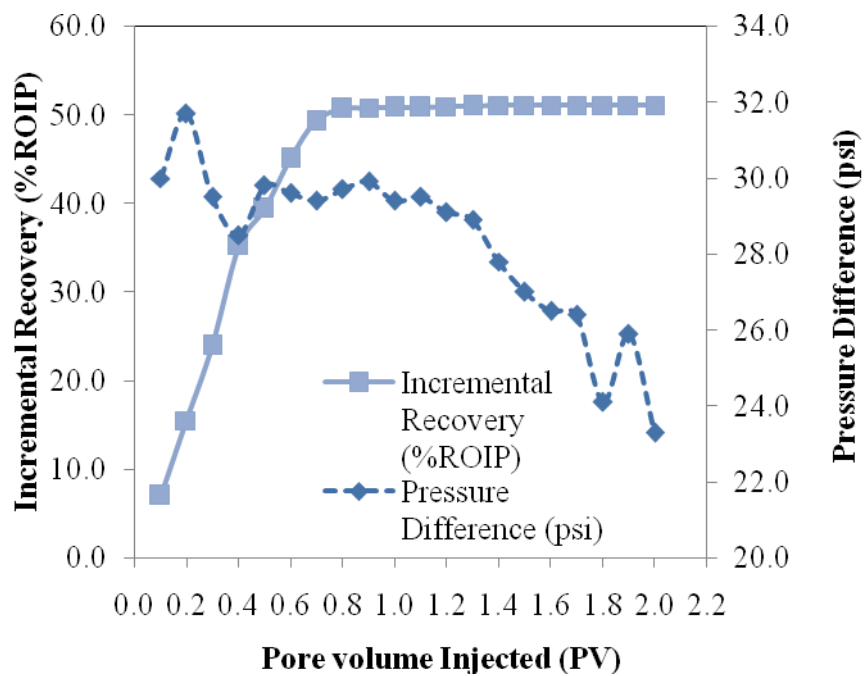


Figure 4.23: Incremental oil recovery and pressure difference for 2 PV injection of Al_2O_3 nanofluid in the presence of EM irradiation

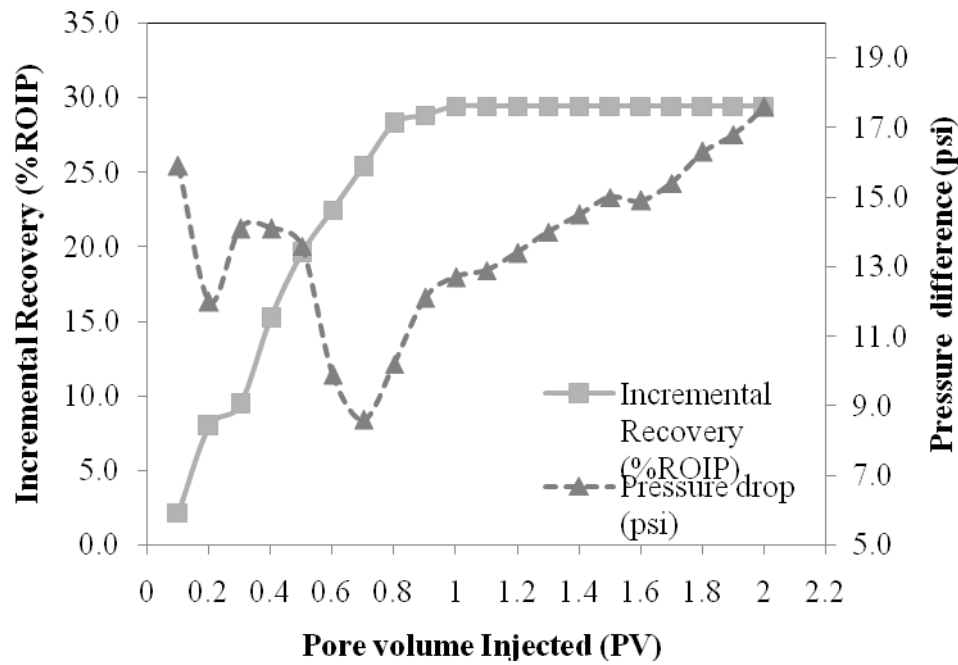


Figure 4.24: Incremental oil recovery and pressure difference for 2 PV injection of ZnO nanofluid

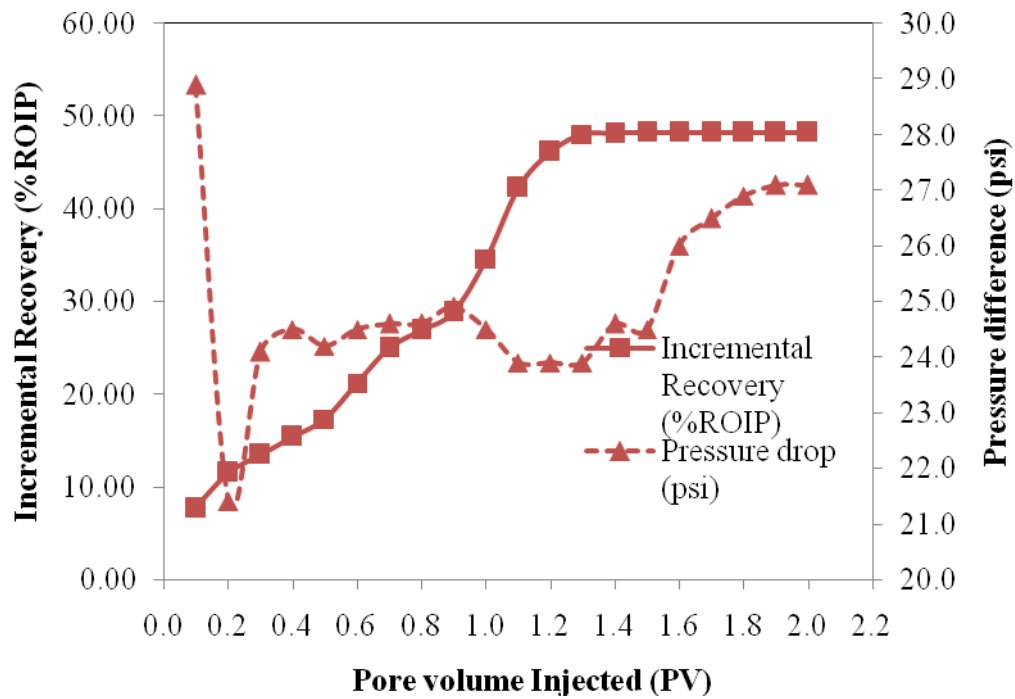


Figure 4.25: Incremental oil recovery and pressure difference for 2 PV injection of ZnO nanofluid in the presence of EM irradiation

CHAPTER 5

CONCLUSIONS

5.1 Conclusion

It is proven that electromagnetically stimulated dielectric nanoparticles can recover oil from an oil reservoir by:

1. Successfully synthesized single phase, high crystallinity hexagonal Al_2O_3 and ZnO nanoparticles having average crystallite size of around 38 nm and 45 nm, with impurities levels below 15%, at temperature 1100°C and 300°C , respectively.
2. At the lowest measurable frequency, 10^2 Hz, dielectric loss of Al_2O_3 is 2.60×10^5 , which is 45.3% higher than that of ZnO at the same frequency. From dielectric loss factor spectra, it is shown that Al_2O_3 has higher dielectric losses in the frequency range of 10^2 - 10^5 Hz in comparison to the ZnO , which indicates more charges bounded at the surface, rendering it to be more surface active for greater interfacial polarization.
3. By conducting core flooding tests;
 - a. Highest recovery by nanofluid flooding itself was achieved in Al_2O_3 nanofluid injection with 32.88% ROIP, which is 11.8% more oil recovered, compared to that of ZnO nanofluid.
 - b. By injecting Al_2O_3 nanofluid in the presence of EM wave, 54.2% ROIP was successfully recovered, giving 5.12% more oil recovered compared to ZnO nanofluid.

5.2 Recommendation

Up to this point, this novel EOR method has been successfully demonstrated and yield promising results for further development. In order to ensure the success and feasibility of this method before field or pilot test could be deployed, few recommendations for the future work are being outlined as follows:

- 1. Stability of nanoparticles suspension in harsh environments:**

In future, a quantitative measurement on the stability of nanoparticles suspension, as well as including the effect of temperature and/or pressure on the stability should be conducted. The choice of additives and surface coating techniques to improve suspension stability would be significant for future studies. as well as their stability in elevated temperature.

- 2. Feasibility in HTHP environment:**

Core displacement tests should be conducted in a high temperature, high pressure (HTHP) cell or a confined system to confirm the applicability of this novel method in the highly pressurized, elevated temperature of extreme oil reservoirs.

- 3. Optimization of various parameters:**

Parameters e.g. nanofluid concentration, EM wave frequency, as well as type and morphology of nanoparticles should be optimized by means of intensive lab works, computer simulation and modelling using software e.g. ECLIPSE 100 & 300, Finite Element Time Domain (FDTD), MATLAB, Computer Simulation Technology (CST) and COMSOL, to name a few.

5.3 Main Contribution

- 1. Application of aluminum oxide nanoparticles in EOR stage has produced 31.3% more oil in comparison with SDS (conventional EOR method).**
- 2. With irradiation of 59.96 MHz, 81.7% more oil was produced in comparison with the oil recovered in the absence of EM irradiation.**

5.4 List of Publications

1. **Ahmad Latiff, N. R.**, Mohd Zaid, H., Yahya, N., & Demiral, B. (2011). Novel enhanced oil recovery method using dielectric zinc oxide nanoparticles activated by electromagnetic waves. National Postgraduate Conference (NPC) (pp. 1-7). Tronoh, Malaysia: IEEE Conference Publications.
2. **Ahmad Latiff, N. R.**, Mohd Zaid, H., Yahya, N., & Demiral, B. (2012). The Effect of IFT and Viscosity of the Nanofluids in Electromagnetically Stimulated Dielectric Nanofluid Flooding. International Conference on Integrated Petroleum Engineering and Geosciences (ICIPEG), Kuala Lumpur.
3. Mohd Zaid, H., **Ahmad Latiff, N. R.**, Yahya, N., & Demiral, B. (2012). Synthesis and Characterization of Dielectric Nanoparticles for Application in Enhanced Oil Recovery. International Conference on Fundamental and Applied Sciences (ICFAS), Kuala Lumpur.
4. Mohd Zaid, H., **Ahmad Latiff, N. R.**, Yahya, N., & Demiral, B. (2012). The Effect of Nanoparticles Crystallite Size on the Recovery Efficiency in Dielectric Nanofluid Flooding. 8th International Conference on Diffusion Solids and Liquids (DSL). Istanbul, Turkey.

REFERENCES

1. Sovacool, B. K. (2007). Solving the oil independence problem: Is it possible?. *Energy Policy, 35(11)*, 5505–5514.
2. Askari, H., & Krichene, N. (2010). An oil demand and supply model incorporating monetary policy. *Energy, 35(7)*, 2013–2021.
3. Aleklett, K., Hook, M. & Jakobsson, K. (2010). The Peak of the Oil Age – Analyzing The World Oil Production Reference Scenario in World Energy Outlook 2008. *Energy Policy, 38(3)*, 1398–1414.
4. Kjarstad, J. & Johnsson, F. (2009). Resources and future supply of oil. *Energy Policy, 37(2)*, 441–464.
5. Lakatos, I, & Szabó, J. L. (2009, June 8-11). *Role of conventional and unconventional hydrocarbons in the 21st century: Comparison of resources, reserves, recovery factors and technologies*. Paper presented at the SPE/EUROPEC/EAGE Annual Conference and Exhibition, Amsterdam, The Netherlands.
6. Nares, H. R., Schacht-Hernández, P., Ramírez-Garnica, M. A., Cabrera-Reyes, M. C. & Noé-Valencia, L. (2007, April 15-18). *Heavy crude oil upgrading with transition metals*. Paper presented at the SPE Latin American & Caribbean Petroleum Engineering Conference, Buenos Aires, Argentina.
7. Wever, D.A.Z., Picchioni, F. & Broekhuis, A.A. (2011). Polymers for enhanced oil recovery: A paradigm for structure–property relationship in aqueous solution. *Progress in Polymer Science,36(11)*, 1558-1628.
8. Sandrea, I. & Sandrea, R (2007). Global Oil Reserves – Recovery Factors Leave Vast Target for EOR Technologies. *Oil and Gas Journal, 105(41)*, 44-48.
9. Mai, A. & Kantzas, A. (2007). Heavy Oil Waterflooding: Effects of Flow Rate and Oil Viscosity. *Journal of Canadian Petroleum Technology, 48(3)*, 42-51.

10. Aladasani, A. & Bai, B. (2010, June 8-10). *Recent Developments and Updated Screening Criteria of Enhanced Oil Recovery Techniques*. Paper presented at the International Oil and Gas Conference and Exhibition China, Beijing, China.
11. Taber, J. J., Martin, F. D., & Seright, R. S. (1997). EOR Screening Criteria Revisited - Part 1: Introduction to Screening Criteria and Enhanced Recovery Field Projects. *SPE Reservoir Engineering*, 12(3), 189-198.
12. Chakma, A., & Jha, K. N. (1992, October 4-7). *Heavy Oil Recovery From Thin Pay Zones by Electromagnetic Heating*. Paper presented at SPE Annual Technical Conference and Exhibition, Washington, D.C.
13. Fanchi, J. R. (1990, September 23-26). *Feasibility of Reservoir Heating by Electromagnetic Irradiation*. Paper presented at the SPE Annual Technical Conference and Exhibition, New Orleans, Louisiana.
14. Kulawardana, E. U., Koh, H., Kim D. H., Liyanage, P. J., Upamali, K. A. N., Huh,C., Weerasooriya, U., & Pope, G. A. (2012, April 14-18). *Rheology and Transport of Improved EOR Polymers under Harsh Reservoir Conditions*. Paper presented at the SPE Improved Oil Recovery Symposium, Tulsa, Oklahoma, USA.
15. Seright, R.S., Campbell, A.R., Mozley, P.S., and Han, P. (2010). Stability of Partially Hydrolyzed Polyacrylamides at Elevated Temperatures in the Absence of Divalent Cations. *SPE Journals*, 15(2), 341-348.
16. Dang, Z., Fan, L., Zhao, S., Nan, C. (2003). Dielectric properties and morphologies of composites filled with whisker and nanosized zinc oxide. *Materials Research Bulletin*, 38(3), 499–507.
17. Huang, C. L., Wang, J. J., Huang, C. Y. (2005). Sintering behavior and microwave dielectric properties of nano alpha-alumina. *Materials Letters*, 59(28), 3746–3749.
18. Sun, Z. X., Zheng, T. T., Bo, Q. B., Du, M., Forsling, W. (2008). Effects of

- calcination temperature on the pore size and wall crystalline structure of mesoporous alumina. *Journal of Colloid and Interface Science* 319, 247–251.
19. Vafaee, M., Ghamsari, M. S. (2007). Preparation and characterization of ZnO nanoparticles by a novel sol-gel route. *Materials Letters*, 61(14–15), 3265–3268.
 20. Davis, J. P. & Fletcher, A. J. P. (2010, April 24-28). *How EOR Can Be Transform by Nanotechnology*. Paper presented at the SPE Improved Oil Recovery Symposium, Tulsa, Oklahoma, USA.
 21. Pillai, V., Kanicky, J. R. & Shah, D. O. (1999). Applications of Microemulsions in Enhanced Oil Recovery. In P. Kumar and K. L. Mittal (Eds.), *Handbook of Microemulsion Science and Technology* (743-754). New York : Marcel Dekker Inc.
 22. Iglauer, S., Wu, Y., Shuler, P., & Tang, Y. (2010). New surfactant classes for enhanced oil recovery and their tertiary oil recovery potential. *Journal of Petroleum Science and Engineering* 71(1-2), 23–29.
 23. Dong, M., Zhang, H., & Zhao, S. (2010). Which One is More Important in Chemical Flooding for Enhanced Court Heavy Oil Recovery, Lowering Interfacial Tension or Reducing Water Mobility?. *Energy Fuels*, 24(3), 1829-1836.
 24. Hirasaki, G.J., Miller, C.A., & Puerto, M. (2011). Recent Advances in Surfactant EOR. *SPE Journals*, 16 (4), 889-907.
 25. Samanta, A., Ojha, K., Sarkar, A., & Mandal, A. (2011). Surfactant and Surfactant-Polymer Flooding for Enhanced Oil Recovery. *Advances in Petroleum Exploration and Development*, 2(1), 13-18.
 26. Chiang, M. Y., Chan, K. S., & Shah, D. O. (1978). A correlation of interfacial charge with various interfacial properties in relation to oil recovery efficiency during waterflooding. *Journal of Canadian Petroleum Technology*, 17(4).

27. Bansal, V. K., et al. (1978). The Effect Of Caustic Concentration On Interfacial Charge, Interfacial Tension And Droplet Size: A Simple Test For Optimum Caustic Concentration For Crude Oils, *Journal of Canadian Petroleum Technology* 17(1).
28. Roosta, A. et. al (2009, March 15-18). *Investigating the mechanism of thermally induced wettability alteration*, Paper presented at the SPE Middle East Oil and Gas Show and Conference, , Bahrain, Bahrain
29. Al-Hadhrami, H. S., & Blunt, M. J. (2001). Thermally Induced Wettability Alteration to Improve Oil Recovery in Fractured Reservoirs. *SPE Reservoir Evaluation & Engineering*, 4(3), 179-186.
30. Rao, D. N. (1999). Wettability Effects in Thermal Recovery Operations.*SPE Reservoir Evaluation & Engineering*, 2(5), 420-430.
31. Schlumberger Oilfield Glossary. [Online] Schlumberger. [Cited: August 2, 2012.]
<http://www.glossary.oilfield.slb.com/Display.cfm?Term=sweep%20efficiency.11194>.
32. Chang, H. G. (2011, December 12-14). *Advances of Polymer Flood in Heavy Oil Recovery*. Paper presented at the SPE Heavy Oil Conference and Exhibition, Kuwait City, Kuwait.
33. Wang, J., & Dong, M. (2007, Jun 12 - 14). *A Laboratory Study of Polymer Flooding for Improving Heavy Oil Recovery*. Paper presented at the Canadian International Petroleum Conference, Calgary, Alberta.
34. Study of Tertiary Oil Recovery by Surfactant/ Polymer Flooding. *Egypt Oil & Gas Web Portal*. [Online] [Cited: September 3, 2012.] http://www.egyptoil-gas.com/read_article_issues.php?AID=100.
35. Amanullah, M. & Al-Tahini, A. M. (2009, May 9-11). *Nano-Technology: Its Significance in Smart Fluid Development for Oil and Gas Field Application*.

Paper presented at the SPE Saudi Arabia Section Technical Symposium, Al-Khobar, Saudi Arabia.

36. Ayatollahi, S. & Zerafat, M. M. (2012, June 12-14). *Nanotechnology-Assisted EOR Techniques: New Solutions to Old Challenges*. Paper presented at the SPE International Oilfield Nanotechnology Conference, Noordwijk, The Netherlands.
37. Binks, B. P. (2002). Particles and Surfactants – Similarities and Differences. *Current Opinion in Colloid and Interface Sciences*, 7(1-2), 21–41.
38. Hao, T. (2002). Electrorheological suspensions. *Advances in Colloid and Interface Science*, 97(1–3), 1–35.
39. Ahmad Latiff, N. R., Mohd Zaid, H., Yahya, N., & Demiral, B. (2011, Sept 19-20). *Novel Enhanced Oil Recovery Method using Dielectric ZnO Nanoparticles Activated by Electromagnetic Waves*. Paper presented at the National Postgraduate Conference (NPC) 2011, Tronoh, Perak. Kuala Lumpur: IEEE Conference Proceedings.
- :40 Karimi, A., Fakhroueian, Z., Bahramian, A., Khiabani, N. P., Darabad, J. B., Azin, R., & Arya, S. (2012). Wettability Alteration in Carbonates using Zirconium Oxide Nanofluids: EOR Implications. *Energy Fuels*, 26 (2), 1028–1036.
41. Espinosa, D., Caldelas, F., Johnston, K., Bryant, S. L. & Huh, C. (2010, April 24-28). *Nanoparticle-Stabilized Supercritical CO₂ Foams for Potential Mobility Control Applications*. Paper presented at the SPE Improved Oil Recovery Symposium, Tulsa, Oklahoma, USA.
42. Suleimanov, B. A., Ismailov, F. S. & Veliyev, E. F. (2011). Nanofluid for enhanced oil recovery. *Journal of Petroleum Science and Engineering*, 78(2), 431-437.
43. Zitha, P. L. J. & Wessel, F. (2002, April 13-17). *Fluid Flow Control Using*

Magnetorheological Fluids. Paper presented at the SPE/DOE Improved Oil Recovery Symposium, Tulsa, Oklahoma.

44. Onyekonwu, M. O. & Ogolo, N. A. (2010, 31 July - 7 August 2010). *Investigating the Use of Nanoparticles in Enhancing Oil Recovery.* Paper presented at the Nigeria Annual International Conference and Exhibition, Tinapa - Calabar, Nigeria.
45. *CLU-IN - The Hazardous Waste Clean-up Information (CLU-IN).* [Online] July 28, 2001 . [Cited: May 11, 2012.] <http://www.clu-in.org/products/aatdf/chap4.htm>.
46. Zhang, T., Davidson, A., Bryant, S. L., & Huh, C. (2010, April 24-28), *Nanoparticle-stabilized emulsions for applications in enhanced oil recovery.* Paper presented at the SPE Improved Oil Recovery Symposium, Tulsa, Oklahoma, USA.
47. Wang, Y., Zhao, F., Bai, B., Zhang, J., Xiang, W., Li X & Zhou, W. (2010, April 24-28). *Optimized Surfactant IFT and Polymer Viscosity for Surfactant-Polymer Flooding in Heterogeneous Formations.* Paper presented at the SPE Improved Oil Recovery Symposium, Tulsa, Oklahoma, USA.
48. McElfresh, P., Wood, M., & Ector, D. (2012, June 12-14). *Stabilizing Nano Particle Dispersions in High Salinity, High Temperature Downhole Environment.* Paper presented at the SPE International Oilfield Nanotechnology Conference, Noordwijk, The Netherlands.
49. Huh, C., Lange, E.A., & Cannella, W.J. (1990, April 22-25). *Polymer Retention in Porous Media.* Paper presented at the SPE/DOE Enhanced Oil Recovery Symposium, Tulsa, Oklahoma.
50. Skauge, T., Spildo, K., & Skauge, A. (2010, April 24-28). *Nano-sized Particles for EOR.* Paper presented at the SPE Improved Oil Recovery Symposium, Tulsa, Oklahoma, USA.

51. Prodanovi, M., Ryoo, S., Rahmani, A. R., Kuranov, R., Kotsmar, C., Milner, T. E., Johnston, K. P., Bryant, S. L., & Huh, C. (2010, April 24-28). *Effects of Magnetic Field on the Motion of Multiphase Fluids Containing Paramagnetic Particles in Porous Media*. Paper presented at the SPE Improved Oil Recovery Symposium, Tulsa, Oklahoma, USA.
52. Hizem, M., Budan, H., Devillé, B., Faivre, O., Mossé, L., & Simon, M. (2008, September 21-24). *Dielectric Dispersion: A New Wireline Petrophysical Measurement*. Paper presented at the SPE Annual Technical Conference and Exhibition, Denver, Colorado, USA.
53. Shang, Y., Jia, Y., Liao, F., Li, J., Li, M., Wang, J., Zhang, S. (2007). Preparation, microstructure and electrorheological property of nano-sized TiO₂ particle materials doped with metal oxides. *Journal of Materials Science*, 42(8), 2586-2590.
54. Parthasarathy, M., Klingenberg, D. J. (1996). Electrorheology: Mechanisms and models. *Materials Science and Engineering: R: Reports* 17(2), 57–103.
55. Stangroom, J. E. (1983). Electrorheological fluids. Physics in Technology, 14(6), 290.
56. Zhou, W., Zhao. K. (2010). Confirmation of water mechanism in zeolite electrorheological fluid. *Journal of Non-Crystalline Solids*, 356, 1522–1525.
57. Yin, J., & Zhao, X. (2006). Titanate nano-whisker electrorheological fluid with high suspended stability and ER activity. *Nanotechnology*, 17, 192.
58. Feret, F. R., Daniel, R., & Clermont, B. (2000). Determination of alpha and beta alumina in ceramic alumina by X-ray diffraction. *Spectrochimica Acta Part B: Atomic Spectroscopy*, 55(7), 1051–1061.
59. Aryasomayajula, A. (2009). *Low temperature alpha alumina thin film coating for cutting tool application by AC inverted magnetron sputtering technique*.

Retrieved from Proquest LLC (AAT 1461445)

60. Tagliabue, M. et al. (2012). High pressure hydrogen sulphide adsorption on silica–aluminas. *Chemical Engineering Journal*, 210, 398–403.
61. Soo, C. L. , Yong, M. K. & Ho, J. C. (2013). Improving regeneration properties of potassium-based alumina sorbents for carbon dioxide capture from flue gas. *Fuel*, 104, 882–885.
62. Morkoç, H. & Özgur, U. (2009). *Zinc Oxide: Fundamentals, Materials and Device Technology*. Wiley-VCH Verlag GmbH & Co.
63. Pei, L. Z., Zhao, H. S., Tan, W., Yua, H. Y., Chen, Y. W., Zhang, Q. (2009). Single crystalline ZnO nanorods grown by a simple hydrothermal process. *Materials Characterization*, 60(9), 1063–1067.
64. Moezzi, A., McDonagh, A. M. & Cortie, M. B. (2012). Zinc oxide particles: Synthesis, properties and application. *Chemical Engineering Journal*, 185-186, 1-22.
65. Materials Test Equipment . *Agilent Technologies, Inc.* [Online] June 26, 2006. [Cited: May 24, 2012.]
http://www.home.agilent.com/agilent/redirector.jspx?action=ref&lc=eng&cc=MY&nfr=-536902475.0&ckey=670519&cname=AGILENT_EDITORIAL_5989-2589EN.
66. Sabouroux, P. & Ba, D. (2011). Epsimu, a tool for dielectric properties measurement of porous media: Application in wet granular materials characterization. *Progress In Electromagnetics Research B*, 29, 191-207.
67. Palit, S. (2005). *Principles of Electricity and Magnetism*. Harrow, Middlesex: Alpha Science International.
68. Wilk, G. D., Wallace, R. M. & Anthony, J. M. (2001). High-k gate dielectrics: Current status and materials properties. *J. Appl. Phys.* 89(10), 5243.

69. Thiruchitrambalama, M., Palkarb, V. R. & Gopinath, V. (2004). Hydrolysis of aluminium metal and sol–gel processing of nano alumina., *Materials Letters*, 58, 3063-3066.
70. Crisan, M., Zaharescu, M., & Dur, V. (2011). Sol–gel based alumina powders with catalytic applications. *Applied Surface Science*, 258, 448-455.
71. Baiju, K. V. (2007). *Aqueous Sol-Gel Process for Nanocrystalline Photocatalytic Titania, Transparent Functional Coatings and Ceramic Membranes*. Kerala, India: Cochin University of Science and Technology.
72. Askeland, D. R. & Phule, P. P. (2006). *The Science and Engineering of Materials 5th Edition..* Thomson Canada Limited.
73. Ahmed, T. (2006). *Reservoir Engineering Handbook (3rd Ed.)*, Burlington, MA:Elsevier,
74. Yang, J., Gao, M., Zhang, Y., Yang, L., Lang, J., Wang, D., Liu, H., Liu, Y., Wang, Y., Fan, H. (2008). Effects of annealing temperature on morphologies and optical properties of ZnO nanostructures. *Superlattices and Microstructures*, 44(2), 137-142.
75. Kumar, V. R., Kavitha, V. T., Wariar, P. R. S., Nair, S. U. K., Koshy, J (2011). Characterization, sintering and dielectric properties of nanocrystalline zinc oxide prepared by a citric acid-based combustion route. *Journal of Physics and Chemistry of Solids*, 72(4), 290-293.
76. Musić, S. et al. (2003). Influence of chemical synthesis on the crystallization and properties of zinc oxide. *Materials Chemistry and Physics*, 77(2), 521–530
77. Pierre, A C. (2002). *Introduction to sol-gel processing*. Norwell, MA: Kluwer Academic Publisher.
78. Khorsand Zak, A., Ebrahimizadeh Abrishami, M., Abd. Majid, W.H., Yousefi, R., Hosseini, S.M. (2011). Effects of annealing temperature on some structural

- and optical properties of ZnO nanoparticles prepared by a modified sol–gel combustion method. *Ceramics International*, 2011, 37, 393-398.
79. Jones, C. D., Barron, A. R. (2007). Porosity, crystal phase, and morphology of nanoparticle derived alumina as a function of the nanoparticle's carboxylate substituent.. *Materials Chemistry and Physics*, 104(2-3), 460-471.
80. Sharbatdaran, M., Amini, M. M., & Maj, A. (2010). Effect of aluminium alkoxide with donor-functionalized group on texture and morphology of the alumina prepared by sol–gel processings. *Materials Letters*, 64(4), 503-505.
81. Tchomgui-Kamga, E., Alonzo, V., Nanseu-Njiki, C. P., Audebrand, N., Ngameni, E., Darchen, A. (2010). Preparation and characterization of charcoals that contain dispersed aluminium oxide as adsorbents for removal of fluoride from drinking water. *Carbon*, 48(2), 333-343.
82. Rama Rao, G. V. & Venkadesan, S. (1989). Surface Area and Pore Size Studies of Alumina Gels. *Journal of Non-Crystalline Solids*, 111(1), 103-112.
83. Agilent. Technologies. Agilent Solutions for Measuring Permittivity and Permeability with LCR Meters and Impedance Analyzer. *Application Note 1369-1*.
84. Kapustianyk, V. & Eliyashevskyy, Y. (2012). Influence of technological factors on conductivity and dielectric dispersion in ZnO nanocrystalline thin films. *Journal of Alloys and Compounds*, 531, 64-69.
85. Liu, G. Z., Wang, C., Wang, C., Qiu, J., He, M., Xing, J., Jin, K., Lu, H., & Yang, G. Z. (2008). Effects of Interfacial Polarization on the Dielectric Properties of BiFeO₃ Thin Film Capacitors. *App. Phys. Letters*, 92(12).
86. Gray, I. A. R. (2012). Dissipation Factor, Power Factor And Relative Permittivity (Dielectric Constant). [Online] [Cited: September 10, 2012.] <http://www.satcs.co.za/TanD-Res-info.pdf>.
87. Cherry, R. A. & Freeze, J. A. (1979). *Groundwater*. Hemel Hempstead :

- Prentice Hall International.
88. Prosser, A J and Franses, E. I. (2011). Adsorption and surface tension of ionic surfactants at the air–water interface: review and evaluation of equilibrium models. *Colloids and Surfaces A: Physicochem. Eng. Aspects*. 178(1-3), 1-40.
 89. Bera, A., Ojha, K., Mandal, A., Kumar, T. (2011). Interfacial tension and phase behavior of surfactant-oil-brine system. *Colloids and Surfaces A: Physicochem. Eng. Aspects*, 383(1-3), 114-119.
 90. de Aguiar , H. B., de Beer, A. G. F., Strader, M. L. & Roke, S. (2010). The Interfacial Tension of Nanoscopic Oil Droplets in Water Is Hardly Affected by SDS Surfactant. *J. Am. Chem. Soc.*, 132 (7), 2122–2123.
 91. Hunter, T.N., Pugh, R.J., Franks, G.V., Jameson, G.J. (2008). The role of particles in stabilising foams and emulsions. *Advances in Colloid and Interface Science*, 137(2), 57-81.
 92. Kutuzov, S., He, J., Tangirala R., Emrick, T., Russell, T. P., & Böker, A. (2009). On the kinetics of nanoparticle self-assembly at liquid/liquid interfaces. *Phys. Chem. Chem. Phys.*, 9, 6351-6358.
 93. Murshed, S. M. S., Tan, S. H., & Nguyen, N. T. (2008). Temperature dependence of interfacial properties and viscosity of nanofluids for droplet-based microfluidics, *J. Phys. D: Appl. Phys.*, 41(8).
 94. Singh, P. K., Anoop, K. B., Patel, H. E., Sundararajan, T., Pradeep, T., Das, S. K. (2010). Anomalous Size Dependent Rheological Behavior of Alumina Based Nanofluids. *International Journal of Micro-Nano Scale Transport*, 1(2), 179-188.
 95. Ahmari, H. & Etemad, S. G. (2009). Electrorheological response of SnO₂ and Y₂O₃ nanoparticles in silicon oil. *Rheologica Acta*, 48(2), 217-220.
 96. Gao, C. H. (2011, December 12-14). *Advances of Polymer Flood in Heavy Oil*

Recovery. Paper presented at the SPE Heavy Oil Conference and Exhibition, Kuwait City, Kuwait.

97. Arhuoma, M, et al. (2009). *Determination of Increase in Pressure Drop Flooding for Heavy Oil Reservoirs and Oil Recovery Associated with Alkaline.* Paper presented at the Canadian International Petroleum Conference, Calgary, Alberta, Canada.
98. Taber, J. J. & Martin, F. D. (1983). *Technical Screening Guides for the Enhanced Oil Recovery.* Paper presented at the 58th Annual Technical Conference and Exhibition, San Francisco, California.

APPENDIX A

XRD DATA

1. Crystallographic properties of zinc oxide nanoparticles annealed at various temperature

a) Sample: ZnO-300

SS-NNNN	Compound Name	Formula	Y-Scale	d x by	Wavelength
89-0511 (C)	Zinc Oxide	ZnO	50	1	1.5406

System	A	B	C	c/a	alpha	beta	gamma
Hexagonal	3.249	3.249	5.2052	1.602	90	90	120

Bravais L.	Space Group	Z	Volume	I/Ic PDF
Primitive	P63mc (186)	2	47.5847	5.4

Sample Name	Left Angle 2-Theta °	Right Angle 2-Theta °	Left Int. Cps	Right Int. Cps	Obs. Max 2-Theta °
ZnO(300)	36	36.4	78	90.8	36.225

d (Obs. Max Angstrom	Max Int. Cps	Net Height Cps	FWHM 2-Theta °	Chord Mid. 2-Theta °	I. Breadth 2-Theta °
2.47778	621	536	0.145	36.237	0.157

Gravity C. 2-Theta °	d (Gravity C.) Angstrom	Raw Area Cps x 2-Theta °	Net Area Cps x 2-Theta °
36.228	2.4776	118.1	84.33

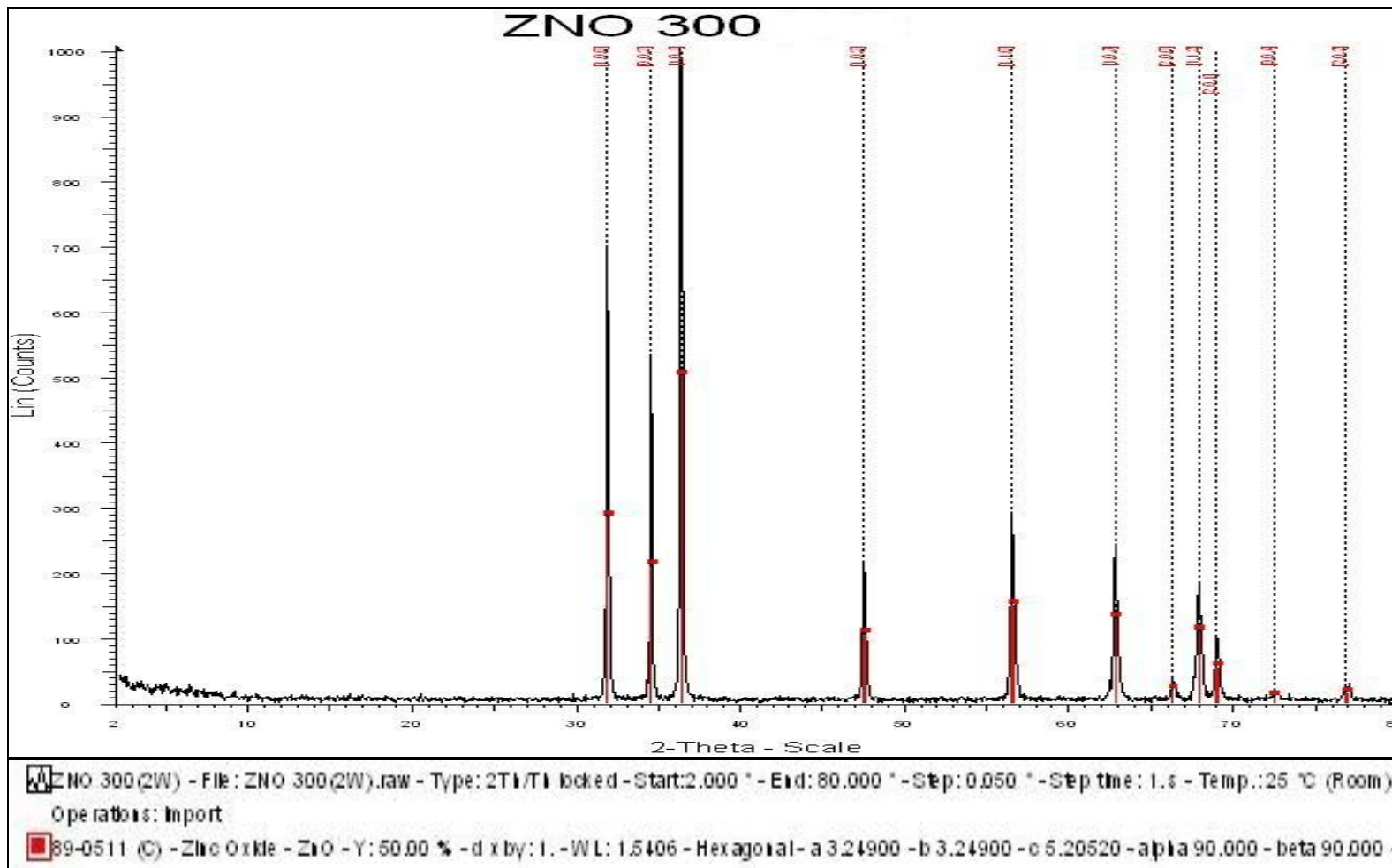


Figure A.1 (a): XRD diffraction pattern of ZnO annealed at 300°C

b) Sample: ZnO-250

SS-NNNN	Compound Name	Formula	Y-Scale	d x by	Wavelength
79-2205 (C)	Zinc Oxide	ZnO	50	1	1.5406

System	a	B	C	c/a	alpha	beta	Gamma
Hexagonal	3.2501	3.2501	5.2071	1.602	90	90	120

Bravais L.	Space Group	Z	Volume	I/Ic PDF
Primitive	P63mc (186)	2	47.6343	5.4

Sample Name	Left Angle 2-Theta °	Right Angle 2-Theta °	Left Int. Cps	Right Int. Cps	Obs. Max 2-Theta °
ZNO 250	36.1	36.7	149	29.7	36.279

d (Obs. Max Angstrom	Max Int. Cps	Net Height Cps	FWHM 2-Theta °	Chord Mid. 2-Theta °	I. Breadth 2-Theta °
2.47423	657	544	0.173	36.282	0.172

Gravity C. 2-Theta °	d (Gravity C.) Angstrom	Raw Area Cps x 2-Theta °	Net Area Cps x 2-Theta °
36.278	2.4743	147.8	93.66

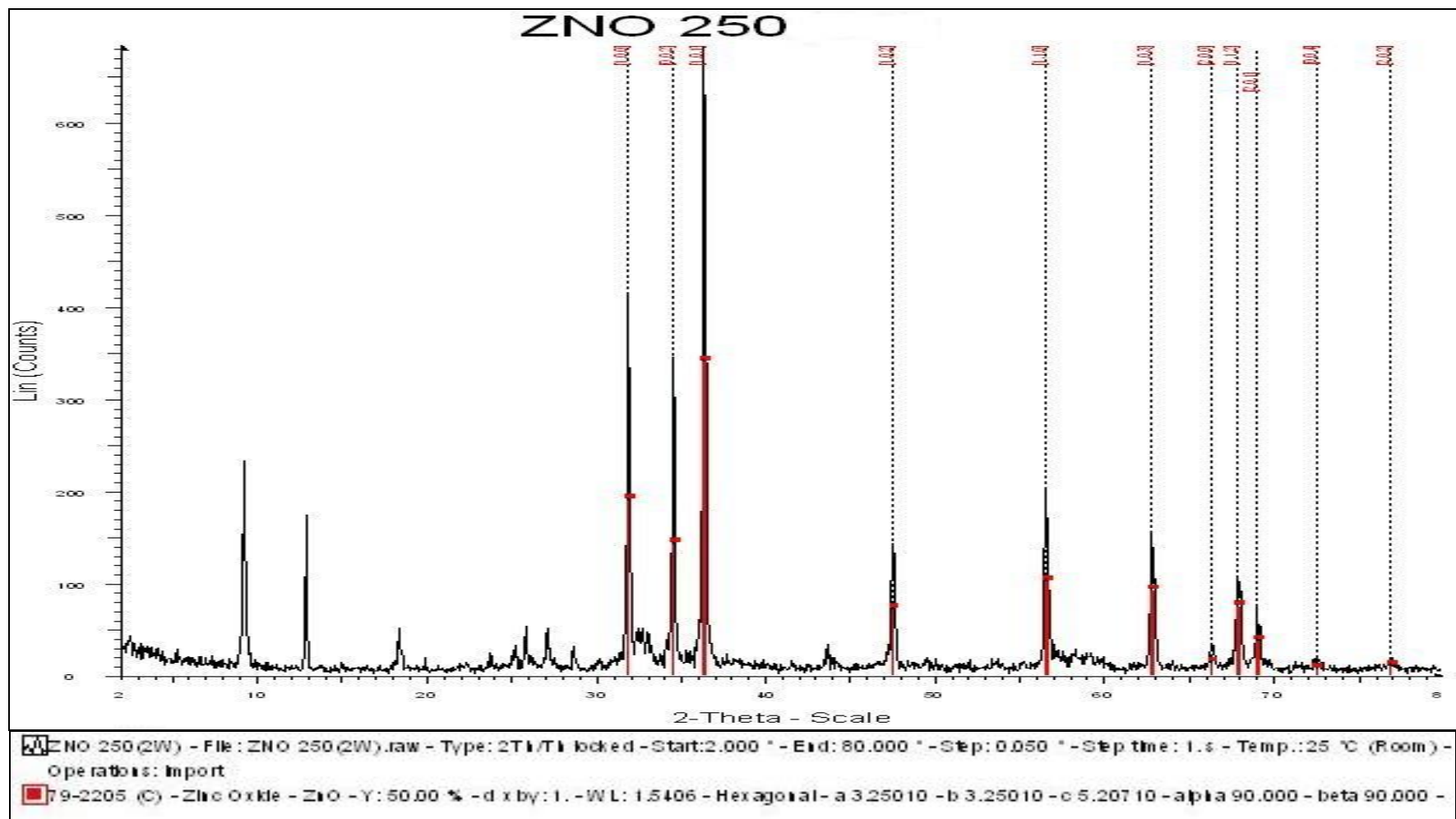


Figure A. 1(b): XRD diffraction pattern of ZnO annealed at 250°C

c) Sample: ZnO- 200

SS-NNNN	Compound Name	Formula	Y-Scale	d x by	Wavelength
70-1361 (C)	Zinc Hydroxide Nitrate	Zn ₃ (OH) ₄ (NO ₃) ₂	50	1	1.5406

System	a	b	c	c/a	alpha	beta	Gamma
Monoclinic	7.038	9.658	11.182	1.588804	90	100.96	90

Bravais L.	Space Group	Z	Volume	I/Ic PDF
Primitive	P21/c (14)	4	746.211	4.3

Sample Name	Left Angle 2-Theta °	Right Angle 2-Theta °	Left Int. Cps	Right Int. Cps	Obs. Max 2-Theta °
ZNO 200	12.6	13	84	28	12.776

d (Obs. Max Angstrom	Max Int. Cps	Net Height Cps	FWHM 2-Theta °	Chord Mid. 2-Theta °	I. Breadth 2-Theta °
6.92352	1234	1174	0.116	12.777	0.127

Gravity C. 2-Theta °	d (Gravity C.) Angstrom	Raw Area Cps x 2-Theta °	Net Area Cps x 2-Theta °
12.775	6.92397	171.6	149.2

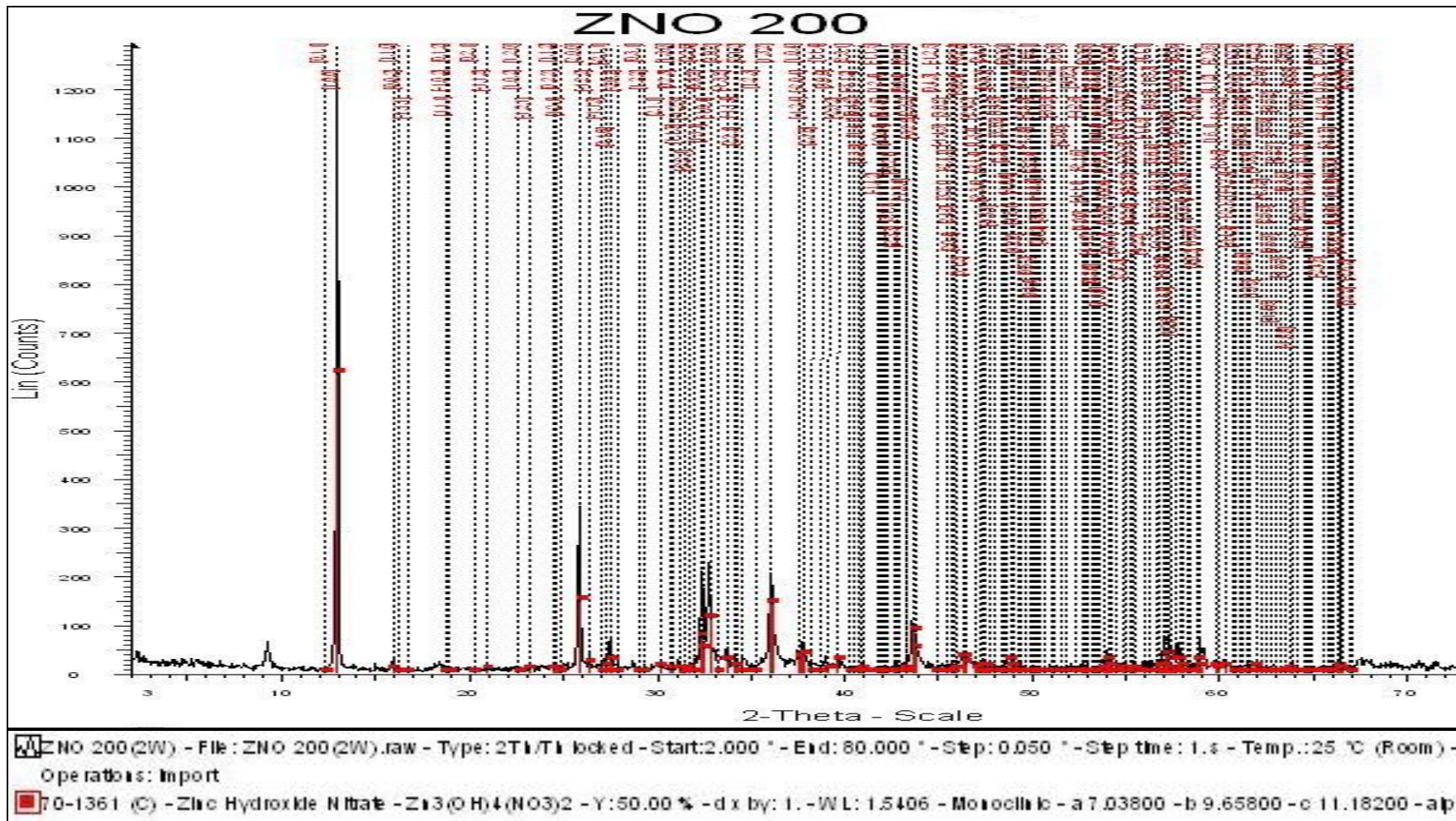


Figure A. 1(c): XRD diffraction pattern of ZnO annealed at 250°C

2. Crystallographic properties of aluminum oxide nanoparticles annealed at various temperature

1. Al_2O_3 -1100

SS-NNNN	Compound Name	Formula	Y-Scale	d x by	Wavelength
88-0826 (A)	Aluminum Oxide	Al_2O_3	50	1	1.5406

System	A	B	c	c/a	alpha	beta	gamma
Hexagonal (Rh)	4.7607	4.761	13	2.73	90	90	120

Bravais L.	Space Group	Z	Volume	I/Ic PDF
Primitive	R-3c (167)	6	255.103	0.9

Sample Name	Left Angle 2-Theta °	Right Angle 2-Theta °	Left Int. Cps	Right Int. Cps	Obs. Max 2-Theta °
1100	43.2	43.6	77	40	43.378

d (Obs. Max) Angstrom	Max Int. Cps	Net Height Cps	FWHM 2-Theta °	Chord Mid. 2-Theta °	I. Breadth 2-Theta °
2.08433	241	180	0.221	43.388	0.216

Gravity C. 2-Theta °	d (Gravity C.) Angstrom	Raw Area Cps x 2-Theta °	Net Area Cps x 2-Theta °
43.388	2.08386	62.42	39.02

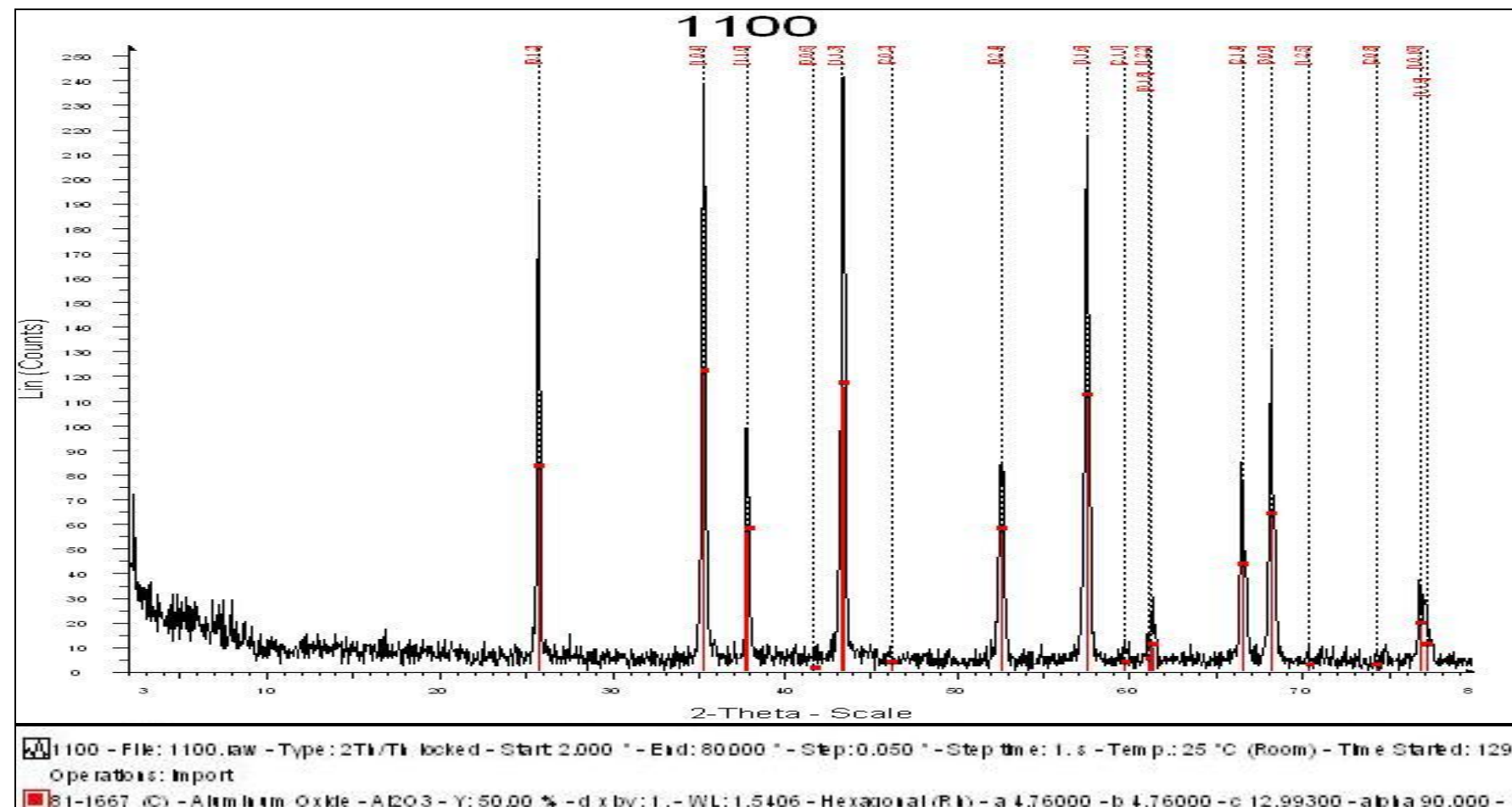


Figure A.2 (a): XRD diffraction pattern of Al₂O₃ annealed at 1100°C

2. Al_2O_3 -1000

SS- NNNN	Compound Name	Formula	Y-Scale	d x by	Wavelength
83-0065 (C)	Staurolite	$(\text{Al}_{17.68}\text{Fe}_{3.12}\text{Mg}_{0.28}\text{Li}_{0.28})(\text{Si}_{7.68}\text{Al}_{0.32})\text{O}_{43.84}(\text{OH})_{4.16}$	50	1	1.5406

System	A	B	c	c/a	alpha	beta	Gamma
Monoclinic	7.861	16.61	5.649	0.719	90	90.18	90

Bravais L.	Space Group	Z	Volume	I/Ic PDF
Base-centred	C2/m (12)	1	737.593	0.4

Sample Name	Left Angle 2-Theta °	Right Angle 2-Theta °	Left Int. Cps	Right Int. Cps	Obs. Max 2-Theta °
1000	34.95	35.25	25	43	35.111

d (Obs. Max) Angstrom	Max Int. Cps	Net Height Cps	FWHM 2-Theta °	Chord Mid. 2-Theta °	I. Breadth 2-Theta °
2.55377	66.6	32	0.148	35.136	0.122

Gravity C. 2-Theta °	d (Gravity C.) Angstrom	Raw Area Cps x 2-Theta °	Net Area Cps x 2-Theta °
35.138	2.55191	14.1	3.899

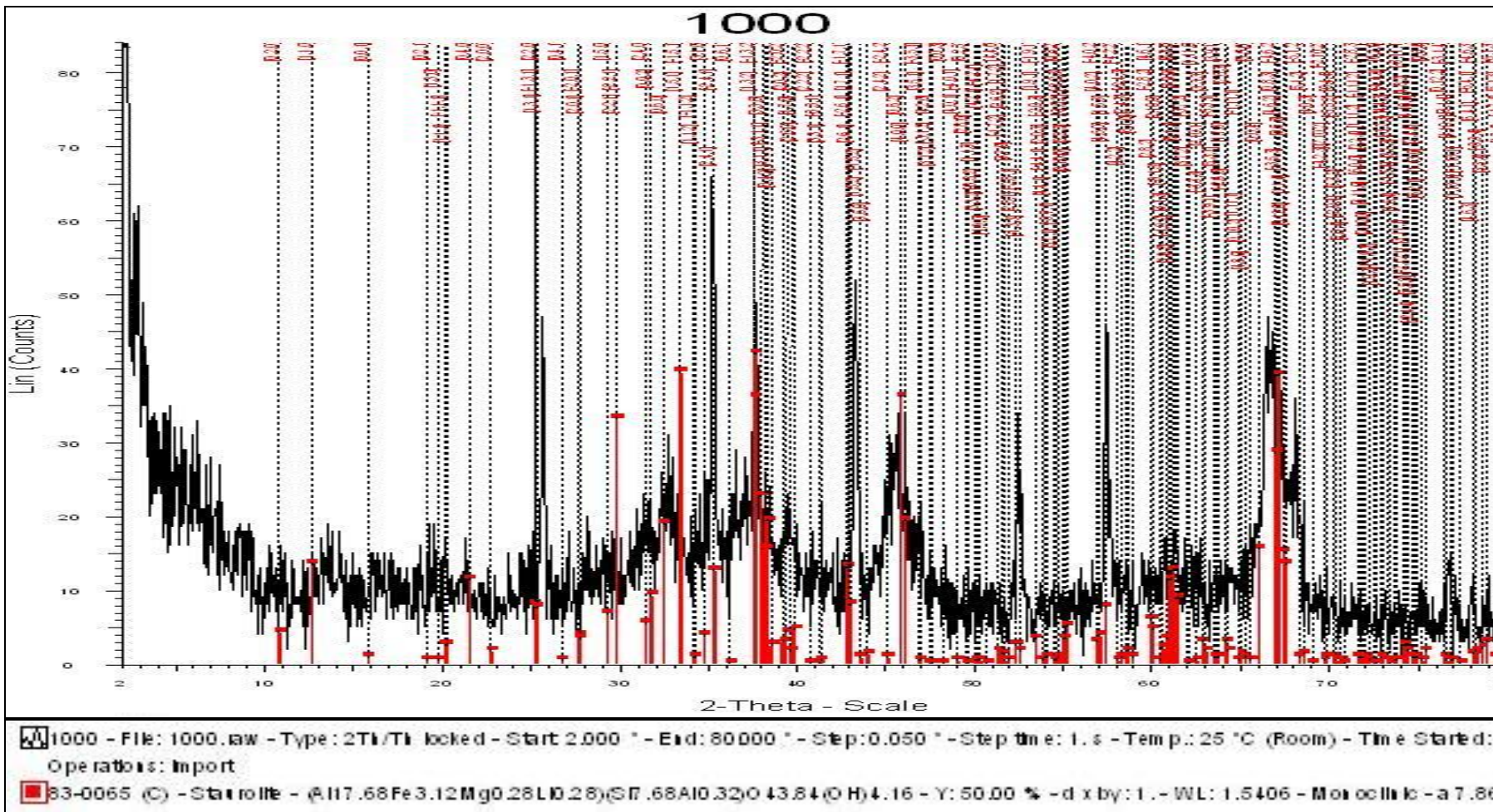


Figure A.2 (b): XRD diffraction pattern of Al_2O_3 annealed at 1000°C

3. Al₂O₃-900

SS-NNNN	Compound Name	Formula	Y-Scale	d x by	Wavelength
88-1609 (C)	Aluminum Oxide	AlAl _{1.6} O ₄	50	1	1.5406

System	a	b	c	c/a	alpha	beta	gamma
Tetragonal	5.599	5.599	23.66	4.225	90	90	90

Bravais L.	Space Group	Z	Volume	I/Ic PDF
Primitive	P-4m2 (115)	12	741.619	0.9

Data from synthesized sample.

Sample Name	Left Angle 2-Theta	Right Angle 2-Theta	Left Int. Cps	Right Int. Cps	Obs. Max 2-Theta
900	66.25	67.85	20.9	19.3	66.671

d (Obs. Max) Angstrom	Max Int. Cps	Net Height Cps	FWHM 2-Theta	Chord Mid. 2-Theta	I. Breadth 2-Theta
1.4017	38.3	17.9	0.602	66.923	0.723

Gravity C. 2-Theta °	d (Gravity C.) Angstrom	Raw Area Cps x 2-Theta	Net Area Cps x 2-Theta
67.099	1.39382	45.14	12.93

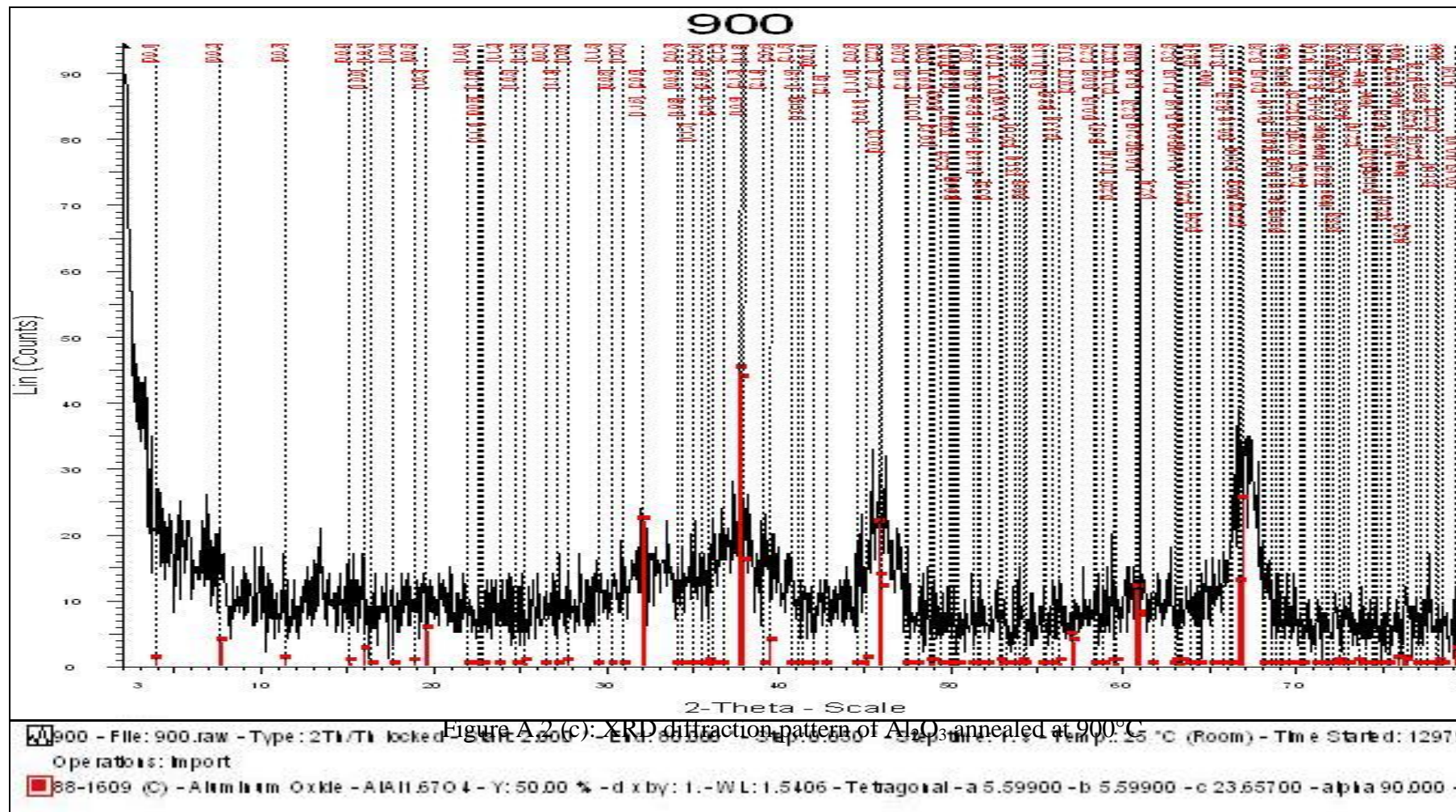


Figure A.2 (c): XRD diffraction pattern of Al_2O_3 annealed at 900°C

APPENDIX B

INTERFACIAL TENSION (IFT) MEASUREMENT

Abbreviations and units used in the list:

IFT_LY	: interface tension (Laplace - Young);
IFT_CSW	: interface tension (Cayias Schechter Wade);
F	: full shape;
L	: left side;
R	: right side;
C	: cylindrical part;
dDens	: density difference [g/cm ³];
Vol	: volume [μl];
Err	: fitting error [pixel];
Speed	: rotation speed [1/min];
Alpha	: drop shape parameter alpha;
a	: drop curvature at apex [mm]

1. IFT of Oil – Al₂O₃ Nanofluid

Run-No	IFT_LY	IFT_CSW	Err	Speed	Vol LY	Type	SA_LY	DiaH	DiaV	T
1	4.131	4.162	0.7	0000.0	2.639	F	11.55	3.83	1.03	59.8
2	4.142	4.162	0.5	9999.7	2.641	F	11.55	3.83	1.03	59.8
3	4.143	4.163	0.5	9999.7	2.637	F	11.53	3.82	1.03	59.8
4	4.138	4.163	0.5	0000.1	2.625	F	11.49	3.81	1.03	59.9
5	4.192	4.162	1.0	9999.8	2.669	F	11.63	3.82	1.03	59.9
6	4.157	4.162	0.5	0000.0	2.637	F	11.52	3.81	1.03	59.9
7	4.195	4.162	0.9	9999.6	2.662	F	11.59	3.81	1.03	59.9
8	4.435	4.397	0.9	0000.1	2.803	F	11.99	3.87	1.05	59.9
9	4.415	4.397	0.4	0000.2	2.781	F	11.92	3.86	1.05	59.9
10	4.437	4.397	0.7	9999.6	2.795	F	11.96	3.86	1.05	59.9
11	4.369	4.397	0.5	0000.1	2.752	F	11.84	3.86	1.05	59.9
12	4.411	4.398	0.4	0000.1	2.758	F	11.83	3.85	1.05	59.9
13	4.437	4.397	0.8	0000.0	2.795	F	11.96	3.86	1.05	59.9
14	4.436	4.396	0.8	0000.0	2.795	F	11.96	3.86	1.05	59.8
15	4.416	4.397	0.6	0000.3	2.783	F	11.93	3.86	1.05	59.8
16	4.402	4.398	0.6	0000.1	2.782	F	11.93	3.87	1.05	59.8
17	4.410	4.397	0.6	0000.1	2.788	F	11.95	3.87	1.05	59.8
18	4.372	4.396	0.5	9999.6	2.767	F	11.89	3.87	1.05	59.8
19	4.364	4.395	0.3	9999.0	2.769	F	11.90	3.88	1.05	59.8
20	4.367	4.396	0.6	9999.4	2.791	F	11.98	3.90	1.05	59.8
21	4.405	4.397	0.5	9999.7	2.814	F	12.05	3.90	1.05	59.8
22	4.366	4.396	0.5	9999.7	2.799	F	12.02	3.92	1.05	59.8
23	4.369	4.396	0.5	0000.4	2.811	F	12.06	3.93	1.05	59.7
24	4.373	4.397	0.5	0000.4	2.813	F	12.07	3.93	1.05	59.7
25	4.404	4.398	0.6	0000.0	2.822	F	12.08	3.91	1.05	59.7
26	4.359	4.396	0.6	0000.2	2.814	F	12.08	3.94	1.05	59.7
27	4.370	4.396	0.5	0000.0	2.812	F	12.06	3.93	1.05	59.7
28	4.408	4.396	0.7	9999.1	2.827	F	12.10	3.92	1.05	59.7
29	4.416	4.396	0.5	9999.7	2.813	F	12.04	3.93	1.05	59.8
30	4.393	4.396	0.5	9999.5	2.811	F	12.05	3.93	1.05	59.8
31	4.398	4.395	0.4	9999.5	2.812	F	12.05	3.94	1.05	59.7
32	4.458	4.396	0.9	9999.8	2.868	F	12.22	3.93	1.05	59.7
33	4.403	4.395	0.6	9999.5	2.843	F	12.16	3.94	1.05	59.7
34	4.481	4.396	1.3	9999.5	2.893	F	12.30	3.94	1.05	59.7
35	4.442	4.396	0.9	9999.7	2.868	F	12.23	3.94	1.05	59.7
36	4.417	4.396	0.6	0000.3	2.862	F	12.22	3.95	1.05	59.7
37	4.367	4.396	0.6	9999.7	2.839	F	12.17	3.96	1.05	59.7
38	4.422	4.395	0.5	0000.1	2.848	F	12.17	3.96	1.05	59.7
39	4.414	4.396	0.7	0000.1	2.870	F	12.26	3.96	1.05	59.7
40	4.394	4.395	0.6	9999.8	2.867	F	12.26	3.97	1.05	59.7
41	4.363	4.396	0.5	9999.8	2.847	F	12.20	3.97	1.05	59.7
42	4.438	4.396	0.5	0000.5	2.876	F	12.26	3.99	1.05	59.7
43	4.371	4.395	0.5	9999.4	2.871	F	12.29	3.99	1.05	59.7

Abbreviations and units used in the list: IFT_LY = interface tension (Laplace - Young); IFT_CSW = interface tension (Caydas Schechter Wade); F = full shape; L = left side; R = right side; C = cylindrical part; dDens = density difference [g/cm³]; Vol = volume [μl]; Err = fitting error [pixel]; Speed = rotation speed [1/min]; Alpha = drop shape parameter alpha; a = drop curvature at apex [mm]

47	4.381	4.395	0.6	9999.4	2.865	F	12.26	4.01	1.05	59.7
48	4.487	4.395	1.5	9999.8	2.958	F	12.54	4.01	1.05	59.7
49	4.472	4.395	1.2	9999.6	2.948	F	12.51	4.01	1.05	59.7
50	4.464	4.395	1.3	9999.4	2.953	F	12.54	4.02	1.05	59.7
51	4.385	4.396	0.5	0000.3	2.890	F	12.35	4.01	1.05	59.7
52	4.489	4.397	1.5	0000.4	2.969	F	12.58	4.02	1.05	59.7
53	4.384	4.395	0.4	0000.4	2.879	F	12.31	3.99	1.05	59.7
54	4.371	4.396	0.4	0000.4	2.871	F	12.29	3.99	1.05	59.7
55	4.364	4.396	0.4	9999.5	2.857	F	12.24	3.98	1.05	59.7
56	4.382	4.396	0.5	9999.6	2.879	F	12.31	3.99	1.05	59.7
57	4.363	4.395	0.3	9999.4	2.866	F	12.27	3.99	1.05	59.7
58	4.424	4.396	0.4	9999.7	2.874	F	12.26	3.99	1.05	59.7
59	4.373	4.396	0.4	9999.7	2.873	F	12.29	3.99	1.05	59.7
60	4.383	4.396	0.4	0000.4	2.868	F	12.27	3.99	1.05	59.7
61	4.357	4.397	0.4	0000.4	2.871	F	12.30	4.01	1.05	59.7
62	4.364	4.396	0.4	0000.1	2.864	F	12.26	3.99	1.05	59.7
63	4.391	4.502	0.4	9999.6	2.883	F	12.32	4.01	1.06	59.7
64	4.403	4.396	0.5	0000.3	2.888	F	12.33	4.01	1.05	59.7
65	4.390	4.396	0.4	9999.7	2.881	F	12.31	4.01	1.05	59.7
66	4.363	4.501	0.4	9999.7	2.872	F	12.29	4.02	1.06	59.7
67	4.369	4.396	0.3	9999.5	2.881	F	12.33	4.02	1.05	59.7
68	4.401	4.396	0.5	0000.4	2.900	F	12.38	4.03	1.05	59.7
69	4.400	4.396	0.4	0000.4	2.899	F	12.38	4.02	1.05	59.7
70	4.360	4.395	0.4	9999.6	2.893	F	12.38	4.03	1.05	59.7
71	4.389	4.395	0.6	9999.4	2.913	F	12.43	4.03	1.05	59.7
72	4.375	4.501	0.4	9999.4	2.893	F	12.37	4.02	1.06	59.7
73	4.508	4.502	0.8	0000.4	2.954	F	12.52	4.02	1.06	59.7
74	4.409	4.501	0.3	0000.1	2.895	F	12.35	4.02	1.06	59.7
75	4.392	4.502	0.4	0000.1	2.884	F	12.32	4.02	1.06	59.7
76	4.497	4.501	0.8	0000.1	2.949	F	12.50	4.02	1.06	59.7
77	4.382	4.502	1.1	0000.2	2.891	F	12.36	4.03	1.06	59.7
78	4.389	4.501	1.7	0000.3	2.903	F	12.40	4.04	1.06	59.7
79	4.397	4.501	1.0	9999.4	2.909	F	12.41	4.04	1.06	59.7
80	4.503	4.502	0.6	0000.1	2.946	F	12.49	4.04	1.06	59.7
81	4.385	4.501	1.4	0000.1	2.903	F	12.40	4.04	1.06	59.7
82	4.411	4.502	1.3	0001.0	2.910	F	12.41	4.04	1.06	59.7
83	4.508	4.500	0.7	0000.1	2.950	F	12.50	4.05	1.06	59.7
84	4.468	4.500	0.7	9999.6	2.947	F	12.51	4.04	1.06	59.7
85	4.500	4.501	0.7	0000.0	2.954	F	12.52	4.04	1.06	59.7
86	4.519	4.500	0.8	9999.6	2.955	F	12.51	4.05	1.06	59.7
87	4.466	4.501	0.7	9999.5	2.955	F	12.54	4.05	1.06	59.7
88	4.512	4.501	0.7	0000.1	2.957	F	12.53	4.05	1.06	59.7
89	4.505	4.501	1.1	9999.5	2.992	F	12.66	4.06	1.06	59.7
90	4.519	4.500	0.7	9999.5	2.967	F	12.56	4.05	1.06	59.7
91	4.496	4.500	0.6	9999.8	2.955	F	12.53	4.05	1.06	59.7
92	4.471	4.501	0.6	0000.3	2.935	F	12.47	4.04	1.06	59.7
93	4.513	4.500	0.8	9999.6	2.967	F	12.56	4.03	1.06	59.7
94	4.501	4.501	0.5	0000.7	2.942	F	12.48	4.03	1.06	59.7
95	4.492	4.500	0.6	0000.1	2.922	F	12.40	4.02	1.06	59.8

Abbreviations and units used in the list: IFT_LY = Interface tension (Laplace - Young); IFT_CSW = Interface tension (Caydas Schechter Wade); F = full shape; L = left side; R = right side; C = cylindrical part; dDens = density difference [g/cm^3]; Vol = volume [μl]; Err = fitting error [pixel]; Speed = rotation speed [1/min]; Alpha = drop shape parameter alpha; a = drop curvature at apex [mm]

98	4.476	4.501	0.7	9999.8	2.932	F	12.45	4.02	1.06	59.7
99	4.373	4.395	0.4	9999.4	2.878	F	12.31	4.01	1.05	59.8
100	4.363	4.394	0.5	9999.6	2.876	F	12.31	4.01	1.05	59.7
101	4.447	4.396	1.0	9999.7	2.941	F	12.50	4.02	1.05	59.7
102	4.408	4.396	0.4	0000.0	2.898	F	12.37	4.02	1.05	59.7
103	4.371	4.499	0.5	9999.1	2.885	F	12.34	4.03	1.06	59.7
104	4.373	4.501	0.5	9999.7	2.883	F	12.33	4.02	1.06	59.7
105	4.357	4.500	0.5	9999.5	2.884	F	12.35	4.03	1.06	59.7
106	4.413	4.501	1.1	9999.6	2.901	F	12.37	4.03	1.06	59.7
107	4.370	4.500	0.4	9999.3	2.902	F	12.40	4.04	1.06	59.7
108	4.464	4.498	0.5	9999.4	2.945	F	12.51	4.04	1.06	59.7
109	4.455	4.502	0.5	0001.3	2.948	F	12.52	4.05	1.06	59.7
110	4.518	4.605	0.7	9999.1	2.968	F	12.56	4.05	1.07	59.7
111	4.374	4.502	1.1	0000.4	2.922	F	12.48	4.05	1.06	59.8
112	4.409	4.499	0.4	9999.5	2.931	F	12.49	4.06	1.06	59.8
113	4.408	4.499	0.8	9999.3	2.935	F	12.50	4.07	1.06	59.7
114	4.352	4.501	1.5	9999.3	2.917	F	12.47	4.07	1.06	59.8
115	4.597	4.500	1.4	9999.7	3.053	F	12.83	4.06	1.06	59.8
116	4.554	4.501	1.2	0000.0	3.024	F	12.75	4.06	1.06	59.8
117	4.600	4.502	1.7	0000.4	3.055	F	12.84	4.06	1.06	59.8
118	4.536	4.500	1.1	0000.1	3.002	F	12.68	4.05	1.06	59.8
119	4.417	4.500	3.2	9999.5	2.934	F	12.50	4.05	1.06	59.8
120	4.512	4.500	0.9	9999.3	2.986	F	12.63	4.05	1.06	59.8
121	4.510	4.501	0.7	0000.2	2.964	F	12.55	4.05	1.06	59.8
122	4.471	4.501	0.5	0000.0	2.955	F	12.54	4.05	1.06	59.8
123	4.468	4.501	0.7	0000.0	2.956	F	12.55	4.05	1.06	59.8
124	4.468	4.500	0.4	0000.1	2.945	F	12.50	4.04	1.06	59.8
125	4.492	4.501	0.5	0000.1	2.953	F	12.52	4.03	1.06	59.8
126	4.410	4.396	0.4	0000.1	2.913	F	12.42	4.03	1.05	59.8
127	4.415	4.395	0.3	9999.3	2.911	F	12.41	4.04	1.05	59.8
128	4.412	4.395	0.7	9999.3	2.939	F	12.52	4.04	1.05	59.8
129	4.418	4.396	0.5	0000.3	2.912	F	12.41	4.04	1.05	59.8
130	4.421	4.396	0.5	9999.7	2.916	F	12.43	4.04	1.05	59.8
131	4.416	4.396	0.4	0000.1	2.916	F	12.43	4.04	1.05	59.8
132	4.415	4.501	0.4	0000.2	2.914	F	12.42	4.04	1.06	59.8
133	4.421	4.397	0.4	0001.1	2.924	F	12.45	4.04	1.05	59.8
134	4.356	4.394	0.4	9999.0	2.901	F	12.41	4.04	1.05	59.8
135	4.422	4.396	0.7	0000.0	2.935	F	12.50	4.03	1.05	59.8
136	4.387	4.395	0.5	9999.4	2.906	F	12.41	4.03	1.05	59.8
137	4.352	4.396	0.5	0000.1	2.898	F	12.40	4.04	1.05	59.8
138	4.366	4.395	0.4	9999.7	2.917	F	12.46	4.05	1.05	59.8
139	4.427	4.501	0.9	9999.3	2.932	F	12.48	4.05	1.06	59.8
140	4.399	4.501	1.9	0000.2	2.919	F	12.45	4.05	1.06	59.8
141	4.619	4.502	1.9	0000.0	3.067	F	12.87	4.06	1.06	59.8
142	4.489	4.500	0.8	0000.0	2.981	F	12.63	4.06	1.06	59.8
143	4.500	4.501	0.9	0000.3	2.987	F	12.64	4.06	1.06	59.7
144	4.525	4.501	0.6	9999.4	2.980	F	12.60	4.07	1.06	59.8
145	4.505	4.501	0.6	9999.7	2.975	F	12.60	4.07	1.06	59.7
146	4.482	4.499	0.6	9999.3	2.967	F	12.58	4.07	1.06	59.8
147	4.525	4.501	0.7	9999.5	2.990	F	12.64	4.08	1.06	59.7

Abbreviations and units used in the list: IFT_LY = Interface tension (Laplace - Young); IFT_CSW = Interface tension (Caydas Schechter Wade); F = full shape; L = left side; R = right side; C = cylindrical part; dDens = density difference [g/cm³]; Vol = volume [μl]; Err = fitting error [pixel]; Speed = rotation speed [1/min]; Alpha = drop shape parameter alpha; a = drop curvature at apex [mm].

150	4.512	4.502	1.0	0000.3	3.046	F	12.86	4.12	1.06	59.7
151	4.533	4.501	1.1	9999.4	3.071	F	12.94	4.13	1.06	59.7
152	4.501	4.501	0.7	0000.4	3.029	F	12.80	4.13	1.06	59.7
153	4.430	4.395	0.5	9999.3	3.003	F	12.75	4.13	1.05	59.7
154	4.435	4.395	0.5	9999.7	3.008	F	12.76	4.14	1.05	59.7
155	4.427	4.395	0.5	0000.0	3.008	F	12.77	4.14	1.05	59.8
156	4.353	4.396	0.4	0000.2	2.986	F	12.73	4.14	1.05	59.7
157	4.367	4.394	0.4	9999.4	2.997	F	12.77	4.14	1.05	59.7
158	4.420	4.395	0.4	9999.4	3.016	F	12.80	4.15	1.05	59.7
159	4.401	4.395	0.6	0000.4	3.029	F	12.87	4.15	1.05	59.7
160	4.353	4.396	0.4	0000.1	2.997	F	12.78	4.15	1.05	59.7
161	1.121	1.055	1.0	1099.9	3.295	F	10.74	2.00	1.77	59.7

Abbreviations and units used in the list: IFT_LY = interface tension (Laplace - Young); IFT_CSW = interface tension (Caydas Schechter Wade); F = full shape; L = left side; R = right side; C = cylindrical part; dDens = density difference [g/cm^3]; Vol = volume [μl]; Err = fitting error [pixel]; Speed = rotation speed [1/min]; Alpha = drop shape parameter alpha; a = drop curvature at apex [mm].

2. IFT of Oil-ZnO nanofluid

Run-No	IFT_LY	IFT_CSW	Err	Speed	Vol_LY	Type	SA_LY	DiAH	DiAV	T
1	4.027	4.125	0.8	9900.2	2.697	F	11.75	3.9	1.04	59.7
2	4.064	4.124	0.9	9900.2	2.714	F	11.79	3.9	1.04	59.7
3	4.063	4.125	0.8	9900.2	2.713	F	11.79	3.9	1.04	59.7
4	4.033	4.124	0.8	9900.2	2.693	F	11.73	3.9	1.04	59.7
5	4.026	4.125	0.9	9900.2	2.697	F	11.75	3.91	1.04	59.7
6	4.018	4.125	0.9	9899.8	2.697	F	11.75	3.9	1.04	59.6
7	4.15	4.126	1.1	9900.2	2.771	F	11.95	3.9	1.04	59.6
8	4.174	4.124	1.6	9899.8	2.797	F	12.03	3.91	1.04	59.6
9	4.018	4.124	0.8	9899.8	2.69	F	11.72	3.9	1.04	59.6
10	4.044	4.125	0.9	9900.2	2.701	F	11.75	3.9	1.04	59.6
11	4.172	4.125	1.3	9900.2	2.795	F	12.03	3.91	1.04	59.6
12	4.044	4.126	0.9	9899.8	2.705	F	11.76	3.9	1.04	59.6
13	4.051	4.124	0.8	9899.8	2.708	F	11.77	3.9	1.04	59.6
14	4.022	4.125	0.8	9900.2	2.691	F	11.72	3.9	1.04	59.6
15	4.15	4.125	1	9899.8	2.773	F	11.96	3.9	1.04	59.7
16	4.166	4.125	1.1	9899.8	2.783	F	11.98	3.9	1.04	59.6
17	4.013	4.124	0.9	9899.8	2.69	F	11.73	3.9	1.04	59.6
18	4.145	4.125	1	9899.8	2.768	F	11.94	3.9	1.04	59.7
19	4.106	4.124	0.6	9899.8	2.742	F	11.87	3.9	1.04	59.7
20	4.104	4.124	0.7	9899.8	2.741	F	11.86	3.9	1.04	59.8
21	4.105	4.125	0.6	9900.2	2.741	F	11.86	3.9	1.04	59.8
22	4.176	4.124	1.3	9899.8	2.79	F	12.01	3.9	1.04	59.8
23	4.18	4.125	1.3	9899.8	2.792	F	12.01	3.9	1.04	59.8
24	4.108	4.126	0.7	9900.2	2.743	F	11.87	3.9	1.04	59.8
25	4.106	4.124	0.6	9900.2	2.742	F	11.87	3.9	1.04	59.8
26	4.163	4.125	1.2	9900.2	2.78	F	11.98	3.9	1.04	59.7
27	4.153	4.125	1.1	9899.8	2.774	F	11.96	3.9	1.04	59.7
28	4.163	4.125	1.3	9899.8	2.78	F	11.98	3.9	1.04	59.8
29	4.112	4.126	0.9	9900.7	2.746	F	11.88	3.9	1.04	59.8
30	4.032	4.125	0.9	9900.2	2.701	F	11.76	3.89	1.04	59.7
31	4.103	4.124	0.7	9899.8	2.741	F	11.86	3.9	1.04	59.7
32	4.105	4.124	0.7	9899.8	2.741	F	11.87	3.9	1.04	59.7
33	4.104	4.125	0.6	9900.2	2.732	F	11.83	3.89	1.04	59.7
34	4.176	4.125	1.2	9899.8	2.78	F	11.97	3.89	1.04	59.7
35	4.171	4.125	1.3	9900.2	2.785	F	11.99	3.9	1.04	59.7
36	4.19	4.124	1.6	9900.2	2.799	F	12.03	3.9	1.04	59.7
37	4.168	4.124	1.2	9899.8	2.775	F	11.95	3.89	1.04	59.7
38	4.147	4.125	1.2	9900.2	2.769	F	11.95	3.9	1.04	59.7
39	4.165	4.124	0.6	9899.3	2.735	F	11.81	3.9	1.04	59.7
40	4.158	4.124	0.5	9900.2	2.735	F	11.81	3.89	1.04	59.7
41	4.167	4.125	1.3	9900.2	2.783	F	11.98	3.9	1.04	59.7
42	4.105	4.125	0.6	9900.2	2.733	F	11.83	3.89	1.04	59.7
43	4.19	4.123	1.6	9899.3	2.799	F	12.03	3.9	1.04	59.8
44	4.174	4.124	1.2	9899.8	2.78	F	11.97	3.89	1.04	59.8
45	4.178	4.124	1.4	9899.8	2.782	F	11.97	3.89	1.04	59.7
46	4.183	4.124	1.3	9899.8	2.785	F	11.98	3.89	1.04	59.8
47	4.104	4.124	0.7	9899.8	2.732	F	11.83	3.89	1.04	59.8

48	4.099	4.118	0.4	9999.6	2.716	F	11.82	3.93	1.03	59.8
49	4.102	4.207	0.6	9999.7	2.714	F	11.81	3.93	1.04	59.8
50	4.127	4.209	1	10000.4	2.729	F	11.86	3.93	1.04	59.8
51	4.106	4.209	0.9	10000.1	2.714	F	11.81	3.93	1.04	59.8
52	4.13	4.119	0.5	9999.6	2.728	F	11.85	3.93	1.03	59.8
53	4.119	4.207	0.5	10000	2.723	F	11.84	3.93	1.04	59.8
54	4.113	4.119	0.7	10000	2.742	F	11.91	3.93	1.03	59.8
55	4.107	4.118	0.6	9999.7	2.738	F	11.9	3.93	1.03	59.8
56	4.105	4.208	0.5	9999.5	2.718	F	11.83	3.93	1.04	59.8
57	4.113	4.209	0.4	10000.4	2.721	F	11.83	3.93	1.04	59.7
58	4.108	4.208	0.4	9999.7	2.717	F	11.82	3.93	1.04	59.7
59	4.097	4.208	0.7	10000	2.708	F	11.8	3.93	1.04	59.7
60	4.108	4.208	0.6	10000	2.715	F	11.81	3.93	1.04	59.7
61	4.095	4.208	0.4	9999.4	2.713	F	11.81	3.93	1.04	59.7
62	4.133	4.209	0.5	10000.3	2.727	F	11.85	3.92	1.04	59.8
63	4.104	4.209	0.5	10000.1	2.713	F	11.81	3.92	1.04	59.7
64	4.095	4.207	0.6	9999.5	2.717	F	11.83	3.93	1.04	59.7
65	4.096	4.21	0.5	10000.4	2.716	F	11.83	3.93	1.04	59.7
66	4.096	4.208	0.5	9999.7	2.709	F	11.8	3.93	1.04	59.7
67	4.094	4.208	0.5	9999.7	2.711	F	11.81	3.93	1.04	59.7
68	4.145	4.209	0.5	10000.1	2.731	F	11.85	3.92	1.04	59.7
69	4.126	4.208	0.5	9999.5	2.723	F	11.83	3.92	1.04	59.7
70	4.099	4.119	0.4	10000.1	2.724	F	11.85	3.92	1.03	59.7
71	4.135	4.209	0.4	10000.2	2.729	F	11.85	3.92	1.04	59.7
72	4.128	4.209	0.4	10000.2	2.721	F	11.83	3.92	1.04	59.7
73	4.106	4.208	0.5	9999.7	2.715	F	11.82	3.93	1.04	59.7
74	4.119	4.208	0.4	9999.6	2.722	F	11.83	3.93	1.04	59.7
75	4.091	4.208	0.9	9999.5	2.704	F	11.78	3.93	1.04	59.7
76	4.117	4.208	0.4	9999.7	2.72	F	11.83	3.92	1.04	59.7
77	4.097	4.209	0.4	10000.1	2.707	F	11.79	3.93	1.04	59.7
78	4.127	4.209	1.1	10000	2.724	F	11.84	3.92	1.04	59.7
79	4.109	4.208	0.5	10000	2.715	F	11.81	3.93	1.04	59.7
80	4.144	4.208	0.4	9999.4	2.73	F	11.85	3.92	1.04	59.7
81	4.095	4.208	0.5	9999.7	2.712	F	11.81	3.93	1.04	59.7
82	4.112	4.209	0.8	9999.7	2.717	F	11.82	3.93	1.04	59.8
83	4.12	4.209	0.4	9999.5	2.723	F	11.84	3.93	1.04	59.8
84	4.104	4.209	1.1	10000.1	2.712	F	11.81	3.92	1.04	59.8
85	4.132	4.209	0.8	9999.8	2.723	F	11.83	3.92	1.04	59.7
86	4.141	4.209	0.7	9999.6	2.728	F	11.84	3.92	1.04	59.7
87	4.132	4.208	0.4	9999.4	2.725	F	11.84	3.92	1.04	59.7
88	4.111	4.209	1	10000	2.716	F	11.82	3.93	1.04	59.7
89	4.114	4.209	0.8	10000.7	2.716	F	11.82	3.92	1.04	59.7
90	4.186	4.208	0.5	9999.5	2.74	F	11.86	3.92	1.04	59.7
91	4.261	4.209	1.5	9999.7	2.807	F	12.07	3.92	1.04	59.8
92	4.219	4.208	1.2	9999.8	2.78	F	11.99	3.92	1.04	59.8
93	4.191	4.208	0.7	9999.8	2.74	F	11.86	3.92	1.04	59.8
94	4.219	4.209	0.5	9999.6	2.753	F	11.89	3.92	1.04	59.8
95	4.112	4.208	0.9	9999.4	2.713	F	11.8	3.92	1.04	59.8
96	4.129	4.209	1	10000.3	2.72	F	11.82	3.92	1.04	59.8
97	4.254	4.209	0.7	9999.7	2.763	F	11.91	3.92	1.04	59.8

98	4.107	4.209	0.7	9999.7	2.709	F	11.79	3.92	1.04	59.8
99	4.186	4.208	0.9	10000	2.758	F	11.93	3.92	1.04	59.9
100	4.245	4.209	0.6	9999.6	2.756	F	11.89	3.92	1.04	59.9
101	4.157	4.21	0.7	10000.7	2.74	F	11.88	3.92	1.04	59.8
102	4.097	4.208	0.5	9999.1	2.71	F	11.8	3.92	1.04	59.8
103	4.105	4.209	0.9	9999.5	2.709	F	11.79	3.92	1.04	59.8
104	4.129	4.207	1.1	9999.1	2.72	F	11.82	3.92	1.04	59.8
105	4.21	4.208	0.6	10000.1	2.743	F	11.86	3.92	1.04	59.8
106	4.108	4.209	0.5	10000	2.708	F	11.79	3.92	1.04	59.7
107	4.135	4.208	0.6	10000	2.714	F	11.79	3.92	1.04	59.8
108	4.119	4.207	0.5	10000	2.715	F	11.81	3.92	1.04	59.8
109	4.171	4.118	1.2	9999.7	2.772	F	11.99	3.92	1.03	59.8
110	4.172	4.207	0.5	9999.7	2.749	F	11.9	3.92	1.04	59.8
111	4.181	4.208	0.8	9999.8	2.754	F	11.92	3.92	1.04	59.8
112	4.122	4.209	0.5	10000.1	2.718	F	11.82	3.92	1.04	59.8
113	4.101	4.208	0.5	10000.5	2.707	F	11.79	3.92	1.04	59.8
114	4.173	4.119	1.3	9999.6	2.773	F	12	3.92	1.03	59.8
115	4.097	4.119	0.8	10000.1	2.722	F	11.85	3.92	1.03	59.8
116	4.219	4.208	0.7	10000.4	2.751	F	11.88	3.92	1.04	59.8
117	4.171	4.118	1	9999.7	2.763	F	11.96	3.91	1.03	59.9
118	4.101	4.208	0.6	9999.1	2.701	F	11.77	3.92	1.04	59.9
119	4.112	4.208	0.6	9999.5	2.707	F	11.78	3.92	1.04	60
120	4.171	4.119	1.1	9999.8	2.763	F	11.96	3.91	1.03	60
121	4.17	4.118	1.4	9998.9	2.772	F	11.99	3.92	1.03	60
122	4.171	4.118	1.1	10000	2.763	F	11.96	3.91	1.03	60
123	4.21	4.21	0.6	10000.4	2.739	F	11.84	3.92	1.04	60.1
124	4.171	4.118	1.3	10000.1	2.772	F	11.99	3.92	1.03	60
125	4.145	4.207	0.6	9999.5	2.732	F	11.86	3.92	1.04	60.1
126	4.169	4.118	1.3	9999.7	2.771	F	11.99	3.92	1.03	60.1
127	4.096	4.2	0.5	9999.3	2.703	F	11.78	3.91	1.04	60.1
128	4.171	4.118	1.1	9999.6	2.764	F	11.96	3.91	1.03	60.1
129	4.172	4.119	1.2	10000	2.764	F	11.96	3.91	1.03	60.1
130	4.213	4.209	0.6	10000.1	2.74	F	11.85	3.92	1.04	60.2
131	4.174	4.119	1.4	10000.4	2.774	F	12	3.92	1.03	60.2
132	4.101	4.118	0.5	9999.5	2.701	F	11.77	3.91	1.03	60.1
133	4.17	4.118	1.1	9999.5	2.763	F	11.96	3.91	1.03	60.2
134	4.171	4.118	1.1	9999.6	2.764	F	11.96	3.91	1.03	60.2
135	4.17	4.119	1.1	9999.5	2.763	F	11.96	3.91	1.03	60.2
136	4.17	4.119	1.2	10000	2.762	F	11.96	3.91	1.03	60.2
137	4.175	4.119	1.4	10000.3	2.775	F	12	3.92	1.03	60.2
138	4.17	4.119	1	9999.7	2.763	F	11.96	3.91	1.03	60.2
139	4.174	4.119	1.4	10000.4	2.774	F	12	3.92	1.03	60.2
140	4.171	4.118	1.3	9999.6	2.773	F	12	3.92	1.03	60.3
141	4.168	4.119	1.1	9999.6	2.762	F	11.96	3.91	1.03	60.3
142	4.169	4.118	1.1	9999.6	2.763	F	11.96	3.91	1.03	60.3
143	4.176	4.119	1.2	10000	2.767	F	11.97	3.91	1.03	60.3
144	4.092	4.118	0.5	9999.4	2.712	F	11.81	3.91	1.03	60.2
145	4.179	4.118	1.5	9999.7	2.778	F	12.01	3.92	1.03	60.2
146	4.161	4.118	1	9999.7	2.758	F	11.94	3.91	1.03	60.3
147	4.092	4.118	0.6	9999.5	2.72	F	11.84	3.92	1.03	60.2

148	4.162	4.117	1.3	9999.3	2.767	F	11.98	3.92	1.03	60.3
149	4.168	4.117	1	9999.1	2.762	F	11.96	3.91	1.03	60.2
150	4.108	4.208	0.4	10000	2.707	F	11.78	3.92	1.04	60.3
151	4.17	4.118	1.2	9999.7	2.763	F	11.96	3.91	1.03	60.3
152	4.116	4.209	0.4	10000.4	2.711	F	11.8	3.92	1.04	60.2
153	4.117	4.208	0.5	9999.7	2.711	F	11.8	3.91	1.04	60.3
154	4.107	4.208	0.5	9999.7	2.705	F	11.78	3.91	1.04	60.3
155	4.107	4.209	0.4	10000.3	2.704	F	11.77	3.91	1.04	60.3
156	4.107	4.207	0.4	9999.4	2.704	F	11.77	3.91	1.04	60.3
157	4.137	4.209	0.5	10000.7	2.719	F	11.81	3.91	1.04	60.3
158	4.129	4.208	0.5	10000.1	2.713	F	11.79	3.91	1.04	60.3
159	4.112	4.208	0.4	9999.5	2.709	F	11.79	3.91	1.04	60.3
160	4.129	4.209	1	9999.5	2.712	F	11.79	3.91	1.04	60.3
161	2.383	2.313	0.5	1299.3	2.686	F	9.35	1.8	1.69	60.4
162	2.962	2.67	0.5	1600.4	2.702	F	9.39	1.82	1.68	60.3

3. IFT of Oil-SDS

Run-No	IFT_LY	IFT_CSW	Et	Speed	Vol LY	Type
1	2.709	2.595	44	2799.7	5.874	F
2	2.709	2.595	44	2799.6	5.874	F
3	2.710	2.595	44	2800.3	5.874	F
4	2.709	2.595	44	2799.7	5.874	F
5	2.709	2.595	44	2799.4	5.874	F
6	2.711	2.597	44	2800.4	5.874	F
7	2.709	2.595	44	2799.5	5.874	F
8	2.710	2.595	44	2799.8	5.874	F
9	2.710	2.596	44	2800.0	5.874	F
10	2.710	2.596	44	2800.2	5.874	F
11	2.709	2.595	44	2799.7	5.874	F
12	2.711	2.597	44	2800.4	5.874	F
13	2.709	2.595	44	2799.7	5.874	F
14	2.708	2.594	44	2798.9	5.874	F
15	2.709	2.595	44	2799.7	5.874	F
16	2.711	2.596	44	2800.3	5.874	F
17	2.710	2.596	44	2800.0	5.874	F
18	2.709	2.595	44	2799.7	5.874	F
19	2.710	2.596	44	2800.1	5.874	F
20	2.709	2.595	44	2799.5	5.874	F
21	2.709	2.595	44	2799.6	5.874	F
22	2.708	2.594	44	2799.3	5.874	F
23	2.711	2.597	44	2800.4	5.874	F
24	2.709	2.595	44	2799.5	5.874	F
25	2.710	2.596	44	2800.1	5.874	F
26	2.711	2.596	44	2800.4	5.874	F
27	2.709	2.595	44	2799.5	5.874	F
28	2.708	2.594	44	2799.3	5.874	F
29	2.710	2.596	44	2800.3	5.874	F
30	2.711	2.596	44	2800.3	5.874	F
31	2.711	2.596	44	2800.3	5.874	F
32	2.710	2.596	44	2800.3	5.874	F
33	2.709	2.595	44	2799.5	5.874	F
34	2.709	2.595	44	2799.5	5.874	F
35	2.710	2.596	44	2800.0	5.874	F
36	2.710	2.596	44	2800.0	5.874	F
37	2.710	2.596	44	2800.1	5.874	F
38	2.710	2.596	44	2800.3	5.874	F
39	2.709	2.595	44	2799.4	5.874	F
40	2.709	2.595	44	2799.7	5.874	F
41	2.711	2.596	44	2800.4	5.874	F
42	2.709	2.595	44	2799.6	5.874	F
43	2.710	2.596	44	2800.0	5.874	F

Abbreviations and units used in the list: IFT_LY = Interface tension (Laplace - Young); IFT_CSW = Interface tension (Cassie-Schaeffer Wert); F = full shape; L = left side; R = right side; C = cylindrical part; cDens = density difference [g/cm^3]; Vol = volume [μl]; Err = fitting error [g/cm^2]; Speed = rotation speed [1/min]; Alpha = drop shape parameter alpha; a = drop curvature at apex [mm]

Run-No	IFT_LY	IFT_CSW	Err	Speed	Vol LY	Type
44	2.709	2.595	4.4	2799.6	5.874	F
45	2.709	2.595	4.4	2799.4	5.874	F
46	2.710	2.596	4.4	2800.1	5.874	F
47	2.710	2.595	4.4	2799.8	5.874	F
48	2.710	2.596	4.4	2800.1	5.874	F
49	2.709	2.595	4.4	2799.5	5.874	F
50	2.709	2.595	4.4	2799.5	5.874	F
51	2.709	2.595	4.4	2799.4	5.874	F
52	0.000	0.000	4.4	0.0	0.000	F
53	0.000	0.000	4.4	0.0	0.000	F
54	0.000	0.000	4.4	0.0	0.000	F
55	0.000	0.000	4.4	0.0	0.000	F
56	0.000	0.000	4.4	0.0	0.000	F
57	0.000	0.000	4.4	0.0	0.000	F
58	0.000	0.000	4.4	0.0	0.000	F
59	0.000	0.000	4.4	0.0	0.000	F
60	0.000	0.000	4.4	0.0	0.000	F
61	0.000	0.000	4.4	0.0	0.000	F
62	0.000	0.000	4.4	0.0	0.000	F
63	0.000	0.000	4.4	0.0	0.000	F
64	0.000	0.000	4.4	0.0	0.000	F
65	0.000	0.000	4.4	0.0	0.000	F
66	0.000	0.000	4.4	0.0	0.000	F
67	0.000	0.000	4.4	0.0	0.000	F
68	0.000	0.000	4.4	0.0	0.000	F
69	0.000	0.000	4.4	0.0	0.000	F
70	0.000	0.000	4.4	0.0	0.000	F
71	0.000	0.000	4.4	0.0	0.000	F
72	0.000	0.000	4.4	0.0	0.000	F
73	0.000	0.000	4.4	0.0	0.000	F
74	0.000	0.000	4.4	0.0	0.000	F
75	0.000	0.000	4.4	0.0	0.000	F
76	0.000	0.000	4.4	0.0	0.000	F
77	0.000	0.000	4.4	0.0	0.000	F
78	0.000	0.000	4.4	0.0	0.000	F
79	0.000	0.000	4.4	0.0	0.000	F
80	0.000	0.000	4.4	0.0	0.000	F
81	0.000	0.000	4.4	0.0	0.000	F

Abbreviations and units used in the list: IFT_LY = Interface tension (Laplace - Young); IFT_CSW = Interface tension (Caylor Schechter魏德); F = full shape; L = left side; R = right side; C = cylindrical part; cDens = density difference [g/cm^3]; Vol = volume [μl]; Err = fitting error [pixels]; Speed = rotation speed [1/min]; Alpha = drop shape parameter alpha; a = drop curvature at apex [mm]

APPENDIX C

CRUDE OIL INFORMATION

Reference: ARAH20020601

Crude: Arabian Heavy

Crude Summary Report

General Information		Molecules (%wt on crude)										Whole Crude Properties				
Reference:	ARAH20020601	methane	+ ethane	0.04	Density @ 15°C (g/cc)	0.886										
Traded Crude:	Arab Heavy	propane		0.38	API Gravity	28.10										
Origin:	Saudi Arabia	isobutane		0.19	Total Sulphur (% wt)	2.92										
Sample Date:	Mar-93	n-butane		0.90	Pour Point (°C)	-45.00										
Assay Date:	Jun-02	isopentane		0.61	Viscosity @ 20°C (cSt)	49.00										
Issue Date:	Jun-02	n-pentane		1.10	Viscosity @ 40°C (cSt)	20.60										
		cyclopentane		0.07	Nickel (ppm)	22.3										
		C ₆ paraffins		2.18	Vanadium (ppm)	70.4										
		C ₆ naphthalenes		0.34	Total Nitrogen (ppm)	1750										
		benzene		0.04	Total Acid Number (mgKOH/g)	0.26										
		C ₇ paraffins		1.99	Mercaptan Sulphur (ppm)	2.7										
		C ₇ naphthalenes		0.53	Hydrogen Sulphide (ppm)	-										
		toluene		0.18	Reid Vapour Pressure (psi)	6.7										
Cut Data		Atmospheric Cuts										Vacuum Cuts				
Start (°C)	IBP	C5	65	100	150	200	250	300	350	370	370	370	450	500	550	550
End (°C)	FBP	65	100	150	200	250	300	350	370	FBP	450	500	550	550	550	550
Yield (% wt)		2.8	3.8	5.4	5.8	6.8	7.5	7.8	3.1	55.5	11.8	6.6	6.0	31.0		
Yield (% vol)		3.8	4.8	6.4	6.6	7.4	7.9	7.9	3.1	49.6	11.5	6.3	5.6	26.2		
Cumulative Yield (% wt)		1.5	4.3	8.1	13.5	19.2	26.0	33.6	41.3	44.5	44.5	56.3	62.9	69.0		
Volume Average B.P. (°C)	398	43	85	128	176	225	275	325	360	600	409	475	525	730		
Density @ 15°C (g/cc)	0.886	0.643	0.692	0.745	0.776	0.809	0.839	0.867	0.891	0.991	0.910	0.936	0.956	1.047		
API Gravity	28.1	88.5	73.1	58.5	50.7	43.4	37.1	31.7	27.2	11.2	24.0	19.6	16.4	3.6		
UOPK	12.0				12.1	12.0	11.9	11.9	11.8	11.7	11.8	11.8	11.8	11.6		
Molecular Weight (g/mol)				115	148	183	222	266	300	518	351	426	485	682		
Total Sulphur (% wt)	2.92	0.000	0.003	0.019	0.107	0.405	1.18	2.04	2.49	4.56	2.85	3.33	3.75	5.63		
Mercaptan Sulphur (ppm)	2.7	3.8	6.2	14.1	25.0	2.2	0.1									
Total Nitrogen (ppm)	1750					11	19	61	221	3120	524	885	1240	4960		
Basic Nitrogen (ppm)	424					0.433	4.12	22.5	50.3	757	114	231	341	1200		
Total Acid Number (mgKOH/g)	0.26	0.00	0.01	0.02	0.05	0.08	0.13	0.20	0.24	0.23	0.27	0.29	0.30	0.19		
Viscosity @ 20°C (cSt)	49.0					1.22										
Viscosity @ 40°C (cSt)	20.6					0.93	1.71	2.84	5.73	10.5						
Viscosity @ 50°C (cSt)	14.7						1.48	2.38	4.57	7.88	4700	18.2	74.6	195		
Viscosity @ 60°C (cSt)											1900	13.2	46.4	110		
Viscosity @ 100°C (cSt)											142	4.79	11.4	20.6	12400	
Viscosity @ 130°C (cSt)																1210
RON (Clear)		76.5	42.6	41.6	36.5											
MON (Clear)		76.1	42.8	41.8	34.7											
Paraffins (% wt)		97.6	84.3	67.0	65.1											
Naphthalenes (%wt)		2.4	14.7	18.3	15.9											
Aromatics (% wt)		0.0	1.0	14.7	19.0											
Pour Point (°C)	-45					-41	-18	-1	9	21	21	31	32	76		
Cloud Point (°C)						-37	-16	0								
Freeze Point (°C)						-66	-37	-13								
Smoke Point (mm)						27	23	18								
Cetane Index						46	51	55	57	57						
Naphthalenes (% vol)						0.36	2.69	6.78	10.87		80.2	84.5	87.1			
Aniline Point (°C)						51.8	56.2	63.0	68.8	73.4	76.4					
Hydrogen (% wt)		16.6	15.9	14.6	14.3	13.8	13.4	12.9	12.6		12.3	12.1	12.0			
Wax (% wt)	3.8									5.7	8.4	9.2	8.7	3.4		
C ₉ Asphaltenes (% wt)	4.8									8.6	0.0	0.0	15.4			
Micro Carbon Residue (% wt)	8.4									15.1	0.4	1.8	26.6			
Rams. Carbon Residue (% wt)	5.9									10.7	0.3	1.6	18.8			
Vanadium (ppm)	70.4									127.0	0.0	0.0	227.0			
Nickel (ppm)	22.3									40.2	0.0	0.0	71.8			
Iron (ppm)	3.9									7.0	0.0	0.0	12.5			

APPENDIX D

OIL RECOVERY EVALUATION & CALCULATION

Displacement Tests

Procedures:

- 1) The experimental setup is fixed as shown in Figure 3.11, with three types of injection fluid prepared in-line; brine, crude oil and nanofluids.
- 2) Brine of concentration 30,000 ppm is used to saturate the porous medium with flow rate of 2.5 ml/min, until the pressure difference, Δp across the porous medium reaching steady state.
- 3) Brine injection is terminated and the next injection resumes with crude oil at the same flow rate.
- 4) During the oil injection process, brine will be displaced out through a tube and continue until oil drop can be seen on top of the brine. This condition shows that the core sample has been fully saturated with oil with just a little amount of connate water (residual brine). The volume of brine displaced from the core sample will be equal to the volume of the crude oil going into the core sample. This volume represents the amount of original oil in place (OOIP).
- 5) The process continues with the secondary brine injection, to imitate the water flooding stage. Brine will displace a substantial amount of crude oil until depletion occurs and brine started to emerge from the outlet. Water flooding process will be terminated when oil depletion occur (water cut reach more than 20%). The volume of oil being displaced from the porous medium represents the volume of oil recovered from the secondary recovery, i.e. water flooding.
- 6) Subsequently, EOR processes will take place by injecting nanofluid and other possible EOR agents at the same flow rate and displaced oil collected at the outlet will be evaluated for recovery efficiency.
- 7) Step 1 until 6 are repeated for evaluation of another samples.

Recovery Calculation (Case = Surfactant (SDS) injection)

1. Determining the porosity of the packed glass beads

Dry weight of the porous medium (before brine saturation) = 1248.40 g

Wet weight of the porous medium (after brine saturation) = 1318.80 g

$$\Delta \text{Weight} = 1318.80 - 1248.40 = 70.40 \text{ g}$$

Length of porous medium = 14.7 cm

Cross-sectional area = 15.91 cm²

Saturating fluid density (brine) = 1.02 g/cm³

$$\begin{aligned}\text{Porosity of the medium} &= \frac{\text{Pore volume}}{\text{Bulk volume}} \times 100 \\ &= \frac{\Delta \text{Weight} / \text{Density of saturating fluid}}{\text{cross sectional area} \times \text{length}} \times 100 \\ &= \underline{\underline{29.51\%}}\end{aligned}$$

2. Determining permeability of porous medium

By applying Darcy's law;

$$q = \frac{kA(p_1 - p_2)}{\mu L}$$

$$k = \frac{q\mu L}{A\Delta p}$$

$$= 62.02 \text{ mD}$$

* $q = 2.5 \text{ ml/min}$; $\mu = 1.009 \text{ g/cm}$; $L = 14.7 \text{ cm}$; $A = 15.91 \text{ cm}^2$; Δp = (pressure gauge reading at steady state condition during brine saturation)

3. Determining Original Oil in Place (OOIP)

Volume of brine displaced out (during oil injection) = Volume of crude oil in the porous medium (OOIP)

4. Recovery calculation for water flooding process

$$\begin{aligned}
 \text{Recovery Factor (RF)} &= \frac{V_{oil}}{OOIP} \times 100 \\
 &= \frac{48.25ml}{65.00ml} \times 100 \\
 &= 74.23 \% \text{OOIP}
 \end{aligned}$$

$$\begin{aligned}
 \text{Residual oil in Place (ROIP)} &= \text{OOIP} - \text{Vol. oil recover during water flooding} \\
 &= 65.00 - 48.25 \\
 &= 16.75 \text{ ml}
 \end{aligned}$$

5. Recovery calculation for EOR process

$$\begin{aligned}
 E_R (\% \text{ROIP}) &= \left(\frac{\text{Volume of oil recovered in EOR fluid injection}}{\text{ROIP}} \right) \times 100 \\
 &= \frac{3.97ml}{16.75ml} \times 100 \\
 &= \underline{23.70 \% \text{ROIP}}
 \end{aligned}$$